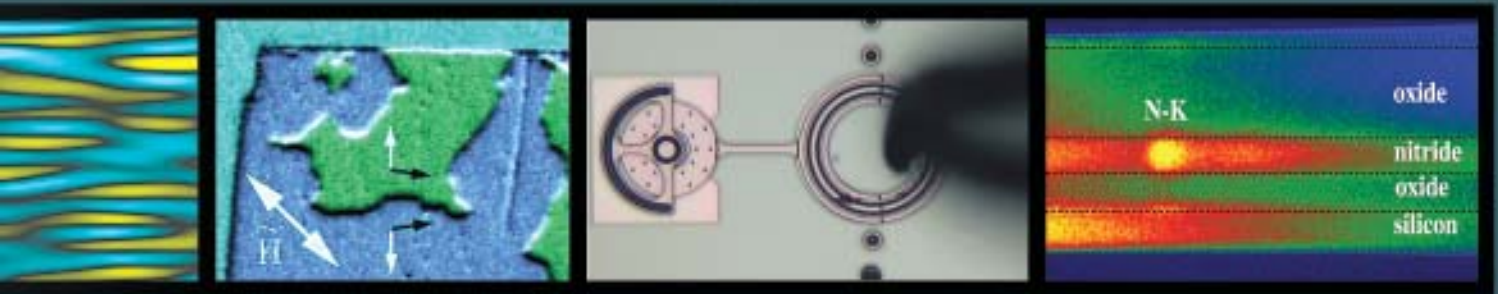


MICRO- & OPTOELECTRONICS



MATERIALS SCIENCE AND
ENGINEERING LABORATORY

ANNUAL REPORT

NIST

National Institute of
Standards and Technology

Technology Administration

U.S. Department of
Commerce

NISTIR 6971

March 2003

On the Cover:

From the front cover and continuing on to the back, the images shown are, respectively: (1) Two-dimensional (2D) electron energy loss spectra (EELS) from a silicon oxide-nitride-oxide (ONO) stack, in which the horizontal dimension corresponds to energy loss, and the vertical represents a spatial coordinate; that is, each 2D spectrum represents a collection of EELS spectra spatially-resolved across the interfaces. From “Nanoscale Structural/Compositional Characterization of Ultra-Thin Films; (2) Tensile test specimen — MEMS polysilicon thickness 4 micrometers; (3) Magneto-optical image of domain patterns in a new “synthetic antiferromagnet” Co/Ru/Co trilayer showing two different types of domains separated by novel non-180 degree walls. Similar trilayers are used in high density recording media; (4) Color representation of one normal mode of magnetization vibration calculated for a 50 nm thick film of Permalloy with 20 nm defects; and (5) A synchrotron x-ray scattering pattern of a nanostructured thin film for electronic applications.

NIST Website: www.nist.gov
Voice Phone: 301-975-2000

**National Institute of
Standards and Technology**
Arden L. Bement, Jr.
Director

**Technology
Administration**
Phillip J. Bond
Undersecretary of
Commerce for Technology

**U.S. Department
of Commerce**
Donald L. Evans
Secretary



MATERIALS SCIENCE AND ENGINEERING LABORATORY

FY 2002 PROGRAMS AND ACCOMPLISHMENTS

MSEL MATERIALS FOR MICRO- AND OPTOELECTRONICS

Frank W. Gayle
Deputy Chief, Metallurgy Division

NISTIR 6971

March 2003

Certain commercial entities, equipment, or materials may be identified in this document in order to describe an experimental procedure or concept adequately. Such identification is not intended to imply recommendation or endorsement by the National Institute of Standards and Technology, nor is it intended to imply that the entities, materials, or equipment are necessarily the best available for the purpose.

Table of Contents

Executive Summary	1
Technical Highlights	3
Pore Size Distributions in Low-k Dielectric Thin Films from X-ray Porosimetry	4
Direct Measurement of the Reaction Front in Chemically Amplified Photoresists	6
Nanoscale Structural/Compositional Characterization of Ultra-Thin Films	8
Advanced Metallizations for Sub-100 Nanometer Electronics	10
Carbon Nanotubes: Characterization and Application for Nanometer Scale Devices	12
Performance-Limiting Defects in GaN	14
Strain in Compound Semiconductor Photonic Systems	16
Magnetization Dynamics in Films with Nanometer Scale Microstructure	18
Ballistic Magnetoresistance: A New Phenomenon with Great Potential for Magnetic Sensors	20
High-Speed Contact at the Head-Disk Interface in a Magnetic Hard Disk Drive: Experiment and Modeling	22
Projects in Materials for Micro- and Optoelectronics	25
<i>Microelectronics</i>	
Characterization of Porous Low-k Dielectric Constant Thin Films	26
Dielectric Metrology for Polymer Composite Films in the Microwave Range	27
Polymer Photoresists for Next-Generation Lithography	28
Superconformal Film Growth: Measurements and Modeling	29
Micrometer-Scale Reliability: Stress Voiding and Electromigration	30
Phase Equilibria and Properties of Dielectric Ceramics	31
Processing of Low Temperature of Co-Fired Ceramics	32
Solder and Solderability Measurements for Microelectronics	33
Mechanism of Sn Whisker Growth from Electrodeposits	34
Solder Reliability: Lead-Free Solder	35
Micrometer-Scale Reliability: Mechanical Behavior of Thin Films	36
Electronic Packaging and Components: Packaging Reliability	37
Electronic Packaging and Components: Acoustic Loss in Piezo Crystals	38

Optoelectronics

Combinatorial Materials Research: Interconnects to Optoelectronic Materials	39
Optical and Structural Characterization of Optoelectronic Semiconductors	40
Micrometer-Scale Reliability: Strain in Photonic Semiconductors	41

Magnetic Materials

Magnetic Properties and Standard Reference Materials	42
Magnetic Properties of Nanostructured Materials	43
Nanomagnetodynamics	44
New Materials for Ultra-High Density Data Storage	45
Nanotribology	46
Metrology for Nanoscale Properties: Brillouin Light Scattering	47

Related Projects

Nanoscale Characterization: Electron Microscopy	48
Phase Diagrams in High Temperature Superconductors	49

Organizational Charts	51
-----------------------------	----

Executive Summary

Introduction

U.S. microelectronics and related industries are in fierce international competition to design and produce smaller, lighter, faster, more functional, and more reliable electronic products more quickly and economically than ever before. At the same time, there has been a revolution in recent years in new materials used in all aspects of microelectronics fabrication.

Since 1994, the NIST Materials Science and Engineering Laboratory (MSEL) has worked closely with the U.S. semiconductor, component, packaging, and assembly industries. These efforts led to the development of an interdivisional MSEL program committed to addressing industry's most pressing materials measurement and standards issues central to the development and utilization of advanced materials and material processes. The vision that accompanies this program — to be the key resource within the Federal Government for materials metrology development for commercial microelectronics manufacturing — may be realized through the following objectives:

- Develop and deliver standard measurements and data;
- Develop and apply *in situ* measurements on materials and material assemblies having micrometer- and submicrometer-scale dimensions;
- Quantify and document the divergence of material properties from their bulk values as dimensions are reduced and interfaces contribute strongly to properties;
- Develop models of small, complex structures to substitute for or provide guidance for experimental measurement techniques; and
- Develop fundamental understanding of materials needed in future micro- and opto-electronics.

With these objectives in mind, the program presently consists of projects led by the Metallurgy, Polymers, Materials Reliability, and Ceramics Divisions that examine and inform industry on key materials-related issues. These projects are conducted in concert with partners from industrial consortia, individual companies, academia, and other government agencies. The program is strongly coupled with other microelectronics programs within government and industry, including the National Semiconductor Metrology Program (NSMP) at NIST.

The present report describes the major technical activities and accomplishments in the area of Materials for Micro- and Optoelectronics within MSEL in FY2002 (October 2001 through September 2002). In this report, we have tried to provide insight into

how MSEL research programs meet the needs of our customers, how MSEL capabilities are being used to solve problems important to the national economy and the materials metrology infrastructure, and how MSEL interacts with its customers to establish new priorities and programs. Feedback and suggestions on how we can better serve the needs of our customers and encourage increasing collaboration to this end are welcomed.

Mission

Our mission is to provide critical leadership in the development of measurement methods and standards, as well as fundamental understanding of materials behavior needed by the U.S. microelectronics and optoelectronics industries to remain competitive in the changing global marketplace. As an essential part of this mission, we are responsible not only for developing new measurement methods with broad applicability across micro- and optoelectronics classes and industries, but also for working with individual industry groups to develop and integrate measurements, standards, software tools, and evaluated data for specific, technologically important applications.

Establishing Priorities

As part of the development of this technical program, a wide range of research opportunities are examined. Choices for the research portfolio are based on several criteria: the match to the NIST mission, the magnitude and immediacy of industrial need, the degree to which NIST's contribution is critical for success, the anticipated impact relative to the investment, ability to respond in a timely fashion with high-quality output, and the opportunity to advance mission science. This requires that MSEL establish its research priorities through extensive consultation and collaboration with customers in U.S. industry and with counterparts in the international metrology community using a variety of methods including workshops, technical meetings, standards committee participation, and individual consultation with our customers. Materials metrology needs are also identified through industry groups and roadmaps, including the International Technology Roadmap for Semiconductors (ITRS), the IPC Lead-free Solder Roadmap, the National Electronics Manufacturing Initiative (NEMI) Roadmap, the Optoelectronics Industry Development Association (OIDA) roadmaps, and the National [Magnetic Data] Storage Industry Consortium (NSIC).

This program deals almost exclusively with rapidly evolving technologies, where advances in measurement science are needed to understand the limitations on

Executive Summary

system behavior. MSEL focuses its efforts to address these needs in order to have the best chance to have an impact on the course of technology.

Research Portfolio

Although there is increasing integration within various branches of microelectronics and optoelectronics, the field can be considered to consist of three main areas. The first, microelectronics, includes needs ranging from integrated circuit fabrication to component packaging to final assembly. MSEL programs address materials metrology needs in each of these areas including, for example, lithographic polymers and electrodeposition of interconnects, electrical, mechanical, and physical property measurement of dielectrics (interlevel, packaging, and wireless applications), and packaging and assembly processes (lead-free solders, solder interconnect design, thermal stress analysis, and co-fired ceramics).

The second major area is optoelectronics, which includes work that often crosses over into electronic and wireless applications. Projects currently address residual stress measurement in optoelectronic films, performance of III-V optical materials, and wide bandgap semiconductors. In particular, the wide bandgap program has grown as a new collaboration with the NIST Electronic and Electrical Engineering Laboratory (EEEL). Building on the existing projects on metal interconnects for GaN (Metallurgy Division) and on interface and bulk defects in GaN (Ceramics Division), the EEEL/MSEL program is developing a comprehensive suite of measurement methods for characterizing interface and bulk defects limiting the application of GaN and related materials.

The third area is magnetic data storage where the market potential is vast and growing and the technical challenges extreme. NSIC plans to demonstrate a recording density of 1 terabit per square inch — 40 times today's level — by 2006. To reach these goals, new materials are needed that have smaller grain structures, can be produced as thin films, and can be deposited uniformly and economically. New lubricants

are needed to prevent wear as spacing between the disk and head becomes smaller than the mean free path of air molecules. Some measurements require calibration of magnetometers using certified magnetic standards in several different shapes and magnetic strengths, and with a wide range in magnetic character. These standards are now being produced under this program. MSEL is working with the magnetic recording industry to develop measurement tools, modeling software, and standards to help achieve these goals. Staff expertise at MSEL spans all fields relevant to magnetic data storage, including materials science, electrical engineering, physics, mathematics and modeling, manufacturing engineering, chemistry, metrology, and computer science, with the Materials Science and Engineering Laboratory, the Electronics and Electrical Engineering Laboratory, the Physics Laboratory, the Information Technology Laboratory, and the Manufacturing Engineering Laboratory working as partners in this effort.

In 2001, two new major projects were initiated within Magnetic Data Storage. As part of the National Nanotechnology Initiative, a major collaboration among MSEL, the Information Technology Laboratory (ITL), and the Electronics and Electrical Engineering Laboratory (EEEL) is developing new measurement methods and models for magnetic damping, needed by the magnetic recording industry to improve switching speed. In 2002, a long-term project on GMR thin films was refocused into Spintronics, the use of spin-polarized electrons for new devices and magnetic imaging. Through an extensive network of university and industrial collaborators, the process measurement and control capabilities of the MSEL Magnetic Engineering Research Facility are being used to develop an understanding of the materials structure and processing issues in the creation and transfer of spin-polarized electrons.

MSEL output exists in a variety of forms, from a fundamental understanding of micro- and optoelectronics behavior to measurement techniques conveyed through scientific literature and oral presentations, standard reference materials, evaluated data and online databases, software tools, and sensors for on-line process control.

Technical Highlights

The following Technical Highlights section includes expanded descriptions of research projects that have broad applicability and impact. These projects generally continue for several years. The results are the product of the efforts of several individuals. The Technical Highlights include:

- Pore Size Distributions in Low-k Dielectric Thin Films from X-ray Porosimetry
- Direct Measurement of the Reaction Front in Chemically Amplified Photoresists
- Nanoscale Structural/Compositional Characterization of Ultra-Thin Films
- Advanced Metallizations for Sub-100 Nanometer Electronics
- Carbon Nanotubes: Characterization and Application for Nanometer Scale Devices
- Performance-Limiting Defects in GaN
- Strain in Compound Semiconductor Photonic Systems
- Magnetization Dynamics in Films with Nanometer Scale Microstructure
- Ballistic Magnetoresistance: A New Phenomenon with Great Potential for Magnetic Sensors
- High-Speed Contact at the Head-Disk Interface in a Magnetic Hard Disk Drive: Experiment and Modeling

Pore Size Distributions in Low-k Dielectric Thin Films from X-ray Porosimetry

NIST is working to provide the semiconductor industry with detailed information on the nanoscopic pore size distribution of porous thin films destined as low-k dielectric materials for the next generation of integrated circuits. The electronics industry has chosen the introduction of nanometer scale pores into interlayer dielectric films as the method of lowering the effective dielectric constant. While these modifications change the dielectric constant favorably, other important parameters such as physical strength and barrier properties will also change, often in an unfavorable way. A new method has been developed to calculate the pore size distribution from x-ray reflectivity measurements on thin films in a controlled environment of solvent vapor.

The rapid and sustained advances in ultra-large-scale integrated circuit performance have been driven, to a large extent, by miniaturization of the circuitry. At these nanoscopic sizes, interlayers with extremely low dielectric constants (low-k) are imperative to reduce cross-talk and to increase processor speed. While the candidate materials differ in their base chemistries, a common theme emerges in the push to develop low-k dielectric materials: nano-scale porosity must be introduced in a controlled manner to further reduce the dielectric constant. Techniques are needed to accurately and non-invasively characterize the porosity in these films while attached on a silicon substrate.

Capillary porosimetry is a prime candidate to measure the pore size distribution (PSD) of the nanoporous films. Bulk materials have been characterized in this manner by measurement of the mass gain of the material when exposed to a controlled pressure of solvent vapor. As the pressure of the probe solvent increases, pores become filled hierarchically by size as is described by the appropriate thermodynamic analysis such as the Kelvin equation:

$$r = \frac{-2V_m\gamma}{RT \ln(P/P_0)}$$

where the pore radius, r , can be calculated from the partial solvent vapor pressure, P/P_0 , known thermodynamic properties of the solvent such as surface tension, γ , and molar volume, V_m , temperature, T , and gas constant, R .

X-ray reflectivity (XR) has been extensively used in the Polymers Division to measure the thickness and density of 1 μm nanoporous thin films. A method of x-ray porosimetry (XRP) has been developed to create a controlled solvent environment around the thin film so

that an equilibrium amount of adsorption occurs. The value of P/P_0 can be varied either by mixing volumes of solvent saturated and dry air at a constant temperature, or by blanketing the sample in air that has reached solvent saturation at a low temperature and increasing the temperature of the thin film. Under such conditions, a standard XR scan gives accurate values of the total density that is a combination of wall density and solvent filled pores. The mass uptake as a function of partial pressure is calculated from these results.

As an example, the reflectivity data from the porous hydrogen silsesquioxane (HSQ) and the silica xerogel films are shown in Figure 1. Each of the two samples has several data sets plotted together to show the effect of solvent adsorption. A critical edge is clearly visible at low q_z values as the sharp drop in $\log(\text{Reflectivity})$ from the initially flat reflectivity curve. In Figure 1, four curves are shown for each sample, varying from the sample exposed to dry air (left most curve) to sample in saturated toluene vapor (right most curve). There is a progression of the critical edge to higher q_z as the vapor pressure increases, due to the increased electron density of the film as the smaller pores become saturated with liquid toluene.

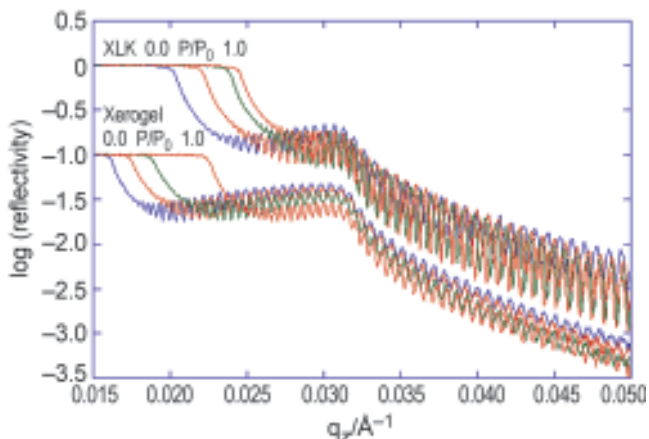


Figure 1: XR curves of a porous organosilsesquioxane (XLK™) and xerogel films under controlled partial toluene vapor pressure.

At $P/P_0 = 1$, toluene will condense in all of the accessible pores or open pores by definition, so the uptake at saturation, W_0 , is a measure of the porosity. It should be emphasized that this porosity only reflects those pores that the toluene can infiltrate. There may also be closed pores not accessible to toluene vapor and therefore not reflected in the XR porosity. Therefore, a matrix density that is a combination of dense wall material and inaccessible closed pores can be calculated.

Figure 2 presents the adsorption/desorption data for a porous methyl silsesquioxane (MSQ) spin-on glass (SOG) film in which P/P_0 is varied through the substrate temperature. The solid lines are cubic spline fits through the data and accurately mimic the shape of the curves. The data points have considerably less scatter than the data in which the isothermal technique is employed. The hysteresis loop is very well defined with data outside of the loop coinciding accurately. If the principle of temperature–pressure equivalency is valid, the temperature control method clearly increases the accuracy of the measurement.

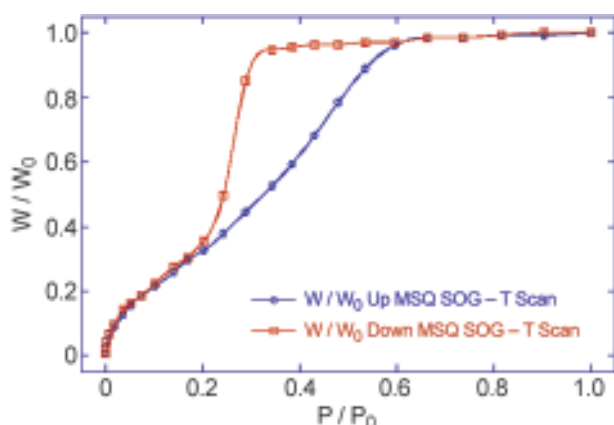


Figure 2: XR toluene vapor adsorption data from MSQ SOG films by varying the substrate temperature.

The pore size distribution can be calculated by use of the Kelvin equation and other thermodynamic considerations from a point-by-point differentiation, as shown in Figure 3.

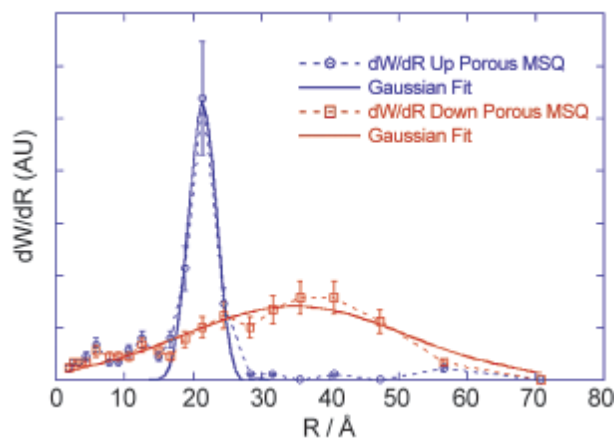


Figure 3: PSD of MSQ SOG films by varying the substrate temperature (where AU = arbitrary units).

There are several advantages of XRP over other techniques to determine pore size in ultrathin films. Some methods require that the film be deposited on

a special substrate, such as the piezoelectric surfaces required for both the quartz crystal microbalance and surface acoustic waves techniques. XRP can be done on any smooth substrate, including the Si wafers used in the semiconductor industry. In many ways, XRP is similar and complimentary to optical methods such as ellipsometric porosimetry (EP). However, the EP analysis requires knowledge of the optical constants, for both the matrix and the adsorbate. With EP it is also necessary to invoke the additional assumption that the polarizabilities are additive. XRP does not require these additional assumptions.

Another potential advantage of XRP is the ability to quantify not only the average film density, but also the density profile normal to the film surface. X-ray reflectivity has been used to extract non-uniform density profiles in a series of low- k films. It may be possible to use XRP to extract pore size distributions as a function of depth into film. To prevent dielectric breakdown, it is desirable to have low porosity or very small pores near the surfaces with the majority of the porosity localized in the center of the thin film. XRP could prove to be very useful for characterizing these types of structures.

“The SANS/SXR measurements have become a key metric in our low- k dielectric materials characterization and screening process.”

Dr. Jeffrey Wetzel

Manager
Low- k Materials Technology
International SEMATECH

“The NIST x-ray reflectivity program is useful, perhaps even critical, to the industry.”

Dr. Abner Bello

Technical Staff Member
Defect and Thin Film Characterization
Laboratory Applied Materials, Inc.

For More Information on this Topic

B.J. Bauer, W.L. Wu (Polymers Division, NIST)

Hae-Jeong Lee, Christopher L. Soles, Da-wei Liu, Barry J. Bauer and Wen-li Wu, “Pore size distributions in low- k dielectric thin films from X-ray porosimetry,” *Journal of Polymer Science, Polymer Physics Edition*, (in press).

Direct Measurement of the Reaction Front in Chemically Amplified Photoresists

The continual device performance increases by the semiconductor industry has been largely driven by the fabrication of smaller structures with lithography. As feature sizes approach sub-100 nm, the photolithographic process must be controlled with tolerances of (2 to 5) nm, dimensions comparable to the molecular size of the polymer chains in the photoresist imaging material. New experimental methods are needed to measure transport and materials science phenomena over nanometer length scales to provide critically needed data for the understanding, design, and control of new lithographic materials and processes. In collaboration with IBM and the University of Texas, we directly measured the spatial evolution of a reaction front, within a photoresist, with nanometer resolution using neutron and x-ray reflectometry and a deuterium-labeled photoresist polymer.

The semiconductor industry is rapidly approaching the need to fabricate sub-100 nm structures to continue performance increases in integrated circuits. Photolithography remains the enabling technology for the fabrication of integrated circuit patterns. Although industry is able to commercially produce 130 nm features, lithographic materials and processes are not fully available for the production of sub-100 nm structures. New materials must be able to produce structures with dimensional tolerances of (2 to 5) nm, dimensions near the size of the polymer chain molecules in the imaging layer.

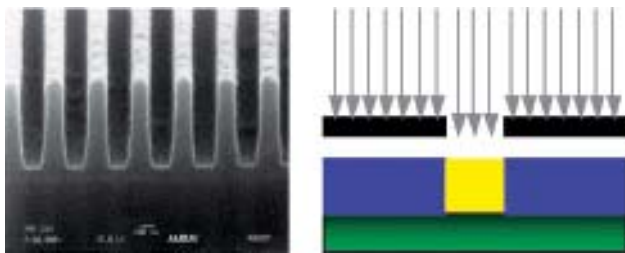


Figure 1: At left, SEM image of a lithographically fabricated structure with a nominal critical dimension of 150 nm and 300 nm pitch. At right, schematic illustration of patterning through a mask to create the structure.

Current imaging layers, chemically amplified photoresists, are multi-component materials consisting of a polymer resin initially insoluble in an aqueous base developer solution, a photoacid generator (PAG), and other additives. A schematic diagram of the fabrication process and an example structure are shown in Figures

1 and 2. The patterns are generated in the resist by exposure to UV radiation through a mask. In the exposed areas, the PAG decomposes forming an acid species. Upon baking, the acid diffuses and catalyzes a deprotection reaction rendering the insoluble resist soluble in a developer. The soluble regions are then removed with the aqueous base developer. Control over this process is dominated by the events in the transitional region between exposed and unexposed areas of the photoresist.

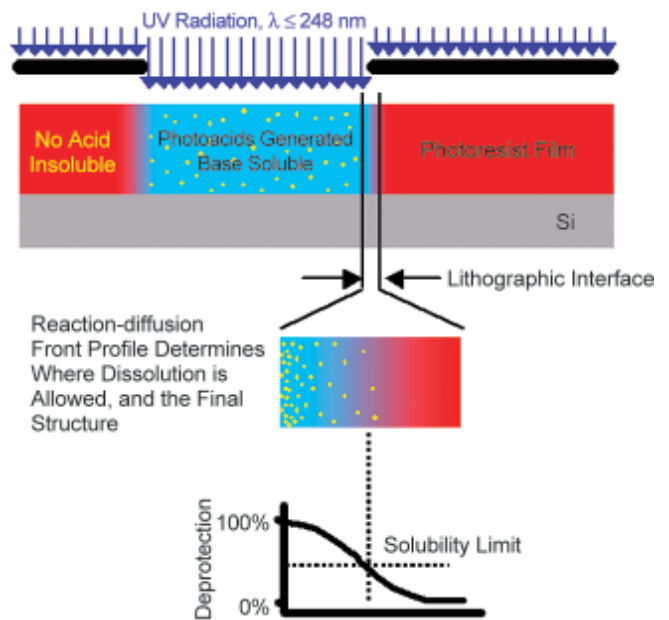


Figure 2: Schematic diagram of the reaction-diffusion process in chemically amplified photoresists. The transitional region between exposed and unexposed regions is particularly important for critical dimension and roughness control.

The initial development of chemically amplified photoresists was a key technological breakthrough furthering the continued use of optical photolithography for the fabrication of sub-micrometer features. The importance of chemically amplified photoresist concepts is illustrated by the industry-wide use of these materials in the fabrication of state-of-the-art devices today and into the foreseeable future. With the imminent need for sub-100 nm feature sizes, nanometer level control over the spatial evolution of the deprotection reaction front and the subsequent development steps is needed. The current level of understanding of the acid-catalyzed reaction-diffusion process is not sufficiently detailed to achieve this goal.

To meet the need for spatially detailed data, we have developed, in collaboration with the IBM T.J. Watson Research Center and the University of Texas at Austin, an experimental methodology to measure directly the spatial evolution of the deprotection reaction front through each processing step. By using model photoresist polymers with a deuterated protection group, neutron and x-ray reflectivity (NR, XR) measurements are able to follow the compositional and density profiles of the reaction-diffusion process in an idealized transitional region in a bilayer film stack. Neutron contrast with the reaction is possible because the reaction products involving the deuterated protection group are volatile as illustrated in Figure 3.

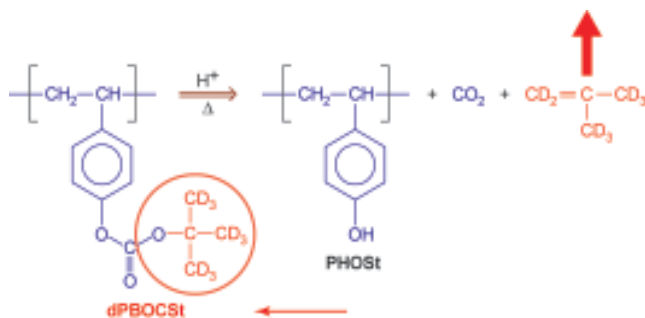


Figure 3: General deprotection reaction in a chemically amplified photoresist. Deuterated molecular parts with strong contrast to neutrons are shown in red. PHOSt = polyhydroxystyrene, PBOCSt = poly *p*-tert-butoxycarboxystyrene.

The NR and XR results from a series of bilayer samples are shown in Figure 4. NR and XR measurements were taken after each processing step from the spin-coating of each film layer through exposure and bake to the dissolution of the upper layer and any deprotected polymer. The data show that the deprotection reaction front broadens with time within the photoresist. The initial interfacial width was approximately 4 nm wide whereas the reaction front was nearly 20 nm wide. Upon development, the data show that the developed film remained sharply defined with a surface roughness of approximately 4 nm as well. Although the reaction front was much wider than the final interfacial width, the selectivity of the dissolution process allows for the fabrication of well-defined nanostructures with diffusive transport mechanisms.

The spatial detail afforded by the developed methodology can play an important role in not only the qualitative description of the reaction-diffusion process, but also with the quantitative determination of physical parameters and changes in any physical or chemical properties over the nanometer length scales required for

control over the fabrication of sub-100 nm structures. In addition, the strategy developed here is general and can be adapted for the study of candidate photoresist materials being developed for future applications.

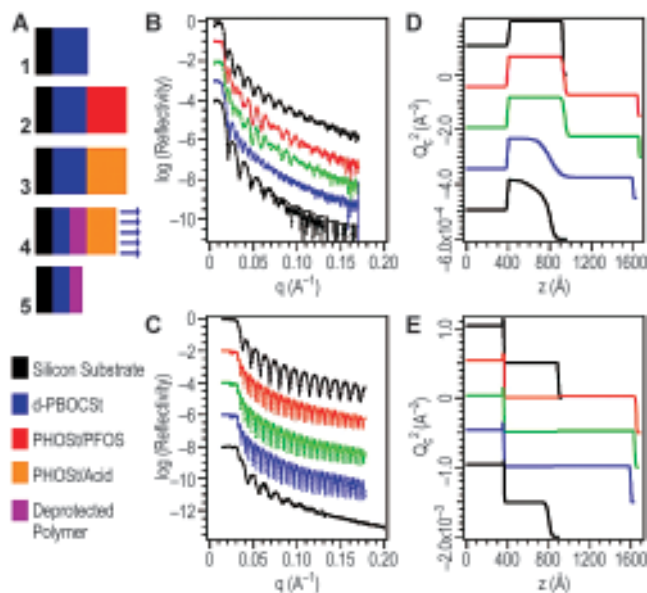


Figure 4: A) schematic diagram of the processing steps including the application of each film layer, exposure to UV radiation, a post-exposure bake (PEB) and development. B) and D) show the NR data and compositional depth profile and C) and E) show the XR data and density depth profiles from each step.

“[This work] opens a window of opportunity to construct structure-property relationships between chemical transport mechanisms and ultimate resist resolution. It may also lead to insights into the ultimate, intrinsic resolution limits and critical dimension control of polymer-based imaging materials.”

E. Reichmanis and O. Nalamasu
Bell Labs, Lucent Technologies,
Science, 297, 349, (2002)

For More Information on this Topic

E.K. Lin, C.L. Soles, R.L. Jones, J.L. Lenhart, W.L. Wu (Polymers Division, NIST); S.K. Satija (NCNR, NIST)

E.K. Lin, C.L. Soles, D.L. Goldfarb, B.C. Trinqué, S.D. Burns, R.L. Jones, J.L. Lenhart, M. Angelopoulos, C.G. Willson, S.K. Satija, and W.L. Wu, “Direct Measurement of the Reaction Front in Chemically Amplified Photoresists,” *Science*, 297, 372, (2002).

Nanoscale Structural/Compositional Characterization of Ultra-Thin Films

Many modern device structures are critically dependent on the properties of ultra-thin layers approaching 1 nm in thickness. Examples of such layers include interfaces and reaction layers and gate dielectrics in CMOS devices. As a result, comprehensive understanding of the structure (amorphous or crystalline) and the chemistry (composition, chemical bonding, etc.) of these ultra-thin films is one of the most important aspects of successful device engineering. The present work demonstrates the application of high-resolution transmission electron microscopy combined with spatially resolved electron energy-loss spectroscopy to the analysis of (i) silicon oxide-nitride-oxide heterostructures and (ii) zirconium oxide ultra-thin films on silicon.

Silicon oxynitrides are leading candidates to replace pure thermally grown SiO₂ as gate dielectrics because they suppress boron penetration from the poly-Si gate, enhance reliability, and reduce hot-carrier-induced degradation. At the same time, silicon oxide-nitride-oxide multilayers (ONO stacks) attract considerable interest as possible charge storage structures in non-volatile memory devices. The critical structural and compositional parameters that affect electrical performance of ONO-based devices include the physical density of the amorphous oxide/nitride layers and the depth distributions of both oxygen and nitrogen atoms. However, few systematic studies that analyze the effect of processing conditions on these parameters in stacked ONO structures have been reported.

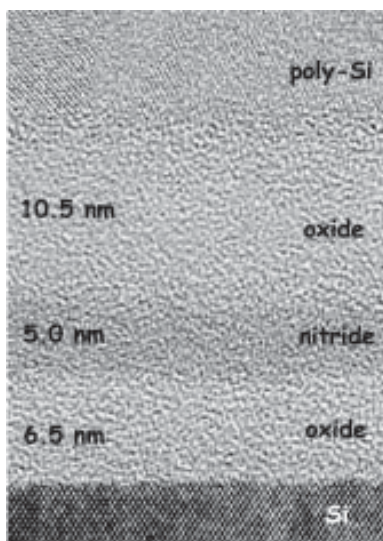


Figure 1: Typical high-resolution TEM image of an ONO stack.

In this study, we applied spatially-resolved electron-energy loss spectroscopy (EELS) in a transmission electron microscope (TEM) to analyze elemental distributions in differently processed ONO stacks (Figure 1) while physical densities of individual layers were measured using x-ray reflectometry. The results of structural/compositional analysis were correlated with the electrical performance of ONO-based flash-memories.

The ONO stacks for this study (Figure 1) were provided by Tower Semiconductor Ltd. Typical profiles of O-K and N-K characteristic intensity distributions, obtained using an imaging filter in a fixed-probe TEM, are shown in Figure 2. The O-K intensity decreases to the noise level in the middle of the nitride layer. The nitrogen signal disappears in the oxide layers, but produces small peaks both at the Si/SiO₂ and poly-Si/SiO₂ interfaces. The presence of nitrogen at the Si/SiO₂ interface in the oxy-nitride films has been reported previously, based on similar EELS measurements, and was attributed to nitrogen segregation during film processing. Such nitrogen segregation could explain the improved electrical breakdown strength of the bottom oxide observed after nitride deposition. However, we found that the amount of nitrogen at both interfaces

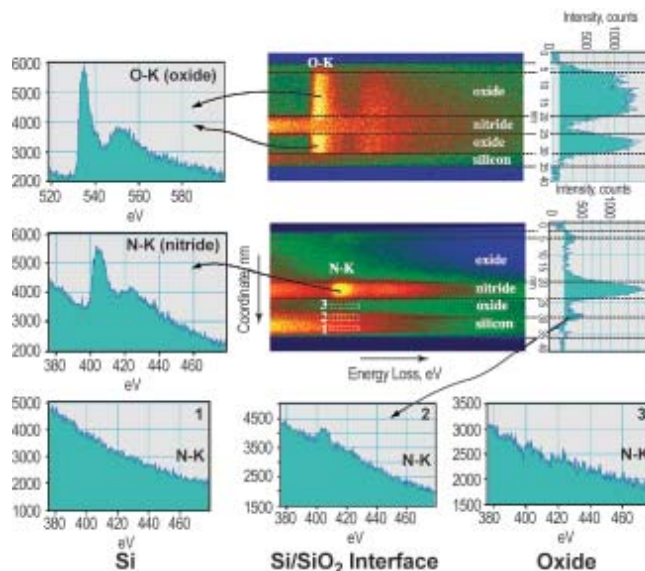


Figure 2: O-K and N-K spectrum-lines. The interfaces in the HRTEM image were set parallel to the energy-dispersion direction of the spectrometer. Each 2D spectrum has two dimensions: horizontal, corresponding to energy loss, and vertical, representing a spatial coordinate; that is, each 2D spectrum represents a collection of EELS spectra spatially-resolved across the interfaces. The individual spectra are shown on the left. The spectrum-lines were processed to remove background, and the intensities under each edge were integrated over an energy window of 2 eV. The profiles of integrated intensity distributions as a function of spatial coordinate are shown on the right.

increased with increasing irradiation time for the analyzed area, which suggested that the nitrogen distribution might be affected by the electron beam.

The effect of the electron beam on the nitrogen segregation was further tested using EELS spectrum-imaging in a dedicated scanning TEM (STEM). In these experiments, spectrum-images provided a collection of spatially-resolved (along the interface) line-scans across the ONO stack; the line-scans were separated in time by about 2.5 s. The first line-scan yielded no significant nitrogen signal at either the Si/SiO₂ or the poly-Si/SiO₂ interfaces. However, the next line-scan revealed a small, but detectable, nitrogen signal at the Si/SiO₂ interface, while the nitrogen signal from the nitride layer was reduced (Figure 3); the magnitude of this effect decreased with decreasing irradiation dose. These results suggest radiation-induced nitrogen segregation to both the Si/SiO₂ and poly-Si/SiO₂ interfaces.

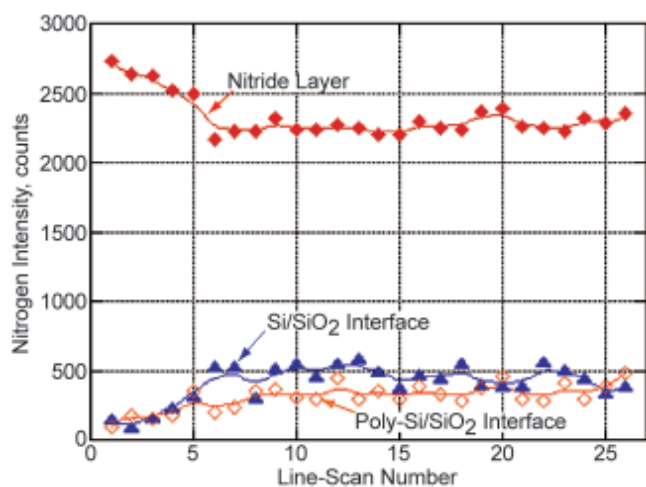


Figure 3: Integrated nitrogen intensity as a function of line-scan number in the EELS spectrum-image acquired in the dedicated STEM. The nitrogen signal at both Si/SiO₂ and poly-Si/SiO₂ interfaces increases significantly with increasing scan number. A corresponding decrease in the nitrogen signal from the nitride layer is consistent with the beam-induced nitrogen diffusion/segregation.

The implications of the beam-induced nitrogen segregation in the ONO stacks are several. First, similar artifacts could be present in other spectroscopic techniques that involve high-energy probes, such as secondary ion-mass spectroscopy (SIMS); therefore, the SIMS data on nitrogen segregation in ONO reported in the literature may need to be revisited. Second, reasons other than nitrogen segregation can be responsible for the improved dielectric properties of the bottom oxide observed after nitride deposition in the present ONO stacks. Additionally, our results indicate that electron-beam-induced damage can be a serious obstacle to EELS analysis at nanoscale resolution. More studies of radiation-induced damage in industrially relevant materials are needed to identify potential artifacts.

In another example, we applied TEM/EELS to the analysis of ZrO₂ ultra-thin films on silicon. Metal oxides, such as ZrO₂, are key candidates for gate dielectrics to replace SiO₂ and SiO_xN_y in CMOS transistor technology. Despite a large effort invested in the characterization of ultra-thin ZrO₂ films, many issues related to the effect of processing conditions on both morphology and thermal stability of ZrO₂ films on silicon remain the subject of a continuing debate. The present work is part of a systematic study of these effects in gate dielectrics, which is conducted in collaboration with the UCLA. The ZrO₂ films for this study were deposited using a state-of-the-art atomic layer CVD (ALCVD) system and subjected to annealing in different atmospheres. The high-resolution TEM images of 2.5 nm ZrO₂ films deposited on the HF-treated silicon surface are presented in Figure 4. The as deposited film is largely crystalline and exhibits a rough morphology; the latter was attributed to a discontinuous nucleation of the ZrO₂ film on the HF-treated Si surface. (A much smoother morphology was observed for films deposited on thermally grown 1 nm SiO₂ layer.) The film includes an interfacial layer having a thickness of about 1 nm. Spatially resolved EELS spectra indicate a lack of any significant Zr content in this layer, suggesting a silicon oxide rather than a silicate phase. Although the presence of a small amount of Zr in the layer still could not be ruled out, the near-edge structure of both the Si-L_{2,3} and O-K edges for this interfacial layer were also consistent with a silicon oxide.

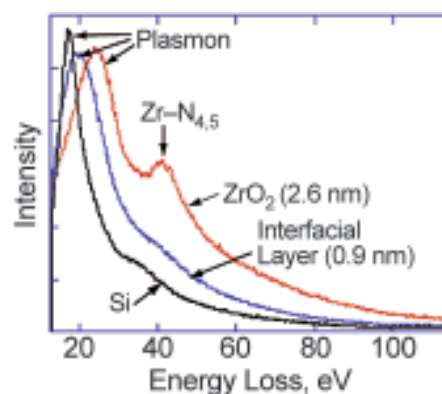


Figure 4: Upper: HRTEM image of a ZrO₂ film deposited on HF-treated silicon at 460°C. Lower: Spatially-resolved EELS spectra from the same area.

For More Information on this Topic

Contact: I. Levin

Advanced Metallizations for Sub-100 Nanometer Electronics

Electrodeposited copper is rapidly replacing aluminum in device interconnect technology because of its lower electrical resistivity, superior electromigration behavior, and the ability to fill fine features without the formation of seams or voids. As feature dimensions go below 100 nm difficulties in maintaining performance are anticipated. In FY2002 we have pushed the quantitative limits of the Curvature Enhanced Accelerator Coverage (CEAC) mechanism developed in the Metallurgy Division of NIST. Exploring the mechanism has yielded new electrochemical processing routes for improved metallization and is guiding the development of advanced metallizations beyond copper as well as new processing routes such as surfactant catalyzed chemical vapor deposition.

This Metallurgy Division project is meeting the microelectronics industry's need for improved device metallization by exploring advanced materials and processes for superconformal film growth. In FY2002 we have:

- Established the generality of the CEAC model for superfilling by electrodeposited silver and other metals;
- Developed a new processing method for eliminating the delay time for superfill to begin during electrodeposition, thereby increasing the aspect ratio and decreasing the width of trenches that can be superfilled; and
- Extended the CEAC mechanism to quantitatively predict superfill during chemical vapor deposition.

Our current measurement and modeling effort is focused on copper and silver metallizations, the latter metal having the lowest resistivity of any element, thus having potential on-chip applications. Superconformal

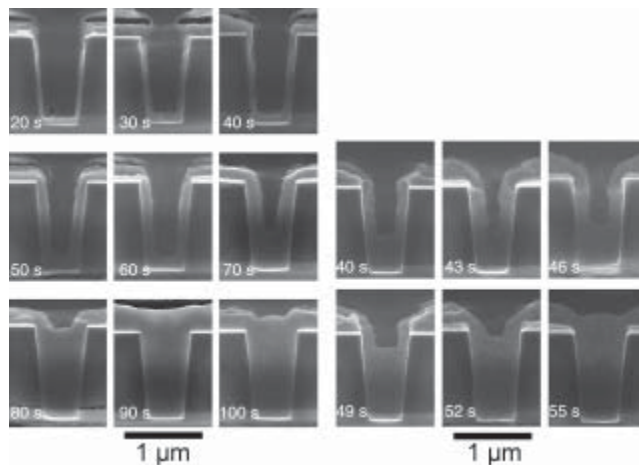


Figure 1: Superconformal filling of vias during silver (left) and copper (right) electrodeposition (NIST Metallurgy Division, using patterned wafers from International SeMaTech).

silver deposition was demonstrated this year in the Metallurgy Division and is the first example of superconformal feature filling with a metal other than copper. “Superfilling” is characterized by bottom-up deposition as shown in Figure 1.

Filling of trenches and vias with silver and copper is quantitatively explained by the Curvature Enhanced Accelerator Coverage Mechanism (CEAC) developed at NIST. Electrochemical and surface analytical measurements on planar substrates were used in FY2002 to establish a one-to-one correlation between catalyst coverage and the metal deposition rate. In the case of silver deposition, adsorbed selenium was found to catalyze the deposition rate. For the thiol/disulfide-polyether-halide additives used in copper superfilling, the sulfonate-end group of the thiol or group of the thiol or disulfide molecules was found to destabilize the passivating polyether surface film thereby accelerating the local metal deposition rate.

The insight provided by uncovering the CEAC mechanism has enabled the development of a new two-step process for superconformal film growth; in contrast to standard electrodeposition techniques, the catalyst is deposited on the substrate prior to the metallization. Specifically, the patterned substrate is first

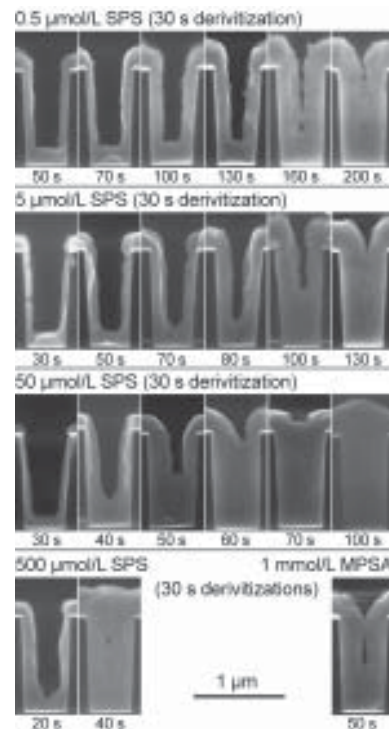


Figure 2: Time evolution of trench filling after different “derivitization” steps. The concentration of SPS or MPSA catalyst used for the 30 s surface derivitization steps are indicated. All specimens were transferred to a catalyst-free electrolyte for copper deposition.

“derivitized” or “dosed” with a submonolayer coverage of catalyst and then transferred for electroplating in an electrolyte that does not contain the catalyst. For an optimum catalyst coverage, superconformal filling of trenches and vias occurs as shown in Figure 2 (50 $\mu\text{mol/L}$ SPS). If the catalyst coverage is too low or high, conformal or subconformal deposition occurs, resulting in void formation during feature filling (0.5, 500 $\mu\text{mol/L}$ SPS, 1 mmol/L MPSA). The filling behavior is completely analogous to that obtained using a single (conventional) electrolyte containing both catalytic and inhibiting species. The new process provides unambiguous verification of the CEAC mechanism of superconformal film growth. Restricting the catalyst to the surface prior to metal deposition also enables the rate differentiation provided by the CEAC mechanism to be increased relative to the conventional process. From a technical perspective, the two-step process offers an interesting solution to the difficult control issues associated with catalyst destruction and related aging effects which are known to occur in the “conventional” single-electrolyte superfilling process currently used in industry.

The generality of the CEAC mechanism has now been extended to include the first quantitative prediction of superconformal chemical vapor deposition (CVD). More recently, this work has enabled a direct comparison of the CEAC mechanism with detailed experiment results on iodine catalyzed copper CVD as shown in Figure 3.

Project results from FY2002 have firmly established the generality of the Curvature Enhanced Accelerator Coverage (CEAC) mechanism, which we developed in FY2001 to explain superconformal electrodeposition of copper. The output also clearly demonstrates the predictive power of the CEAC formalism.

Three different electrode-shape change algorithms have been developed. They show excellent agreement with experimental results.

These algorithms, in the form of software, are available from the Metallurgy Division website and are currently being examined by Texas Instruments and IMEC. In addition, Motorola (B. Melnick and M. Freeman), International SeMaTech (C. Witt) and

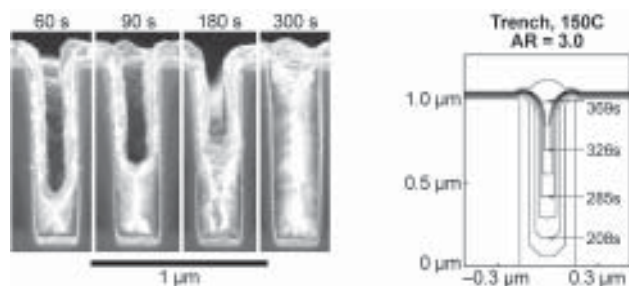


Figure 3: Superconformal filling of vias during iodine catalyzed chemical vapor deposition. Experimental via results are from Hynix Semiconductor, and model predictions for a trench are from the Metallurgy Division of NIST.

Hynix Semiconductor (S.G. Pyo) are now active collaborators in our experimental and modeling efforts. The first two provide patterned wafers for NIST electrodeposition studies; the last provides results from iodine catalyzed chemical vapor deposition experiments for NIST modeling.

Selected Project Publications for FY2002

D. Wheeler, D. Josell and T.P. Moffat, Modeling Superconformal Electrodeposition Using the Level Set Method, *J. Electrochem. Soc.*, submitted July 2002.

T.P. Moffat, D. Wheeler, C. Witt and D. Josell, Superconformal Electrodeposition Using Derivitized Substrates, *Electrochemical and Solid-State Letters*, submitted May 2002.

D. Josell, S. Kim, D. Wheeler, T.P. Moffat, S.G. Pyo, Superconformal Deposition by Iodine-Catalyzed Chemical Vapor Deposition, *J. Electrochem Soc.*, submitted May 2002.

B.C. Baker, M. Freeman, B. Melnick, D. Wheeler, D. Josell, T.P. Moffat, Superconformal Electrodeposition of Silver from a $\text{KAg}(\text{CN})_2\text{-KCN-KseCN}$ Electrolyte, *J. Electrochem. Soc.*, in press.

D. Josell, B. Baker, C. Witt, D. Wheeler and T.P. Moffat, Via Filling by Electrodeposition: Superconformal Silver and Copper and Conformal Nickel, *J. Electrochem. Soc.*, in press.

T.P. Moffat, B. Baker, D. Wheeler, J.E. Bonevich, M. Edelstein, D.R. Kelly, L. Gan, G.R. Stafford, P.J. Chen, W.F. Egelhoff, and D. Josell, Superconformal Electrodeposition of Silver in Submicron Features, *J. Electrochem. Soc.* 149, C423 (2002).

D. Josell, D. Wheeler and T.P. Moffat, Superconformal Electrodeposition in Vias, *Electrochemical and Solid-State Letters* 5, C49 (2002).

D. Josell, D. Wheeler and T.P. Moffat, Superconformal Deposition by Surfactant-Catalyzed Chemical Vapor Deposition, *Electrochemical and Solid-State Letters* 5, C44 (2002).

D. Josell, D. Wheeler, W.H. Huber, J.E. Bonevich and T.P. Moffat, A Simple Equation for Predicting Superconformal Electrodeposition, *J. Electrochem. Soc.* 148, (12) C767 (2001).

Our findings have also been conveyed to U.S. industry, academia and other national laboratories through more than ten external presentations in the last year.

For More Information on this Topic

D. Josell, D. Wheeler, B. Baker, T.P. Moffat

Carbon Nanotubes: Characterization and Application for Nanometer Scale Devices

The Materials Reliability Division believes that research on carbon nanotubes and their applications can significantly support economic opportunities in nanotechnology. Carbon nanotubes have a unique set of characteristics that offer promise for a variety of nanometer scale applications. The carbon-carbon bond is among the strongest known atomic bonds, and produces amazing mechanical strength. Because of their outstanding thermal conductivity, nanotubes are also being considered for thermal transport applications. In addition, recent reports envision nanotubes performing multiple functions in future computers: both as switching elements and as interconnections. We are, therefore, developing nanometer scale measurement, manipulation, and bonding techniques to enhance future nanometer scale devices.

Technical Description

The Materials Reliability Division has begun research on carbon nanotubes in two application areas: as probes in advanced imaging and as materials for mechanical and electrical structures. Starting this research required us to develop an understanding of the different types of nanotubes available, their sources, and techniques for handling them. Because nanotubes are such new materials, and new to this Division, a brief introduction is given.

Carbon nanotubes are essentially graphite sheet structures that are rolled into tubes. They can be single sheet tubes, referred to as single-walled, or they can be multiple concentric tubes, referred to as multi-walled. Several types of nanotubes are available commercially in quantities of the order of a gram. One manufacturer's catalog lists five types of multi-walled nanotubes and one type of single-walled. The type that we used for probe tips for atomic force microscopy (AFM) differs slightly. These are a number of multi-walled nanotubes twisted together and referred to as nanotube ropes. These ropes are large enough to view in an optical microscope. Figure 1 shows various diameter multi-walled nanotubes.

Accomplishments

This year, FY02, we have developed methods to handle the nanotubes and used them in several experiments. We have attached nanotubes to an AFM probe, to map surface conductance on a nanometer scale, and to a mechanical strain-testing device mounted in a scanning electron microscope (SEM) that allows imaging of the nanotube as it is strained. We have also joined with the Electronics and Electrical Engineering Laboratory to

explore the high-frequency response of nanotube AFM probes. Within the Division, we are also working on multiscale modeling, so that designers can model, for example, the effect of imposed deflection on the attachment of a nanotube to its mount within some device.

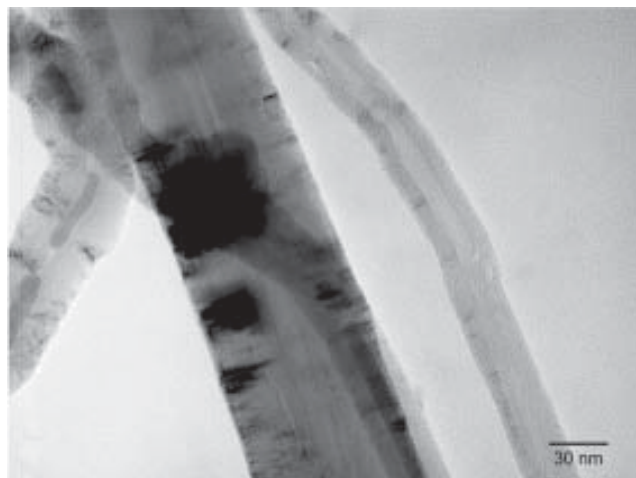


Figure 1: Transmission electron microscope (TEM) image showing multi-walled nanotubes of different diameters. These are large-diameter tubes, from a set obtained for testing as AFM probes. Single-walled tubes are much smaller, from 1 to 5 nm in diameter.

Developing the manipulation and attachment processes has required the largest effort so far. To attach the tubes, the first handling step is to remove impurities from the bulk nanotubes with solvents. Next a drop of solvent with nanotubes is dispensed on a substrate such as a glass slide and allowed to dry, leaving the tubes lying flat. Adhesive tape is then used to pick up and hold several nanotubes for access and manipulation under the optical or scanning electron microscope.

The next operation is to prepare the target to which the nanotube will be attached. The target is mounted on a micromanipulator. We have used a micromanipulator controlled by manual micrometers under an optical microscope and one driven by piezo-stepper motors in the SEM. To practically view thick-walled nanotubes optically, an optical microscope, with a very long working distance and a very bright oblique illuminator, was obtained.

To mount a nanotube to an AFM tip under the optical microscope, the AFM tip is mounted on the micromanipulator and then touched to a carbon impregnated conductive adhesive. A small submicrometer-sized bead of adhesive is subsequently attached to the tip as it is pulled away. The AFM tip is

then positioned to an appropriate nanotube, and the nanotube is applied to the tip. A nanotube rope attached to an AFM tip is shown in Figure 2. The bead of adhesive can be seen at the end of the pyramidal AFM tip. From this image it is clear that the sensing portion of the nanotube is much smaller than the end of the AFM tip. Claims of an order of magnitude increase in image resolution have been reported in the literature.

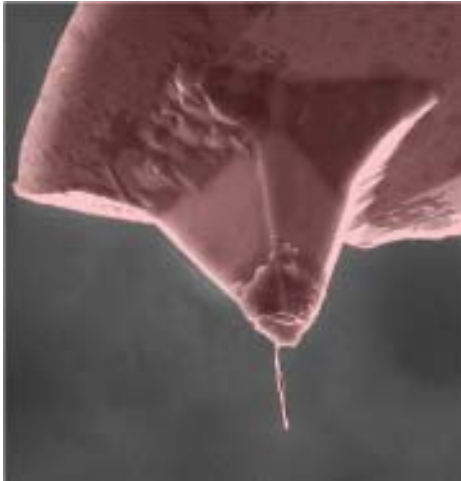


Figure 2: Scanning electron microscope (SEM) image of nanotube attached to an AFM tip with applied adhesive. The nanotube is actually a rope of several tubes about 100 nm in diameter.

Attaching nanotubes in the SEM begins with a sharp tungsten probe mounted in a piezo-driven micromanipulator. The tungsten probe is brought in contact with the nanotube, and the electron beam is focused and left stationary where the two come together, producing a carbonaceous deposit. This technique, called electron beam deposition (EBD), produces a strong bond on the nanometer scale. Next, the nanotube



Figure 3: SEM image of tungsten probe (bottom of image) attaching a 20 mm long nanotube rope to the end of an AFM tip (upper left) using EBD. After this nanotube rope was attached, it was pulled until the tube separated from the tungsten probe.

is moved to the AFM tip or other device for attachment, again using EBD to bond the two together. We have made preliminary tensile measurements using this procedure by viewing the deflection of the AFM cantilever as the tungsten probe is pulled away from the AFM cantilever. We have found the EBD bond can survive micronewton forces (Figure 3).

Microelectrical mechanical systems (MEMS) are developing rapidly. Nanotubes can be used with MEMS as mechanical and electrical components. Mechanical and electrical characterization of the bonding techniques is critical to developing the full potential of nanotubes on MEMS. We can easily apply the micromanipulation procedures we have developed to test various bonds (Figure 4).

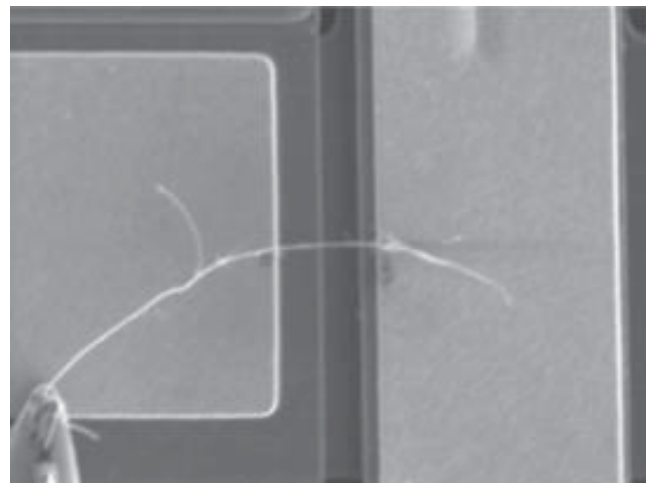


Figure 4: SEM image of attaching a nanotube to a MEMS device, in progress. Development of carbon deposits can be seen near the edges of the MEMS under the nanotube. The nanotube rope is about 100 nm in diameter. The tip of the tungsten probe that maneuvers the nanotube can be seen in the lower left corner of the image.

Future Research

More details on our research on the use of nanotubes as probes in advanced imaging appears later in this report. Future research on nanotubes as mechanical materials includes developing systematic procedures for mechanical measurements on nanotubes of different types. In addition, we plan on applying these attachment techniques to mechanical measurements of other submicrometer tube or fiber-like materials, such as collagen fibrils, and developing a practical modeling capability for nanotube-device attachments.

For More Information on this Topic

P. Rice, D. Read

Performance-Limiting Defects in GaN

The III-V nitrides and GaN, in particular, are emerging new semiconductors for electronic devices, including light-emitting diodes (LED) and laser diodes in the blue-green and UV wavelengths, UV detectors and ultrahigh power switches. The main challenges in this technology are optimization of optical output efficiency and stability of metal contacts. One objective of the MSEL project on GaN is to quantify the effect of GaN defects, in particular of threading dislocations, on these properties. In FY2002 a mechanism for the degradation of electrical contacts through threading dislocation-mediated phase transformations was determined through detailed characterization using transmission electron microscopy. Doping methods to disable the mechanism may lead to greatly improved stability, reliability, and performance of commercial GaN devices.

Direct bandgap GaN and its alloys with AlN and InN are receiving considerable attention as promising semiconductors for electronic devices operating at high temperatures, high frequency and high power and for optoelectronics applications in the blue-green and UV wavelengths. Therefore, electrical contacts to the nitrides (ohmic contacts and Schottky barriers) which are stable at elevated temperatures are needed.

As bulk crystals of these materials are not available, GaN is epitaxially grown on a substrate, usually on (0001) sapphire or (0001) 6H-SiC. Because of a large lattice mismatch between the substrates and GaN, high densities of various crystallographic defects are present in the active GaN layers. Among the defects that can cross the epitaxial GaN layer and reach a surface are threading dislocations, inversion domains, nanopyes and prismatic planar defects.

In order to achieve desirable characteristics of ohmic contacts, different combinations of different metal layers have been studied. For example, the commonly accepted contact to p-type GaN is Ni/Au which gives good electrical characteristics after annealing at 400-600°C. For higher temperatures, the electrical characteristics worsen and severe degradation of contact morphology is observed. Degradation of such electrical contacts are associated with dislocations in GaN, island formation in the contact layers, and decomposition of GaN. In FY2002, NIST developed a mechanism for contact degradation that is based on heterogeneous nucleation of GaN decomposition at threading dislocations/metal interface, followed by wetting of the threading dislocation by liquid Ga. The morphology of the metal/GaN interface is an important issue: if the Ga metal were to penetrate through a thin GaN layer and reach an

underlying layer in a device, the device could be rendered inoperable. Furthermore, the stability of interfacial morphology is a general concern for contacts to all semiconductors.

Reaction and interdiffusion in the Au/Ni/GaN system as a function of annealing temperature from 400 to 900°C has been investigated by several groups, mostly using Rutherford backscattering (RBS), Auger spectroscopy and x-ray scattering. Only rarely has this microstructural evolution been directly observed using transmission electron microscopy (TEM). In collaboration with researchers from the Electrical Engineering Department at Howard University, we investigated electrical and microstructural behavior of Ni/Au bilayers as a function of annealing temperature, with emphasis on structural evolution at a TEM level. The as-deposited layers consisted of 50 nm of Ni and 35 nm of Au, with Ni in contact to n-type GaN. Ohmic contacts with a specific contact resistivity, ρ_s , as low as $6.9 \times 10^{-6} \Omega\text{-cm}^2$ for a doping level of $5.0 \times 10^{17} \text{ cm}^{-3}$ were obtained after annealing the sample for 10 s at 800°C. Two very important conclusions were achieved from the TEM investigation:

1. A strong reaction between the metal contact layer and the threading dislocations core structure leads to decomposition of GaN along dislocation lines. Such behavior will be a major factor limiting annealing temperature and operation temperature/time of devices.
2. Interdiffusion between Ni and Au results in reversal of Au and Ni phases across the metal film. Thus, after annealing the phase primarily responsible for the formation of the energy barrier of the contact between GaN and metal contact is Au-based.

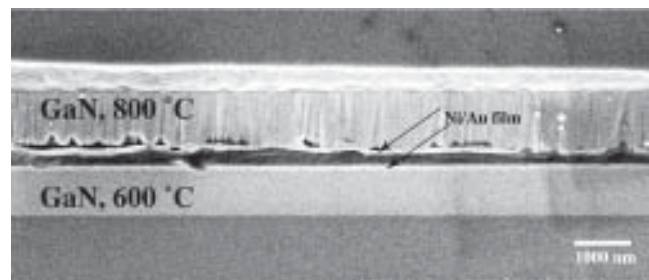


Figure 1: SEM image of Au/Ni/GaN/sapphire annealed at 600 and 800°C for 10 sec.

Figure 1 shows a SEM image of Au/Ni/GaN annealed at 600 and 800°C for 10 sec. For the imaging, we used a cross-sectional ion milled TEM specimen where two differently annealed specimens were glued face to face. Whereas at 600°C the metal film is continuous, at 800°C severe degradation of the metal contact occurred. In many places the film is

separated from GaN, and deep V-shaped pits can be found penetrating GaN. Such pits are detrimental to the near-surface electrical performance of devices.

TEM analysis of these specimens showed that the V-shaped pits are always associated with the threading dislocations. Figure 2 shows bright and dark field images of the 600°C-annealed specimen. The pits are clearly seen in the bright field image and marked by triangles. The weak beam imaging using different g-vectors established that each pit is connected to a place where a threading dislocation exits GaN. The threading dislocations vary in character (e - edge, s - screw and m - mixed).

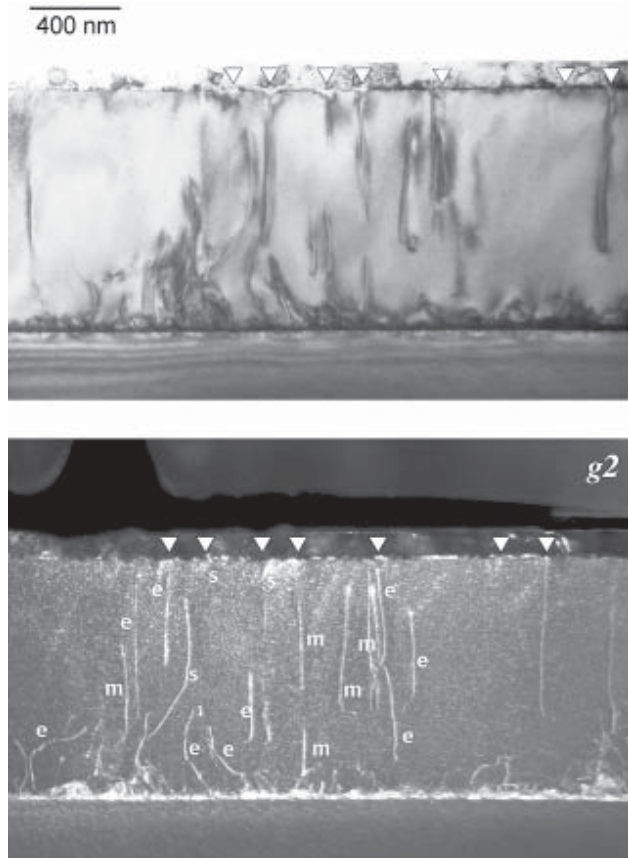


Figure 2: Bright field (upper) and weak-beam dark field (bottom) images of the 600°C-annealed specimen.

Bright and dark field images of the 800°C-annealed specimen are shown in Figure 3. The pits associated with the threading dislocations in the specimen are significantly deeper and wider. The metal film in some places is lifted from the GaN surface, and in other places, the surface of GaN is exposed. It appears that the surface of GaN, between the dislocations, was not degraded and remained flat (see arrows in Figure 3).

This phenomenon, the elevated temperature chemical instability of GaN defects exposed to either metal films

or free surfaces, is very general in nature and has importance for GaN-based device design. Bulk GaN has the following decomposition reaction above 800°C: $\text{GaN} \rightarrow \text{Ga(l)} + \text{N}_2(\text{g})$. Nevertheless, GaN films can survive higher temperatures due to the high stability of the (0001) surface. In addition, the reaction is sluggish due to kinetic difficulties recombining nitrogen atoms into N_2 molecules on the GaN surface. At locations where a dislocation exits GaN, the atomic arrangement is of lower stability and therefore triggers the decomposition of GaN (Figure 4). Nitrogen atoms may diffuse into the metal, recombine into molecules and form N_2 gas. Such gas accumulates under the metal film and exerts enough pressure to cause metal film de-cohesion (see Figure 3).

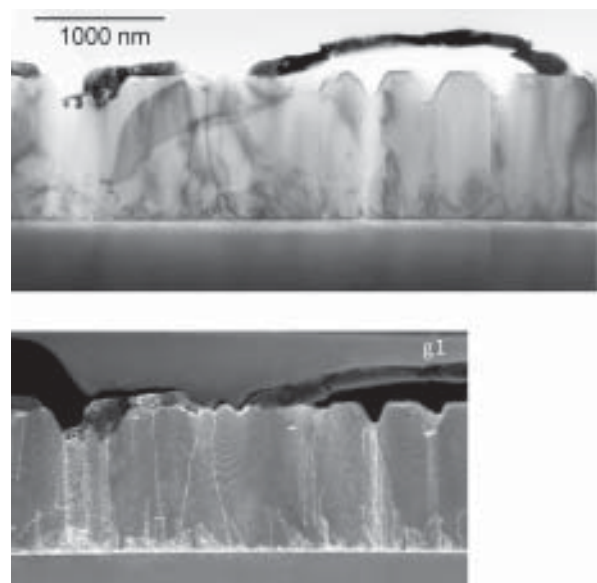


Figure 3: Bright field (upper) and weak-beam dark field (bottom) images of the 800°C-annealed specimen.

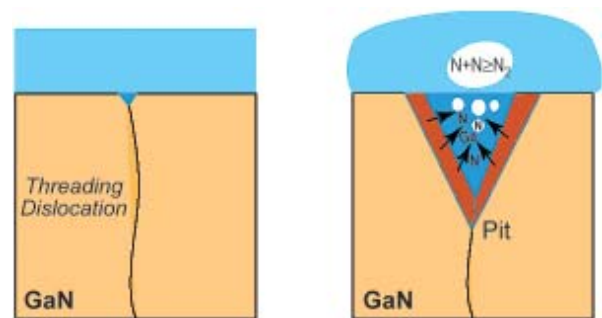


Figure 4: Schematic drawing illustrating decomposition of GaN along a dislocation line and resulting in the formation of N_2 .

For More Information on this Topic

L.A. Bendersky, A.V. Davydov, W.J. Boettinger

Strain in Compound Semiconductor Photonic Systems

The photonics technology industry develops products that often contain strain. Sometimes the strain is intentionally introduced, as in the case of highly strained quantum wells, while at other times it is undesirable, as in the case of oxide-confined vertical cavity surface-emitting lasers (VCSEL)s. Industry seeks to better understand and control strain development in such systems. We approach this problem in the Materials Reliability Division with two efforts — one concentrating on high spatial resolution measurement of strain using electron microscopy methods; and the other on theoretical modeling of development of strain energy during heterostructure growth using Green’s Functions and related boundary element methods.

Background

Strain is a major factor in the compound semiconductor photonics industry. It can be intentionally used for the self-assembly of quantum dots (QDs) or for tuning the energy band structure of heteroepitaxial layers. Deleterious effects of strain can lead to delamination of buried oxide apertures in vertical cavity surface-emitting lasers (VCSELs) or shifting of operating wavelengths for InGaAsP/InP-based devices.

We have begun an effort, which is partially ATP-funded, to understand and control strain development in III-V semiconductor materials systems. One aspect of the work involves developing experimental methods for measuring elastic strains with spatial resolution in the range of tens of nanometers. This involves the use of electron diffraction in the scanning electron microscope (SEM) and also in the transmission electron microscope (TEM). At present, this is being applied to strains induced by phase transition arising from the wet oxidation of AlGaAs layers confined between GaAs layers. Such oxides are used as optical apertures for VCSELs and, upon formation, result in volumetric compressive strains in the semiconducting layers in excess of 6%.

The second aspect of our contribution to solving this problem is to develop a multi-scale theoretical method for modeling the self-assembly of InAs QDs on GaAs substrates. This involves the combined use of Green’s functions (GF) and boundary element methods (BEMs) incorporating anisotropic elasticity. Strain, in this case, occurs from the mismatch in natural lattice parameters between the two materials. We determine both numerically and analytically the elastic strain energy distribution in these systems. A nice aspect of the work is that we are able to provide experimental data for direct incorporation into the theoretical model using electron microscopy, due to the well-defined conditions often present during epitaxial growth of crystals.

Strain Measurement with Electron Diffraction

We describe the SEM method of electron backscatter diffraction (EBSD) here due to some recent advances in our lab. The advantage of using a SEM method over a TEM method for strain determination lies primarily with the fact that less specimen preparation is required. This reduces the likelihood of significantly changing the initial strain state and, therefore, removes the need to model the preparation-induced relaxation. The main disadvantage of the SEM method is that strain sensitivity is not as good (detectability $\sim 0.1\%$ at best) as that possible by use of TEM. We estimate the EBSD spatial resolution for strain measurement in these systems to be ~ 50 nm.

Figure 1 shows a cross-sectional SEM image of an AlGaAs/GaAs multilayer structure, with an aluminum oxide layer partially grown in. The diffuseness of the EBSD patterns is an indication of the amount of strain present around the oxide growth front. More specifically, pattern diffuseness is a direct measure of the magnitude of the elastic strain gradient present within the sampling volume of the electron beam. The strain is greater near the growth front. With automated beam scanning and pattern collection, we are able to determine the spatial extent of the distortion field caused by the oxidation. Preliminary measurements suggest that the distortion field associated with a single oxide layer extends more than $1\ \mu\text{m}$ beyond the position of the front. The diffraction measurements are made only in crystalline portions of the specimen and, hence, do not sample the oxide strain directly, but rather the resulting effect on AlGaAs and GaAs layers in the vicinity.

More quantitative determinations of elastic strain are made by measuring the widths of the bright bands visible in the EBSD patterns, as shown in Figure 2. One bandwidth is directly proportional to the Bragg angle for the diffracting planes.

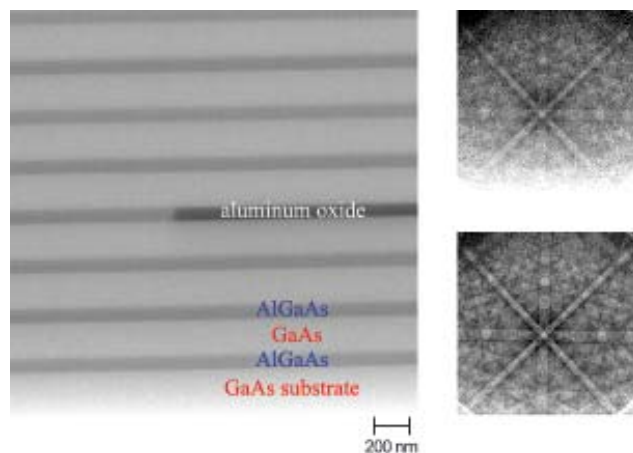


Figure 1: SEM image of multilayer structure, with oxide growth front visible. EBSD patterns obtained from positions indicated by line segments. Image to far right is an indexed pattern. Scale bar = 200 nm.

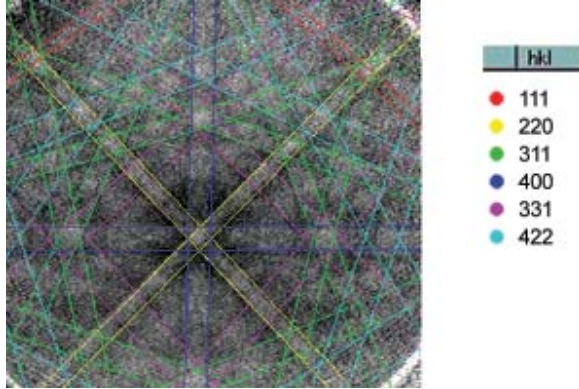


Figure 2: Indexed EBSD pattern used for elastic strain determination.

Energetics of Self-Assembly of Quantum Dots

We are developing advanced theoretical techniques using Green's functions (GF) and boundary element methods (BEMs) to model the self-assembly of arrays of quantum dots in anisotropic semiconductors. We consider the energetics of growth of a small QD in the strain field of an existing "grown" QD. We introduce a new parameter Γ , the elastic energy release rate (EERR), that determines the growth of a QD. The EERR, as in fracture mechanics, is defined as the elastic relaxation energy per unit volume of growth and is given by dW/dV_{QD} , where W is the elastic strain energy and V_{QD} is the volume of the growing QD. Assuming uniform misfit strain in QDs,

$$W = \frac{1}{2} \int_{\partial D} T_i u_i dS - \frac{1}{2} \sum_{n=1}^N \int_{\partial \Omega_n} (C_{ijkl} \varepsilon_{ij}^0 n_l) u_k dS + \frac{1}{2} \int_D C_{ijkl} \varepsilon_{ij}^0 \varepsilon_{kl}^0 dV, \quad (1)$$

where the first term is the work done by external traction, the second term is the work done by the intrinsic traction at the boundary of QDs, and the last term represents the energy of the reference state.

We use eq. (1) to evaluate W by using GF and a special BEM that requires numerical discretization only along the boundaries of the uncapped QDs and the interfaces between the substrate and QDs. Our BEM is computationally more efficient than the conventional BEM and the domain-based numerical techniques such as the finite-element method.

Equation (1) takes into account the strain created by the growing QD. This effect has been neglected in the earlier papers that consider only the strain field of the "grown" QDs. Equation (1) also accounts for the fact that the material parameters of QDs are different from the host solid and include the continuity conditions at the interface between QDs and the host solid. These contributions have been neglected in earlier calculations using Green's functions.

We have applied our theory to InAs QDs in GaAs. We have calculated EERR for a QD growing on the free (001) surface for a buried seed dot as well as a seed dot on the surface (Figure 3). We find that the grown QD reduces the EERR of a new QD. For the grown QD at the surface, the EERR for the new dot is lower in the $\langle 100 \rangle$ and $\langle 010 \rangle$ directions. However, the change in EERR is small when the grown QD is at the surface. In contrast, the effect of a buried QD on EERR of the new QD is very pronounced.

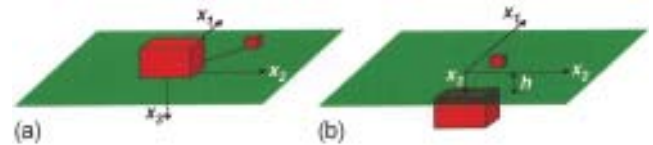


Figure 3: Formation of a new QD under the influence of a grown surface QD (a) or buried QD (b).

We find that the maximum of EERR occurs vertically above the grown QD only for some values of the depth of the QD (Figure 4). This shows that, for QDs covered by a thick spacer medium, a vertical array of self-assembled QDs is energetically favorable. In the case of a thin covering, an oblique stacking of QDs could occur. We also find that there is an optimum depth of the buried QD for the formation of a new QD vertically above it.

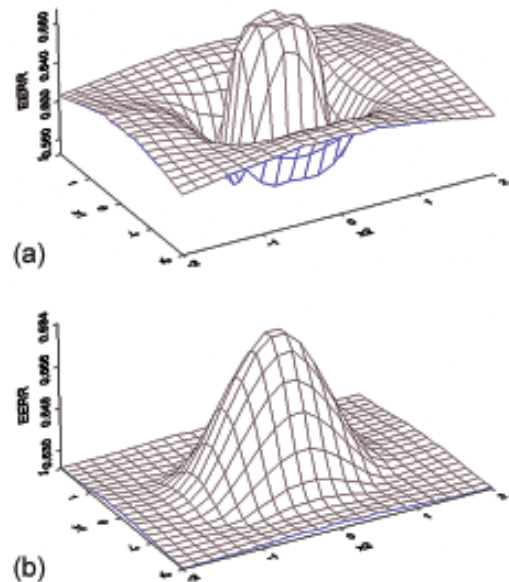


Figure 4: Variation of the EERR for formation of a new QD with locations at different depths of the buried QD (Figure 3b): (a) $h = 0.1a$; (b) $h = 0.6a$.

For More Information on this Topic

Electron diffraction strain measurement: R.R. Keller;
GF/BEM modeling: V.K. Tewary

Magnetization Dynamics in Films with Nanometer Scale Microstructure

Magnetization damping is essential for data storage and retrieval at GHz data rates in disk drives, MRAM chips and other magnetoelectronic devices. In disk drives, the write head materials, media and read head must all be able to perform well on nanosecond time scales. For measurement of magnetic damping parameters, ferromagnetic resonance (FMR) is the dominant technique, but the raw linewidth data is often clouded by the presence of inhomogeneities. Our modeling of ferromagnetic resonance spectra in inhomogeneous thin films takes a novel approach to a problem that for several decades has been solved only for weak inhomogeneities. Our new model involves solving for the normal modes of an inhomogeneous film and calculating the absorption spectrum from all of the modes. This model provides the theoretical basis for studying the intrinsic damping processes through FMR linewidth measurements, and ultimately for delivering the needed data on magnetic damping to industry.

Magnetic data storage has become the most prevalent form of data storage in the world, far surpassing paper documents in worldwide capacity. Annual hard drive storage capacity shipped is approximately 1×10^{19} bytes with a 60% per year growth rate. To handle anticipated storage at GHz data rates, it is important to understand and control magnetization damping, the process that allows magnetization to come to equilibrium by dissipating heat. To develop high-data-rate hard drives, it will be important to understand and control damping in the magnetic materials used in write heads, media and in read heads. For magnetic random access memory (MRAM) chips, damping is a limiting factor for the speed of these chips because reliable switching of the magnetic “bit” requires waiting for the magnetization to come to equilibrium before the next switching event.

The Nanomagnetodynamics Project is a cooperative project between the Metallurgy Division in MSEL and the Magnetic Technology Division in EEEL. The work is designed to address magnetization dynamics, and magnetization damping in particular, and to deliver to industry the data and metrology needed to develop high-data-rate magnetic devices. This highlight describes a recent theoretical breakthrough by MSEL staff that will enable reliable magnetization damping metrology.

The primary measurement used to determine the damping properties of magnetic materials is ferromagnetic resonance (FMR) linewidth. Ferromagnetic resonance, like electron spin resonance (ESR) and nuclear magnetic resonance (NMR) involves precession of the magnetization around an equilibrium direction at a frequency that depends on the applied field. The damping rate is determined from

the width of the susceptibility peak corresponding to the magnetization precession frequency as illustrated in Figure 1.

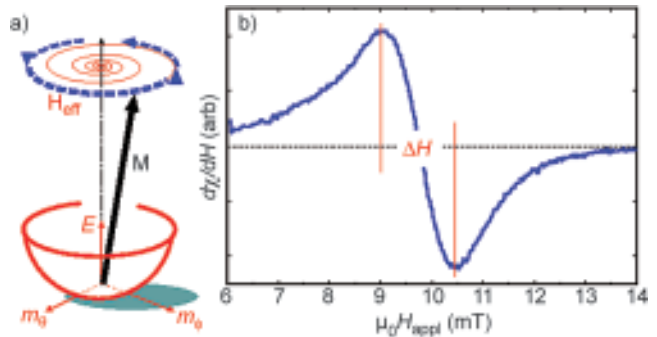


Figure 1. a) Magnetization precession. Damping causes the magnetization to come to equilibrium as shown by the red spiral. b) A typical FMR signal, taken at 2.5 GHz in a 10 nm thick film of Permalloy. Damping is measured through the line width ΔH .

Measurements of damping in ferromagnetic materials are complicated by the fact that in addition to damping, inhomogeneity contributes to the FMR linewidth. Reliable interpretation of FMR linewidth data therefore requires separation of the linewidth into components arising from damping and inhomogeneity.

Unlike ESR and NMR in paramagnetic materials, the spins in ferromagnetic materials are strongly coupled by short-range exchange interactions and long range dipolar interactions. To account for magnetic interactions, it is convenient to describe the vibrations of the magnetization in terms of spin waves, or in quantum mechanical language, “magnons.” Spin waves (magnons) are the collective vibrational normal modes of the magnetization in a uniform film just as sound waves (phonons) are the collective normal modes of a uniform crystal lattice. The analogy with sound waves is useful in describing the interaction of spin waves with defects. If a sound wave encounters a defect where the elastic properties are different, a portion of the incoming sound energy will be scattered into sound waves traveling in different directions, but with the same frequency. For spin waves, the uniform precession that is driven by a microwave field in an FMR experiment can be scattered into short-wavelength spin waves with the same precession frequency as the uniform mode. The quantum mechanical Hamiltonian describing a system with defects can be written

$$H = \hbar \sum_{\mathbf{k}} \omega_{\mathbf{k}} a_{\mathbf{k}}^{\dagger} a_{\mathbf{k}} + \hbar \sum_{\mathbf{k}} (A_{\mathbf{k},\mathbf{k}'} a_{\mathbf{k}}^{\dagger} a_{\mathbf{k}'} + A_{\mathbf{k},\mathbf{k}'}^* a_{\mathbf{k}} a_{\mathbf{k}'}^{\dagger})$$

where $a_{\mathbf{k}}^{\dagger}$ and $a_{\mathbf{k}}$ are the magnon (or phonon) creation operators for waves at frequency $\omega_{\mathbf{k}}$ and $A_{\mathbf{k},\mathbf{k}'}$ is a coefficient describing the strength of the defect that produces scattering.

The “two-magnon” model was first derived in the 1950’s to describe the effects of defects on linewidth measurements in bulk ferrite materials. Until the present work, it was the most sophisticated model of inhomogeneities in FMR.

The physical picture presented by the two magnon model is that inhomogeneities cause energy to be transferred from the $\mathbf{k} = 0$ uniform precession mode to other $\mathbf{k} \neq 0$ spin wave modes having the same frequency. The two-magnon model is expected to be valid when the spin wave amplitudes are small compared to the uniform precession amplitude, so scattering from spin wave modes back to the uniform precession mode is weak and spin wave–spin wave interactions are not important.

Our approach to the problem of ferromagnetic resonance in inhomogeneous thin films treats the very common case where the $A_{\mathbf{k},\mathbf{k}}$ coefficients are too large for the two-magnon model to be valid. To do this, we start with the Hamiltonian for films with inhomogeneities given above and find the eigenmodes and eigenvalues directly. This process involves constructing a model microstructure of the film, calculating the $A_{\mathbf{k},\mathbf{k}}$ coefficients, limiting the Hamiltonian to approximately 1000 spin wave modes and computationally diagonalizing the Hamiltonian matrix having elements $A_{\mathbf{k},\mathbf{k}} + \omega_{\mathbf{k}}\delta_{\mathbf{k},\mathbf{k}'}$.

The resulting eigenmodes of the inhomogeneous film are mixtures of the spin waves and the uniform, $\mathbf{k} = 0$ precession mode. Each eigenmode has a finite coupling to a uniform driving field that depends on the amount of the $\mathbf{k} = 0$ mode that it contains. Figure 2 shows the eigenmode spectrum and an eigenmode for a typical calculation.

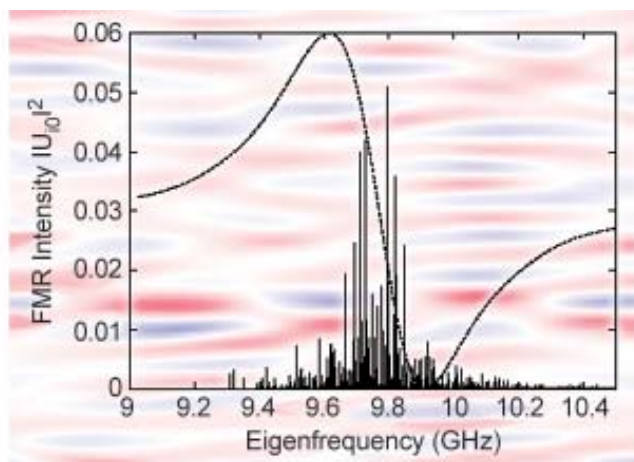


Figure 2: Eigenmode spectrum of an inhomogeneous thin film. Each eigenmode couples directly to the uniform FMR driving field to give the simulated FMR spectrum shown. The background image is the magnetization pattern corresponding to one of the eigenmodes. The image width is 5 μm and the defect size is 20 nm.

The physical picture presented by this model is very different from that of the two-magnon model.

Inhomogeneities do not merely couple the spin wave modes, they cause mixing of the spin wave modes into a new set of eigenmodes, each of which is observable in an FMR experiment. In this picture, it is clear that the linewidth caused by inhomogeneities is due to a spreading of the FMR intensity in frequency, not to any additional damping process.

Figure 3 shows a comparison between our eigenmode calculation, the two-magnon model and experimental linewidth measurements for a 20 nm film of Permalloy deposited on polycrystalline NiO. The coupling to antiferromagnetic NiO produces an inhomogeneous “exchange bias” field and a uniaxial anisotropy field that varies in strength and direction from grain to grain. These intentionally created “defects” are turned off by deposition of a thin layer of Ta on the NiO, decoupling it from the Permalloy.

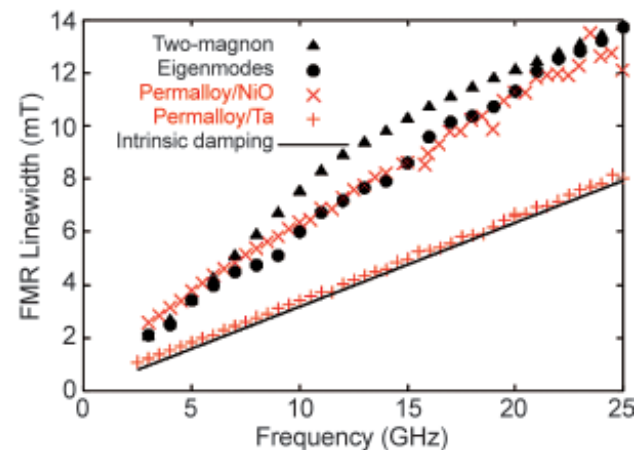


Figure 3: Comparison of the two-magnon model and the eigenmode model of FMR line width with Permalloy films: one made inhomogeneous by NiO and a control sample.

The development of this new model of FMR in inhomogeneous films is important in several respects.

- It gives a clear physical picture of the magnetization dynamics in inhomogeneous thin films.
- It clarifies that the linewidth due to inhomogeneities does not constitute a different kind of damping.
- It provides the theoretical basis for interpreting FMR linewidth that will allow us to study the intrinsic damping processes and, ultimately, to deliver the necessary data to industry.

For More Information on this Topic

For further information on magnetization dynamics, damping and ferromagnetic resonance, please contact R.D. McMichael.

Andrew Kunz and R.D. McMichael, “Normal Mode Mixing and Ferromagnetic Resonance Linewidth.” *IEEE Trans. MAG*, (in press).

Ballistic Magnetoresistance: A New Phenomenon with Great Potential for Magnetic Sensors

Magnetic sensors play a central role in many important technologies ranging from data storage to health care to homeland security. A common need among these technologies is higher sensitivity and smaller size. One possible route to higher sensitivity and smaller size is the introduction of the Ballistic Magnetoresistance (BMR) effect as a method of sensing magnetic fields. Although BMR is, at present, a poorly understood and poorly characterized effect, it has shown very large magnetoresistance values in nanoscale devices and could potentially lead to dramatic improvements in magnetic sensors. NIST has initiated a program aimed at clarifying, controlling, and utilizing BMR for advanced magnetic sensor applications.

Magnetic sensors play a central role in many important technologies. To name just a few, computer hard disk drives use magnetic sensors to read stored data, magneto-encephalography uses magnetic sensors to image brain wave activity, and bio-hazard detectors use magnetic sensors to detect magnetic beads that are bio-tagged for biological agents such as anthrax, botulism, and cholera.



Figure 1: Computer hard disk drives use a magnetic sensor to read data.

A common need among these technologies is sensors with higher sensitivity and smaller size. With higher sensitivity and smaller size, more data could be stored on a hard disk, higher resolution imaging of brain activity would be possible, and earlier warnings of bio-contamination could be given.

The recent discovery of the Ballistic Magnetoresistance effect (BMR) holds the promise of both greatly increased sensitivity and greatly reduced size for magnetic sensors. Figure 3 illustrates how a typical sample is fabricated.

Magneto-encephalography: Imaging Brain Activity

An array of 37 magnetic sensors:

An image of epileptic activity:

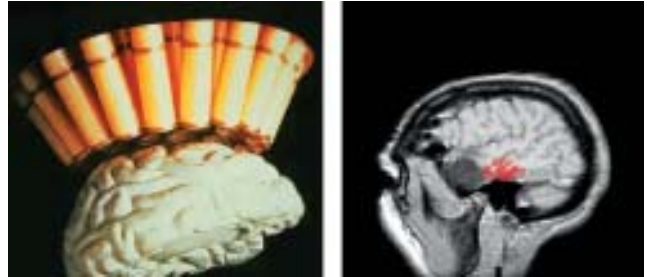


Figure 2: Magnetic sensors are the only technology available for real-time imaging of brain activity. Current sensors are bulky and provide low resolution. Advanced sensors could provide much higher resolution and provide improved surgical guidance.

A sharp Ni wire is placed about 20 μm from a flat Ni substrate. In an electrochemical cell, an electrodeposition potential is applied between the wire and substrate. A fine column of Ni grows out from the wire until it meets the substrate. When electrical contact is made between the column and the substrate the electrodeposition potential drops immediately to zero and the electrodeposition stops. At the point of contact with the substrate, the column has a diameter of ~ 10 nm. When the wire and substrate are magnetized in parallel, electrical current easily flows through the nanocontact. However, when the magnetization is antiparallel, as illustrated in Figure 3, electrons tend to be reflected at the nanocontact because they have the wrong spin to pass easily through this region, and a sharp increase in electrical resistance is observed. This effect is known as magnetoresistance, and values as large as 700% have been observed in this type of magnetic nanocontact.

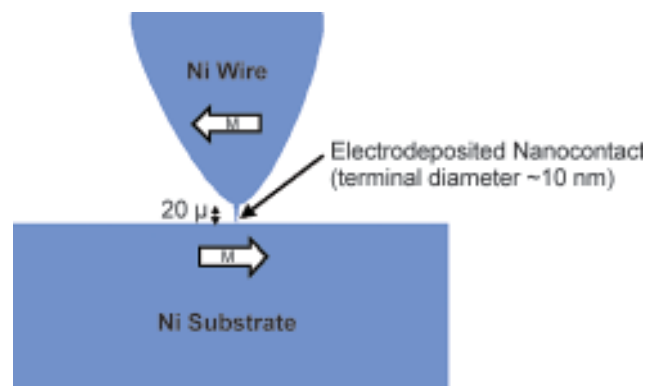


Figure 3: An illustration of magnetic nanocontacts formed by electrodeposition that exhibit very large values of magnetoresistance (N. Garcia, et. al., 2001).

To put this result in context, the sensors that read data from hard disk drives currently have a magnetoresistance of only about 15%, almost 50 times smaller. Moreover, the size of the nanocontact in BMR samples is ~50 times smaller than the hard disk drive sensors. Thus, the BMR effect holds the potential for magnetic sensors of greatly increased sensitivity and greatly reduced size.

The term “ballistic” means that the nanocontact is too small for electrons to flip their spin in transit, as they would in a macroscopic Ni sample.

Unfortunately, it often takes many years to go from laboratory demonstration of a concept to a commercially successful device. While BMR looks promising, it is certainly at an early stage of development. The samples investigated so far have poor reproducibility, poor stability, and poor reliability. The techniques of fabrication are poorly understood, and there is no theory that can explain the magnitude of the BMR effect.

Fortunately, there is the precedent of the Giant Magnetoresistance (GMR) effect to serve as a model. When GMR was discovered in 1989, it was subject to very similar shortcomings. Many experts thought it would never be a commercially successful technology. However, the technical community, assisted by a strong effort at NIST, began to address the issues, and gradually the problems were solved. The result is that, today, every hard disk drive produced in the world uses GMR technology in the read head.

Clearly, the sample geometry illustrated in Figure 3 is not suitable for fabrication of hard disk read heads. The industry’s manufacturing practices require lithographic processing on wafers, and a fundamentally different approach would be prohibitively expensive. In light of this need, initial work at NIST has focused on techniques for achieving BMR in planar geometries on wafers. Our first attempt is illustrated in Figure 4. Although the geometry looks ideal, the BMR achieved so far is only 14%. We believe the problem lies in the method of pinhole formation. Consequently, we are exploring novel approaches to controlling pinhole size, such as the use of the Coulomb explosion that occurs when a highly charged ion like Xe⁴⁴⁺ contacts a surface. By varying

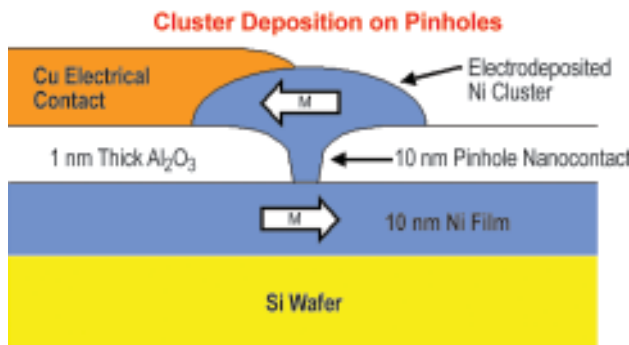


Figure 4: A planer geometry for BMR. Pinholes are created by dielectric breakdown at thin spots in an Al₂O₃ film when the electrodeposition potential is applied.

the charge on the ion, the size of the pinhole can be finely tuned.

A different and much more successful planar geometry on a wafer is illustrated in Figure 5. In this work, a Ni film ~10 nm thick is deposited on an insulating wafer and patterned into the form of a nano or micro gap. Electrodeposition is used to bridge the gap with a Ni nanocontact. In such samples, we have been able to achieve a much higher BMR value of 350%. However, problems with reproducibility, stability, and reliability remain. We are investigating these shortcomings with scanning electron microscopy (SEM) with polarization analysis, transmission electron microscopy (TEM), Lorentz microscopy, and scanning tunneling microscopy (STEM). The field of BMR is so new that very little microscopy has been carried out to date.

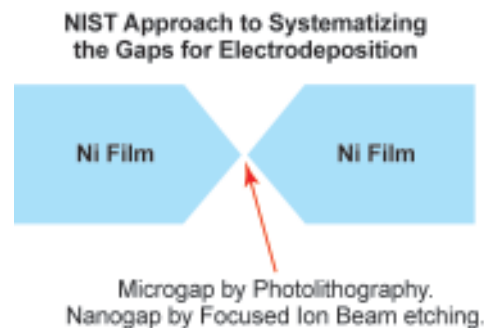


Figure 5: An illustration of Ni films with lithographically patterned gaps for electrodeposition of magnetic nanocontacts on wafers.

We believe that with these studies, it is likely that the shortcomings of BMR materials can be addressed, and BMR technology can move towards a new generation of ultrasensitive nanoscale magnetic sensors that will have wide-ranging impact on many important technologies.

“The technical challenges facing the data storage industry in the next 10 years are so broad and so deep that the industry cannot do it alone. We need researchers like you here at NIST to help us.”

Dr. Sining Mao
 Director, Read-Head Research
 Seagate Technology
 June 14, 2002

For More Information on this Topic

Contact: W.F. Egelhoff, Jr.

M. Muñoz, G.G. Qian, N. Karar, H. Cheng, I.G. Saveliev, N. García, T.P. Moffat, P.J. Chen, L. Gan, and W.F. Egelhoff, “Ballistic Magnetoresistance in a Nanocontact between a Ni Cluster and a Magnetic Thin Film.” *Appl. Phys. Lett.*, 79, p. 2946, (2001).

High-Speed Contact at the Head-Disk Interface in a Magnetic Hard Disk Drive: Experiment and Modeling

As magnetic data storage technology moves towards higher areal density with lower flying heights and higher rotational speeds, the propensity of random contacts at the head-disk interface is bound to increase. The tribological performance of the head-disk interface will have significant impact on the performance and durability of the hard disk drive. A high-speed impact test method has been developed for evaluating nanometer-thick lubricant film/carbon overcoat materials on hard-disk surfaces, and a three-dimensional finite element model has been constructed to calculate the stress concentrations and the effect of material parameters on the resulting deformation. The availability of an experimental technique and a model enables effective screening of different material chemistries and lubricant combinations to improve the level of protection for hard disk technology.

Development of newer generations of hard disk drives with higher data storage capacity poses many technological challenges. The magnetic disk drive consists of a multilayer disk that stores the data and an air-bearing slider that contains a magnetic head for reading and writing. As the areal density of data storage increases towards 155 Gb/cm², the physical spacing between the head and disk surfaces needs to be reduced from (10 to 15) nm to 3.5 nm. The rotational speed needs to increase to 15,000 rpm (45 m/s) from 7200 rpm. The combination of the low flight height and high speed makes occasional contacts inevitable due to disk waviness, spindle wobble, and disk surface roughness. Sometimes catastrophic collisions (avalanche) result in the loss of data.

Besides improving the spindle and surface roughness, new overcoats and lubricants are being investigated to improve the protection of the disk against such high-speed collisions. Actual durability field trials to evaluate new materials under such conditions are time-consuming and expensive as well as statistics-based. Thus, there is an urgent need to develop an accelerated test methodology to evaluate materials under controlled conditions.

The experimental research includes development of a one-pass, high-speed impact test instrumentation and test method to evaluate materials on a hard disk surface. The basic concept is to artificially create a ridge (500 to 2000) nm high with a 0.002° to 0.01° angle of incline on the disk surface by controlled scratching at the substrate side of the disk to create a ridge on the top surface with its multilayers intact. A 3 mm diameter ruby ball collides with the ridge under 7200 rpm rotational

speed. The impact force is measured with an acoustic emission (AE) sensor and the deformation volume is obtained with an atomic force microscope (AFM).

For the experiments reported here, the height of the ridge is 2000 nm and the angle of incline is 0.003°. There is considerable difficulty in alignment, z-height control, and force calibration. Figure 1 shows a typical electrical signal from the AE sensor during an impact. The intensity of the signal is converted to force which is about one newton or less. The calibration of the AE signal is carried out using both the ball-drop method and pencil-lead break method. A modified ball drop method was developed to improve the accuracy of the calibration. Figure 2 shows the setup: one ball drops onto another ball to create the signal. The bottom ball is pressed into the disk and the area of contact is measured with an optical microscope.

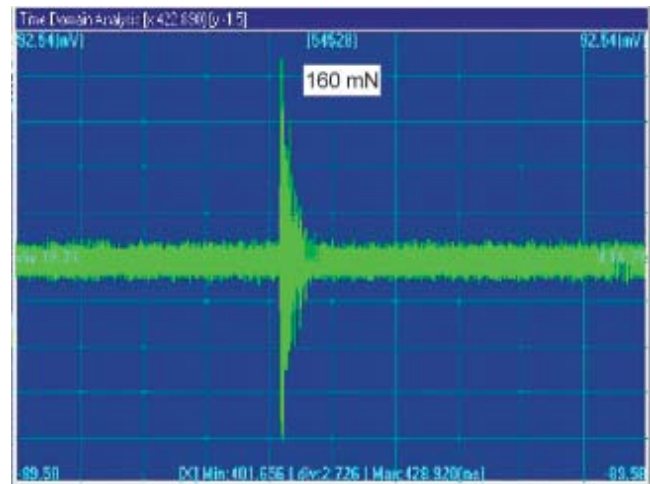


Figure 1: Acoustic emission signal from an impact event.

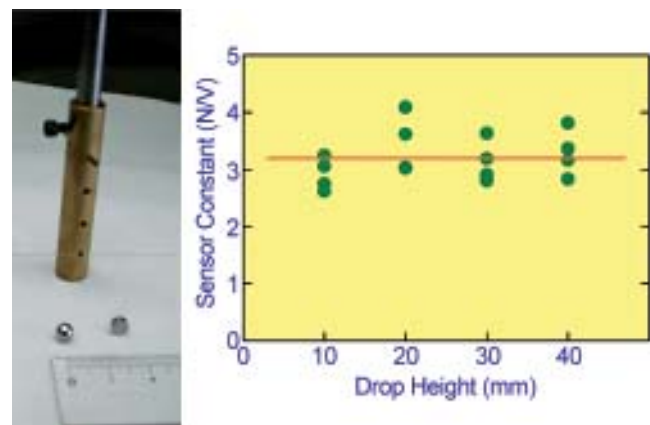


Figure 2: Ball-dropping apparatus (left) and data (right) for the force calibration.

By dropping one ball on top of a second ball positioned at the pre-formed deformation zone, the signal transmits through the known contact area between the ball and the disk. The acoustic signal from the collision is recorded with the sensor placed on the other side of the disk. The resulting calibration curve indicates a sensor constant of (3.2 ± 0.4) N/V under these experimental conditions.

A series of impact tests was conducted on disk samples with different monolayer (1 nm) coatings. The transmitted force measured for a blank disk is (0.92 ± 0.23) N. For perfluoro-polyether (PFPE), the transmitted force is (0.61 ± 0.04) N and for PFPE + 5% phosphazine, the transmitted force is (0.31 ± 0.07) N. This ranking corresponds with industrial field experience in terms of robustness of lubricant coatings.

The computational component of this research investigates the dynamic problem of a high-speed spherical asperity impacting on a flat surface of a hard disk at a shallow angle. The objective is to ascertain the result of such an impact and to investigate the complex interactions of multilayer materials such as a hard disk. We seek to obtain the values of contact duration, contact zone size, time history solutions of stress field (including residual stress), damage/plastic yield zone, contact area, and contact force for a given set of attributes including the layered structure of the disk. Due to the time-dependent nature and the difficulty of the problem (such as the geometric complexity, the materials' nonlinear, nonuniform and path-dependent properties, and inertial effects), analytical closed form solutions are not possible. A numerical method using finite element simulation was used. It should be emphasized that this approach is continuum in nature as implied by the conventional finite element theory. However, as the thicknesses of the layers are reduced to a few nanometers, the effect of surface mechanical stresses present at the free surface and interfaces becomes significant and, thus, cannot be ignored.

Using the guidelines described above, we constructed a 3D finite element model. The model includes only the top half of the disk due to the shallowness of the impact. The slider is modeled by a two-mass system linked by a spring simulating a nanoasperity on the head surface.

For a given layered structure and geometry, asperity size, and impact velocity, the model is capable of predicting sliding contact events, including contact duration, zone size, forces, penetration depth, underlying plastic zone, and energy transfer. The simulations use realistic values from current disk design: asperity size = 30 nm in radius, impact speed = 10 m/s, and (5, 30 and 50) nm thicknesses for the overcoat, media layer and substrate, respectively. The results are given below.

Figure 3 is a contour plot of the maximum principle stress field created by two collisions. Each collision occurs on a time scale of approximately 10 ns. The *in-situ* stress field under the asperity demonstrates compression ahead and tension behind the penetration.

The plastic deformation zone created in the substrate as a result of two collisions between the asperity and substrate is shown in Figure 4. When the asperity has left the disk surface after a collision, there exists a well-defined zone of residual stress, indicating that elastic recovery causes stress redistribution. The stress field distribution is influenced by the different mechanical properties of the individual layers as noted in Figure 3.

The simulation also gives an indication of the energy partition as a result of collision under an adiabatic assumption. Results suggest that under a short duration, relatively light normal load, the momentum transfer due to velocity change results in a substantial temperature rise at the interface. The energy attributable to frictional dissipation is about 40 fJ per impact for a given friction coefficient of 0.3. The energy from plastic deformation is only about 7 fJ when a portion of the kinetic energy from the moving slide is transferred onto the disk. It is clear that the dominant mechanism of energy consumption is due to heat generated from friction, an outcome consistent with experimental observations.

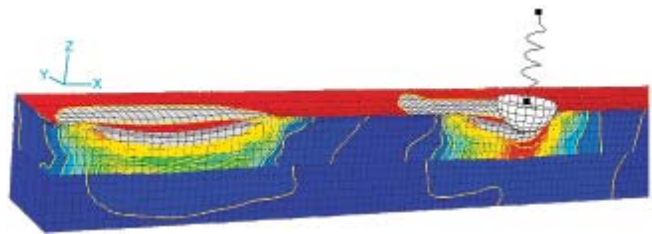


Figure 3: Contour plot of the maximum principle stress field created from two collisions between an asperity (represented by a semi sphere in the figure) and substrate.

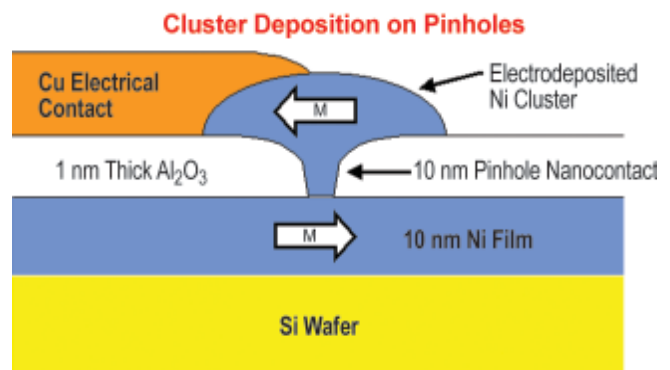


Figure 4: Plastic zones developed underneath the collision sites. Also shown are the deformed craters on the top surface.

For More Information on this Topic

Contact: M. Bai, T.J. Chuang, S.M. Hsu, Z.C. Ying

“Simulation of a Single Asperity Impact at Head-Disk Interface,” Chuang, T.-J., and Hsu, S.M., ASME/STLE Proceedings on the Frontiers of Magnetic Hard Disk Drive Tribology and Technology, Cancun, Mexico; also submitted to ASME *Trans. Journal of Tribology*.

Projects in Materials for Micro- and Optoelectronics

Characterization of Porous Low-k Dielectric Constant Thin Films

NIST is working to provide the semiconductor industry with unique on-wafer measurements of the physical and structural properties of porous thin films important to their use as low-k dielectric materials. The methodology utilizing several complementary experimental techniques to measure the average pore and matrix morphology has been expanded to include pore size distributions. New methods have been developed to measure closed pore content and matrix morphology in films having complex structures with any morphological type.

Barry J. Bauer and Wen-li Wu

The next generation of integrated circuits will require feature sizes that demand new low-k interlayer dielectric materials. To address problems with power consumption, signal propagation delays, and crosstalk between interconnects, dielectric constants will have to reach unprecedented values. One avenue to low-k dielectric materials is the introduction of nanometer scale pores into a solid film to lower its effective dielectric constant. While these modifications change the dielectric constant favorably, other important parameters such as physical strength and barrier properties will also change, often in an unfavorable way. Characterization of the pore structure is crucial to rapid development of new dielectric materials, and new measurement methods are necessary.

The small sample volume of 1 μm films and the need to characterize the films on silicon wafers narrows the number of available measurement methods. We have been providing standard characterization using a combination of small angle neutron scattering (SANS), high-resolution x-ray reflectivity (HRXR), and ion scattering techniques. These measurements are performed directly on films supported on silicon substrates so that processing effects can be investigated. New methods are required, however, to provide more detailed information necessary to complete the product development.

During the past year, we have continued our efforts on characterization of current industrially-relevant materials through International SEMATECH, and by new collaborations with Dow Chemical and IBM. More significantly, we have perfected new techniques for more thorough and accurate film characterization.

International SEMATECH, a consortium of microelectronics companies, provided more than 20 separate samples for characterization by NIST. The structural information provided by NIST is placed into a master database that includes data from a variety of sources, detailing both the structural and material properties needed to evaluate candidate materials. Member companies make extensive use of the data to

guide the development of low-k dielectric materials for integration into future devices.

Finally, we have evaluated and perfected new measurement methods to more thoroughly and accurately characterize pore and matrix morphology. Capillary porosimetry has been applied to HRXR measurements to determine pore size distributions, rather than simple averages. By the use of a carrier gas and control of vapor pressure through thermal methods, the accuracy and speed of the measurements have greatly improved. Based on these findings, an automated measurement system has been designed and is under construction with the ultimate goal of providing a measurement technique that can be transferred to the materials suppliers and chip manufacturers.

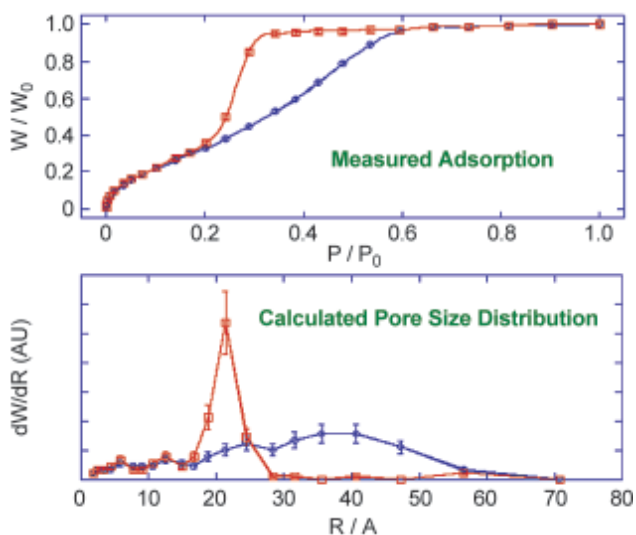


Figure 1: Representative mass gain and pore size distribution calculated from HRXR porosimetry measurements (AU = arbitrary units).

New techniques have been developed that measure SANS from films that have been infused by mixtures of normal toluene and toluene in which hydrogens have been replaced by deuterium. The match point measures where the neutron contrast matches that of the wall material. By filling the open pores with contrast match fluids, SANS reveals the closed pore content and size. The relative open and closed pore content is becoming increasingly important to low-k applications.

Contributors and Collaborators

B.J. Bauer, H.J. Lee, R.C. Hedden, C.L. Soles, H. Wang, D. Liu, W.L. Wu (Polymers Division, NIST); C. Glinka (NIST Center for Neutron Research); J. Wetzel, J. Lee (International SEMATECH); B. Landes (Dow Chemical); M. Baklanov (IMEC); D. Gidley (University of Michigan); W. Chen, E. Moyer (Dow Corning); S. Yang (Lucent)

Dielectric Metrology for Polymer Composite Films in the Microwave Range

Novel dielectric hybrid materials based on organic resins and ferroelectric ceramics with high dielectric constants have been identified by the industry as key dielectrics for advancing miniaturization and functional performance of microwave electronics. The objective of this project is the development of broadband dielectric metrology for such materials and fundamental understanding of the high frequency relaxation mechanism in relation to structural and molecular attributes.

Jan Obrzut

We have developed an accurate broadband measurement technique that enables dielectric measurements at microwave frequencies of up to several GHz. The broadband test methods currently in use by the industry are based upon a lumped element approximation and are limited to frequencies below a few hundred megahertz. Our new technique is based on the observation and theoretical analysis of fundamental mode propagation at high frequencies in thin film dielectrics terminating a coaxial air-filled transmission line. The 3D vector plot of the electric field of the first fundamental mode, simulated inside a high-k specimen, is shown in Figure 1.

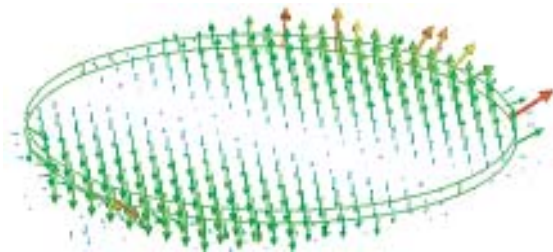


Figure 1: The vector plot of the electric field, E , of the first fundamental mode inside the film specimen ($\epsilon^* = 34.6 - j1.6$) terminating an AP-7 coaxial line. The arrows indicate the direction and strength of the electric field E .

In contrast to the assumption of the lumped element model, the field in the specimen section is not uniform. At a resonant frequency of about 8.2 GHz, the magnitude of the electric field, E , shows two maxima localized near the edge of the specimen, while the minimum magnitude of field E extends along the specimen diameter. The corresponding plot of the magnetic field, H , is parallel to the propagation direction. Both E and H fields appear to decay rapidly at the boundary between the high-k dielectric and air. The results of numerical simulations confirm our earlier experimental analysis that, at microwave frequencies, the film specimen becomes a transmission line with propagation direction along the film diameter rather than its thickness.

The new broadband methodology enables measurements at frequencies of 100 MHz to 10 GHz with the precision required by new electronic technologies. In partnership with the Institute for Interconnecting and Packaging Electronic Circuits, IPC, we initiated a standard test method development and chair the IPC-D37-d test method subcommittee for Embedded Passive Devices. We guided the design of the test protocol and made arrangements with co-sponsoring member companies for round robin evaluation.

Our capability to measure the dielectric relaxation times in the sub-nanosecond regime and the relaxation strength for wide range of dielectric permittivity values is used to quantify dispersion, alignment, and structure in hybrid materials. Using the broadband study, we demonstrated that the composites of organic polymer resins filled with ferroelectric ceramics exhibit a dominant intrinsic high-frequency relaxation behavior. Such dielectric properties were beneficial in eliminating the electromagnetic noise in processors and logic devices. We have confirmed that the fastest dielectric relaxation process is controlled by the dipolar dynamics of the polymer matrix while the dielectric loss arises from the difference in coupling between the relaxed and unrelaxed dipoles. Our new numerical models can quantitatively correlate the dependence of the real and imaginary parts of the complex permittivity on the volume fraction of the ceramic filler.

We have developed constrained regularization algorithms to obtain a continuous distribution function of relaxation times. The method is able to resolve multiple relaxation processes without any *a priori* assumptions about their character. It may be generalized to different types of fundamental relaxation processes and not restricted to a superposition of Debye-like functions. This approach will help judge the identity between microscopic and macroscopic relaxation behavior of polymer composite systems. It also allows us to link broadband dielectric spectroscopy with other techniques such as time domain spectroscopy, photon correlation spectroscopy and NMR.

Contributors and Collaborators

O. Anopchenko, N. Noda and J. Obrzut (Polymers Division); B. Rust (Mathematical and Computational Sciences Division); R. Croswell (Motorola); R. Charbonneau (Storage Tech.); D. McGregor (DuPont); T. Hubbing (University of Missouri); R. Greenlee (Merix); J. Murry (Litton); Tom Newton (IPC); R. Foly (DOD); J. Peiffer (3M); L. Patch (NCMS); D. Senk (Shipley); R. Sheffield (Nortel)

Polymer Photoresists for Next-Generation Lithography

Photolithography, the process used to fabricate integrated circuits, is the key enabler and driver for the microelectronics industry. As lithographic feature sizes decrease to the sub-100 nm length scale, significant challenges arise because both the image resolution and the thickness of the imaging layer approach the macromolecular dimensions characteristic of the polymers used in the photoresist film. Unique high-spatial resolution measurements are developed to reveal limits on materials and processes that challenge the development of photoresists for next-generation sub-100 nm lithography.

Eric K. Lin

Photolithography is the driving technology used by the microelectronics industry to fabricate integrated circuits with ever decreasing sizes. In this process, a designed pattern is transferred to the silicon substrate by altering the solubility of areas of a polymeric photoresist thin film through an acid catalyzed deprotection reaction after exposure to radiation through a mask. To fabricate smaller features, next-generation photolithography will be processed with wavelengths of light requiring photoresist films less than 100 nm thick and dimensional control to within 2 nm. Material and transport issues arise when fabricating structures over these length scales. To date, the materials and processes needed to fabricate sub-100 nm features have not been selected.

To advance this key fabrication technology, we work closely with industrial collaborators to develop and apply high-spatial resolution and chemically specific measurements to understand changes in material properties, interfacial behavior, and process kinetics at nanometer scales and to provide high-quality data needed in advanced modeling programs.

Over the past year, we have applied and enhanced unique measurement methods and computer simulation tools to provide new insight and detail into the complex physico-chemical processes used in advanced chemically-amplified photoresists. These methods include x-ray and neutron reflectivity (XR, NR), small angle neutron and x-ray scattering (SANS, SAXS), incoherent elastic neutron scattering (IENS), near-edge x-ray absorption fine structure (NEXAFS), combinatorial methods, x-ray standing waves with fluorescence (XSW), nuclear magnetic resonance (NMR), molecular dynamics (MD) simulations, and atomic force microscopy (AFM). In particular, XR and NR studies with specially designed model materials were used to profile the reaction front with nanometer resolution (see Highlights), NEXAFS measurements have been extended to depth profile the chemical composition of the top 5 nm of a polymer film surface, SAXS measurements have been performed in transmission on patterned structures to complement

earlier SANS studies, and AFM techniques have been adapted to begin study of the mechanical properties of interfacial polymer layers and structures.

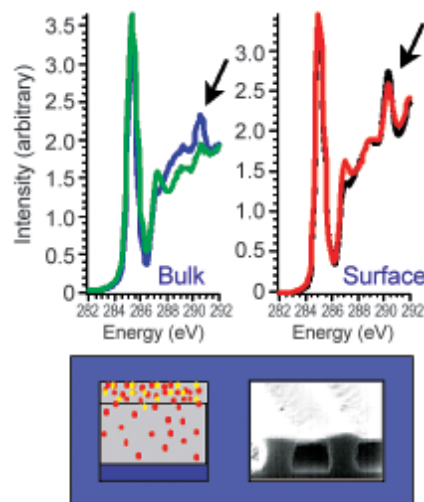


Figure 1: NEXAFS carbon-edge spectra from the bulk and surface of a model photoresist before (blue/black) and after exposure and bake (green/red). A delay time of 5 min was imposed after exposure and before a bake. The reaction is incomplete only at the surface (peak signature at arrows) corresponding to surface base (yellow) contamination as illustrated.

Our experimental and theoretical methods have been used to understand important technical problems in the development of next-generation materials. These topics include: the spatial evolution of the reaction-diffusion process as a function of temperature and time; the domain size and distribution of photoacid generator molecules within a model photoresist polymer matrix; the microscopic dynamics of photoresist polymers in thin films; the segregation and distribution of small molecule contaminants, solvents, and moisture in ultrathin polymer layers; investigation of the anti-reflective coating-photoresist interface for material sources of compromised line-profile control; development contributions to the measured line-edge roughness; and the structural characterization of critical dimensions and line-edge roughness in lithographically-fabricated patterned structures.

Contributors and Collaborators

E.K. Lin, C.L. Soles, J.L. Lenhart, R.L. Jones, V.M. Prabhu, F.W. Starr, J.F. Douglas, P.M. McGuigan, D.L. VanderHart, W.L. Wu (Polymers Division); D.A. Fischer, S. Sambasivan, J. Woicik (Ceramics Division); S.K. Satija, C.J. Glinka (NCNR); D.L. Goldfarb, M. Angelopoulos (IBM T.J. Watson Research Center); B.M. Trinqué, S.D. Burns, C.G. Willson (University of Texas); R. Puligadda, Y. Wang, D. Guerrero (Brewer Science)

Superconformal Film Growth: Measurements and Modeling

State of the art manufacturing of microelectronic devices relies on superconformal deposition of copper for on-chip interconnects. Superfilling of trenches and vias results from the interplay of rate inhibiting and accelerating adsorbates. NIST has recently identified the mechanism that explains “bottom-up” filling of submicrometer features. A quantitative capability for predicting the influence of adsorbates on superconformal film growth has been demonstrated. The mechanism has also been shown to apply to the electrodeposition of elements beyond copper, as well as CVD processing.

Thomas P. Moffat and Daniel Josell

The mechanism of superfilling or “bottom-up” filling of submicrometer features has been explained. The chief tenets are: a) the deposition rate is proportional to catalyst coverage and b) the catalysts “floats” or remains segregated at the interface during film growth. Superfilling follows as a natural consequence of these stipulations. Namely, the catalysts coverage increases (decreases) as the local surface area decreases during deposition, thereby giving rise to “bottom-up” filling and a bright surface finish.

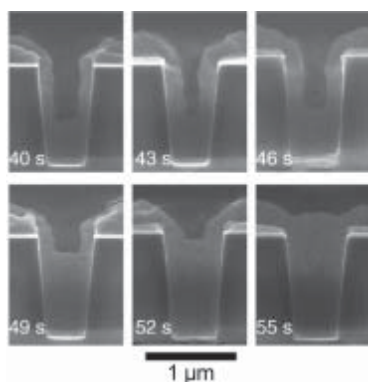


Figure 1: “Bottom-up” filling of vias with silver.

Quantitative description of the curvature enhanced accelerator coverage (CEAC) mechanism enables the simulation of feature filling. Three different electrode shape-change algorithms have been developed: 1) a simple model based on the solution of a single first-order differential equation, 2) a parameterized interface tracking code, and 3) a level set model, which incorporates a rigorous description of all concentration fields. Good agreement was found between these formalisms and feature filling experiments. A summary of the “simple model” simulations for filling trenches of variable aspect ratio as a function of applied potential and catalyst concentration is shown in Figure 2.

The generality of the CEAC mechanism has been verified by demonstrating superfilling of metals other than copper, i.e. silver electrodeposition from an alkaline

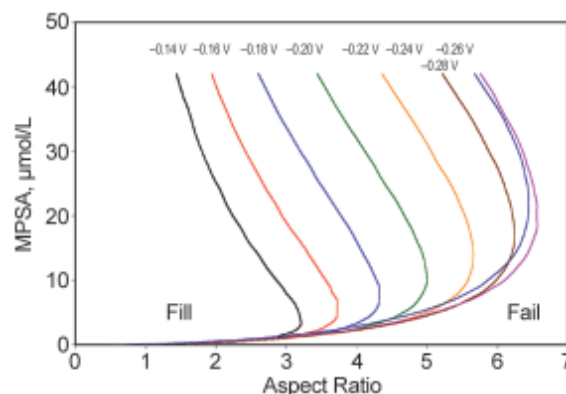


Figure 2: Feature fill/fail boundaries as a function of processing parameters: catalyst concentration, etc.

electrolyte, as well as the first quantitative predictions of superfilling by iodine catalyzed chemical vapor deposition (CVD).

All kinetic parameters were determined from voltammetric (i-V) and chronoamperometric (i-t) experiments performed on planar substrate. Correlation between the reactivity and catalyst coverage was determined by surface analysis following metal deposition or, alternatively, by dosing the surface with a prescribed quantity of catalyst prior to the metal deposition experiment. The second scheme not only substantiates the CEAC mechanism but may also be implemented in manufacturing in order to circumvent the challenging control issues associated with catalyst consumption during electrolyte aging.

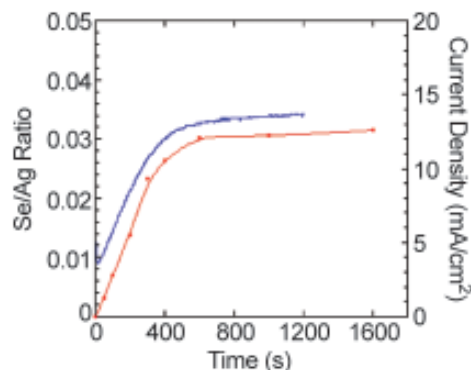


Figure 3: A one-to-one correlation between catalyst coverage (red) and the deposition rate (blue).

Contributors and Collaborators

D. Wheeler, J. Bonevich, W. Egelhoff (MSEL); G. McFadden (ITL); S. Coriell, B. Baker, C. Yang, L. Richter, S. Robertson (CSTL); J. Mallett, C. Witt (International SeMaTech); B. Melnick, M. Freeman (Motorola); S.G. Pyo (Hynix Semiconductor)

Micrometer-Scale Reliability: Stress Voiding and Electromigration

The microelectronics industry continues to strive for better device performance through a combination of dimensional scaling and incorporation of new materials for chip-level interconnects. Reliability of the resulting new systems is poorly known at present. We conduct studies to understand the mechanisms of thermal strain — and electric current — induced degradation phenomena, with emphases on the roles of localized stress and localized variations in microstructure on interconnect lifetimes.

Robert R. Keller and Roy H. Geiss

Technical Description

The two primary reliability-limiting phenomena that chip-level interconnects undergo are stress voiding (SV) and electromigration (EM), occurring during thermal- and electric current-induced stressing, respectively. Both involve the development and subsequent relaxation of stress and take the form of surface topography development and void formation. Consequent device failure occurs in the form of passivation cracking, short circuiting, and open circuiting. Previous studies have demonstrated that even small variations in localized microstructure can have large impacts on these types of failure.

We began an effort about a year and a half ago that shows that both mechanical and diffusion-based degradation processes can occur due to alternating current (AC) stressing at low frequencies and high current densities. Interconnect damage under such conditions appears to occur due to thermomechanical fatigue resulting from Joule heating of metal interconnects well-adhered to oxidized silicon substrates. Thermal expansion mismatch strains lead to large stresses in the metal and cause cyclic deformation. This work has suggested both a new testing technique as well as a potentially new reliability threat to narrow interconnects. AC stressing can be used to perform fatigue testing of very small structures in this manner. The reliability threat appears as we consider such testing in metals encapsulated by soft dielectrics, which may not suppress the surface damage. Here, we report new observations of microstructural changes accompanying AC stressing of Al-alloy interconnect lines.

Accomplishments

We conducted a quasi *in situ* test whereby a line was characterized for surface structure and crystallographic orientation distribution prior to testing, as well as during periodic (every 15–60 s) test interruptions. Figure 1

shows a SEM image and the corresponding orientation map obtained by automated electron backscatter diffraction (EBSD) after less than one minute of stressing. The topography in the large grain towards the left of the field of view can be explained by the schematic to the far left. Given the observed orientation, threading dislocations could glide on the indicated slip system leaving slip offsets at the surface. During cycling, the severity of the offsets increases considerably.

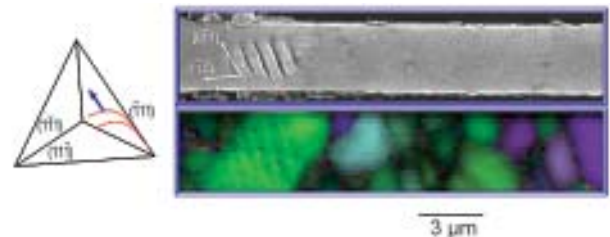


Figure 1: Dislocation mechanism for topography formation induced by AC stressing in Al-1Si.

An unexpected observation is shown in Figure 2, where the orientation maps show that significant grain growth can occur even within the first minute of stressing, prior to the formation of slip offsets. This demonstrates that the effect induced by low-frequency cycling of high-current density is not simply mechanical fatigue, but that diffusion must also play a significant role. Interestingly, we have seen this effect only in the aluminum alloy. Similar ongoing studies on copper done by our colleagues at the Max-Planck-Institut have shown no evidence of grain growth in the absence of topography development. Rather, that work shows grain growth that takes place concurrently with or after the formation of slip offsets.

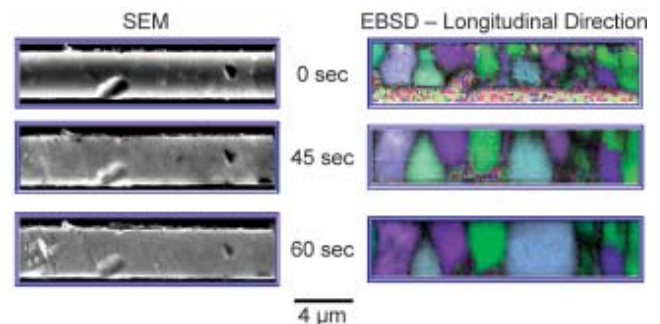


Figure 2: Grain growth induced within first minute of AC stressing, prior to occurrence of topography.

Contributors and Collaborators

R. Mönig, C. Volkert (Max-Planck-Institut für Metallforschung)

Phase Equilibria and Properties of Dielectric Ceramics

Ceramic compounds with exploitable dielectric properties are widely used in technical applications such as actuators, transducers, and resonators or filters for wireless communications. The commercial competitiveness of next-generation devices depends on new ceramics with improved properties and/or reduced processing costs. Experimental phase equilibria determination, integrated with systematic chemistry-structure-property studies (experimental, theoretical, and modeling) contribute toward the fundamental understanding and rational design of these technologically important materials.

**Terrell A. Vanderah, Benjamin P. Burton,
Eric J. Cockayne, and Igor Levin**

Ternary oxides in the $\text{Bi}_2\text{O}_3\text{-ZnO-Nb}_2\text{O}_5$ system exhibit high-dielectric constants (ϵ), relatively low dielectric losses, and compositionally tunable temperature coefficients of capacitance (τ_c). Such properties combined with sintering temperatures of less than 950°C render these materials attractive candidates for capacitor and high-frequency filter applications in multilayer structures co-fired with silver electrodes. The system features two structurally distinct ternary compounds, $\text{Bi}_{1.5}\text{Zn}_{0.92}\text{Nb}_{1.5}\text{O}_{6.92}$ ($\epsilon = 145$, $\tau_c = -400 \text{ MK}^{-1}$) and $\text{Bi}_2\text{Zn}_{2/3}\text{Nb}_{4/3}\text{O}_7$ ($\epsilon = 80$, $\tau_c = +200 \text{ MK}^{-1}$), which exhibit very dissimilar dielectric properties and form temperature-stable, commercially important mixtures. However, the absence of structural information for both phases has precluded understanding of the unusual dielectric properties; in particular, $\text{Bi}_{1.5}\text{Zn}_{0.92}\text{Nb}_{1.5}\text{O}_{6.92}$ ceramics exhibit dielectric relaxation, attributed to a dipolar glass-like mechanism, while no such behavior is observed for $\text{Bi}_2\text{Zn}_{2/3}\text{Nb}_{4/3}\text{O}_7$. Recent studies combined electron, x-ray, and neutron powder diffraction techniques to elucidate the crystal structures of these compounds which feature pyrochlore and zirconolite-like structures, respectively. The results reveal that displacive disorder in $\text{Bi}_{1.5}\text{Zn}_{0.92}\text{Nb}_{1.5}\text{O}_{6.92}$ is responsible for the high dielectric constant and the relaxation phenomenon.

Subsolidus phase relations have been determined for the $\text{BaO}:\text{TiO}_2:\text{Ta}_2\text{O}_5$ system and the $\text{BaO}:\text{Ta}_2\text{O}_5$ subsystem, which are pertinent to the processing of Ta_2O_5 -based ceramics for cellular base station resonators and filters. BaTiO_3 dissolves a considerable amount of Ta^{5+} by forming Ti^{4+} vacancies. The formation of $\text{Ba}_3\text{Ti}_4\text{Ta}_4\text{O}_{21}$, a member of the hexagonal $\text{A}_3\text{M}_8\text{O}_{21}$ -type ternary oxides, was confirmed as well as its solid solution. Several new compounds have been found, including four members of the orthorhombic “rutile-slab” homologous series, $\text{BaTi}_n\text{Ta}_4\text{O}_{11+2n}$, with n -values 3, 5, 7, 9. Three ternary phases with close-packed $[\text{Ba},\text{O}]$ layer structures related to that of $6L \text{Ba}_4\text{Ti}_3\text{O}_{30}$ were found: $13L \text{Ba}_{18}\text{Ti}_{53}\text{Ta}_2\text{O}_{129}$,

$7L \text{Ba}_{10}\text{Ti}_{27}\text{Ta}_2\text{O}_{69}$, and $8L \text{Ba}_6\text{Ti}_{14}\text{Ta}_2\text{O}_{39}$. The crystal structures of the $13L$ and $7L$ phases were determined by single-crystal x-ray diffraction. Phases with tetragonal tungsten bronze related structures occur over large compositional ranges, both within the ternary and along the $\text{BaO-Ta}_2\text{O}_5$ binary.

$\text{PbZr}_{1-x}\text{Ti}_x\text{O}_3$ (PZT) is an important piezoelectric material that has applications in transducers. A first-principles-based effective Hamiltonian was developed for Zr-rich PZT. This model is the first that reproduces the correct sequence of phase transitions in this system: orthorhombic to rhombohedral to cubic, as the temperature increases.

Other important transducer materials include relaxor ferroelectrics. An effective Hamiltonian was developed for the relaxor ferroelectric $\text{PbSc}_{1/2}\text{Nb}_{1/2}\text{O}_3$ (PSN), based on first-principles calculations. This model allows one to simulate the structure and dielectric properties of PSN as a function of cation ordering, temperature, and applied fields, in systems representing as many as 300,000 atoms. Molecular dynamics methods allow the polarization dynamics and frequency dependence of the dielectric permittivity to be studied. The local electric field at the Pb sites due to the charged Sc and Nb ions has been calculated (see Figure 1) and incorporated into the model. The results establish a clear link between chemical disorder and dielectric response, and they indicate “nanoscale texture,” i.e., the size and geometrical arrangement of domains play a fundamental role in the observed macroscopic properties.

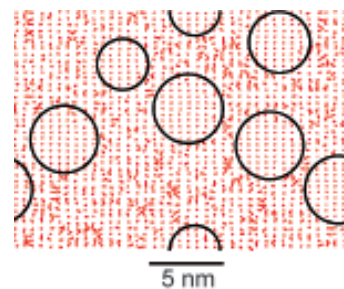


Figure 1: Local electric fields in a model for the relaxor ferroelectric PSN. Experiments suggest that relaxor ferroelectrics contain chemically-ordered regions in a disordered matrix and that such inhomogeneities may be responsible for the relaxor behavior. Computations show that chemically-ordered regions in PSN (circles) have much lower local fields than the disordered matrix.

Contributors and Collaborators

R.S. Roth, W. Wong-Ng (MSEL); J.E. Maslar (CSTL); R. Geyer (EEEL); S. Bell (TRAK Ceramics, Inc.); C.A. Randall (Penn State); J.C. Nino (Penn State); K. Leung (Sandia); L. Bellaiche (University of Arkansas); U. Waghmare (JNCASR, Bangalore, India); S. Prosandeev (Rostov State University, Russia); V. Zelezny and J. Petzelt (Czech Academy of Sciences)

Processing of Low Temperature Co-Fired Ceramics

Low temperature co-fired ceramics (LTCC) are rapidly becoming the technology of choice for RF components and modules for portable wireless applications. LTCC technology has demonstrated that it can enable the high density integrated packages meeting the requirements for portable wireless. Commercialization of these modules requires the accurate prediction of dimensional changes during sintering in order to design passive integrated components (resistors, capacitors and inductors) in the LTCC module.

John E. Blendell and Jay S. Wallace

Low temperature co-fired ceramics (LTCC) are finding increasing use in portable wireless applications due to their high dielectric constant, low loss and high Q. These features allow a reduction in the size of modules for high-frequency applications. In addition, LTCC can include integrated passive components, they are environmentally robust, and they can be rapidly produced. These factors lead to a significant cost advantage for LTCC modules. Because dimensional tolerances are critical for high-frequency applications, accurate predictive models of dimensional changes during sintering are necessary for the commercialization of LTCC modules.

Modeling the evolution of the microstructure, and the dimensional changes that take place during sintering, is being carried out using a combination of phase field methods and object-oriented finite element analysis. This allows accurate modeling of sintering processes with arbitrary boundary conditions. The finite element models are being used to solve for the stress state of the powder compact. These stress profiles will be used in the phase field model to predict mass flow and microstructural evolution during firing. Preliminary two-particle models have been constructed to study the shrinkage in a glass phase. These models will be extended to multiple particle models to allow the interactions that can cause rearrangement of the particles to take place.

An important aspect of this research is the verification of the models developed. We have constructed an optical hot stage microscope for direct examination of the surface of the LTCC tapes during sintering. The movement of markers placed on the surface has shown that there is anisotropic shrinkage, Figure 1. Not all markers move towards a common center, but rather there is local rotation of the markers, indicating local variations in shrinkage.

Optical transmission through the unsintered tapes was measured, Figure 2. The measurements show

density variations on the 100 μm scale, consistent with the sintering results. The transmission measurements are being extended into the near IR region using an IR diode laser to improve the resolution of the density variation data.

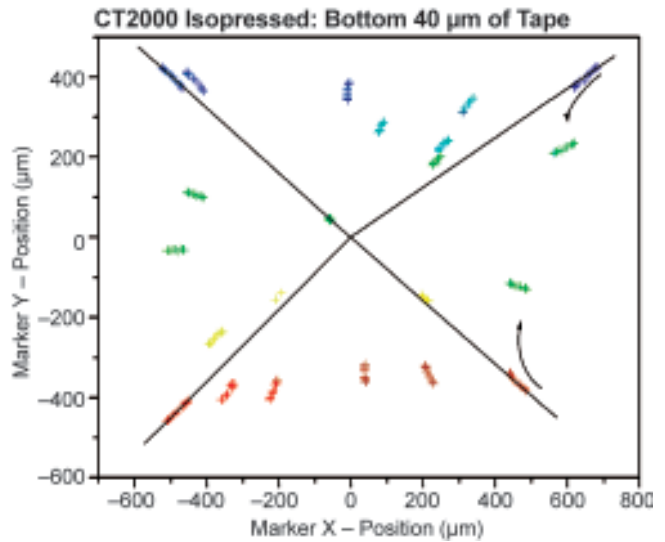


Figure 1: Hot stage optical microscope measurement of surface marker movement showing anisotropic shrinkage.

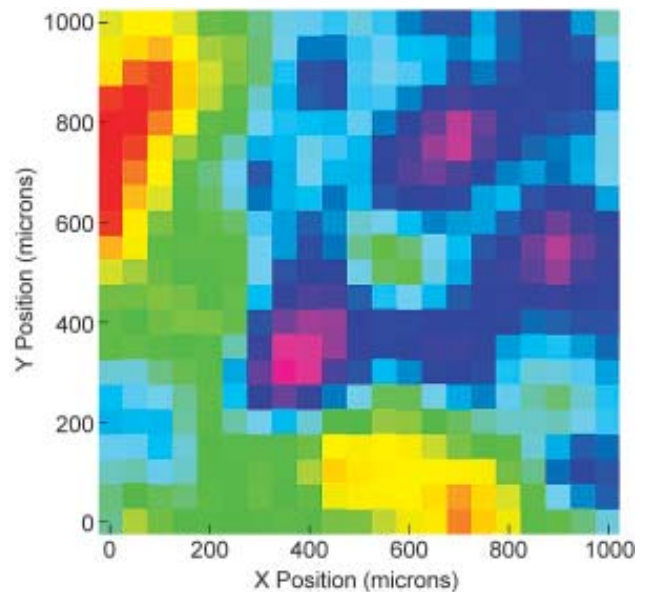


Figure 2: Optical transmission of unsintered tape showing variations due to particle packing variations.

Contributors and Collaborators

P. Schenck, B. Hockey (Ceramics Division); J. Warren (Metallurgy Division); M. Locatelli (University of Washington, Seattle, WA)

Solder and Solderability Measurements for Microelectronics

Solders and solderability are increasingly tenuous links in the assembly of microelectronics as a consequence of ever-shrinking chip and package dimensions and the international movement toward environmentally-friendly, lead-free solders. Through collaboration with the NEMI Pb-Free Assembly Project, we are providing the microelectronics industry with measurement tools, data, and analyses that address national needs in the implementation of lead-free solders. We also work with industrial standards organizations to provide measurement methods and guidance for integration of lead-free solders and new component types into assembly processes.

Maureen E. Williams, William J. Boettinger, Carol A. Handwerker, Ursula R. Kattner, and Frank W. Gayle

The U.S. microelectronics industry has clearly articulated the measurement needs for Pb-free solders and for solderability and assembly. For example, the urgency for materials data for Pb-free solders has been specified in the 1997 IPC, 1999 ITRS, 2000 NEMI, and 2000 IPC Lead-Free Solder Roadmaps. The pressure from the Japanese consumer product market and from the EU to produce lead-free microelectronics continues to increase. In addition, the lack of understanding and control of current standard solderability measurements has inhibited the development of improved measurements necessary for new solders and for new packaging schemes. These industrial needs are addressed through this NIST project.

Since 1999, NIST has served a major role in the NEMI Pb-Free Assembly Project to identify and move Pb-free solders into practice. Last year, NIST held a workshop cosponsored by NEMI, NSF, and TMS, on Modeling and Data Needs for Lead-Free Solders. The report from this workshop is serving as a roadmap for research on the reliability of lead-free solders. In FY2002, the NEMI Lead-free Task Force and the National Institute of Standards and Technology (NIST) have worked together to respond to the identified needs by:

- Identifying the most important lead-free solder data for the microelectronics community;
- Developing “a guide to recommended practices” for measuring the mechanical, thermal, electrical and wetting properties of lead-free solders. This document is being distributed to all interested parties through the NEMI and NIST websites and through NIST in hard copy form;
- Gathering into a single database existing physical and mechanical property data that have been developed by researchers around the world;
- Critically reviewing existing materials property data for the most important alloys for use in finite element analyses; and

- Providing a list of literature references on alloys, processing, reliability, environmental issues, and components for assisting in the implementation of lead-free solders.

In a second major activity with the NEMI Lead-Free Assembly Project, NIST completed the microstructure-based failure analysis of thermally-cycled assemblies as part of the project’s full-scale reliability trials with the new national standard Pb-free solder. The NEMI Final Report will be issued in early FY2003.

NIST is also working in collaboration with the IPC Standards Committees (most closely with members from Celestica, Lucent, Raytheon, Rockwell, and Shipley-Ronel) to establish reproducible solderability test standards for board assembly. Activities include: 1) providing benchmark experiments for the wetting balance tests to predict on-line solderability for a wide range of surface finishes, lead materials, and solder alloys; 2) developing a “best practice” for globule solderability test for small components and pads; and 3) evaluation of the effect of component lead geometry on industrial solderability tests.

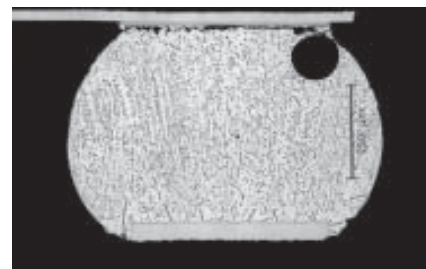


Figure 1: Metallographic cross-section of a lead-free SnAgCu solder joint showing fracture in the solder adjacent to the interface with the component following accelerated thermal cycling. Failure location is the same as for Sn-Pb eutectic solder, which this alloy is replacing as a standard alloy.

Highlights

- Sources of uncertainty have been established for wetting balance solderability tests leading to increased repeatability and reproducibility of tests.
- Recent flux studies performed at NIST led to a change in test procedures for the IPC/EIA/JEDEC J-STD 002 solderability standards.
- Research at NIST helped to separate the role of solder melting temperatures from solder paste wetting dynamics and the effect of air reflow.

Contributors and Collaborators

L.C. Smith (NIST); K.-W. Moon (University of Maryland); D. Napp (National Center for Manufacturing Sciences and associated consortium members); R. Gedney (NEMI Lead-Free Task Force and associated consortium members)

Mechanism of Sn Whisker Growth from Electrodeposits

The electrodeposition of metallic alloys has been central to the growth of the electronics industry. This is largely due to the exceptional properties exhibited by electrodeposited material as well as the favorable economy of scale associated with electrodeposition processes. A technology important to electronics manufacturing is the electrodeposition of Sn-based coatings and surface finishes to guarantee solderability. With the rapid move to Pb-free solder surface finishes, new test methods are needed for predicting the tendency of such coatings to form Sn whiskers that can lead to catastrophic failures.

Christian E. Johnson, Maureen E. Williams, and Kil-Won Moon

In FY2001, the National Electronics Manufacturing Initiative (NEMI) Pb-Free Task Force, of which NIST is a member, identified a serious concern of OEMs, contract manufacturers, and component manufacturers with the conversion from Sn-Pb to Pb-free surface finishes for circuit boards and component leads. It is well known that the use of pure Sn protective surface finishes can cause serious problems: tin whiskers (1 mm diameter and several mm long) can grow from the plated tin surface and cause electrical shorts and catastrophic failure. Historically Pb was added to Sn plate to prevent whisker growth, and, thus, the “whisker problem” disappeared. With the rapid move to environmentally-friendly Pb-free assemblies, the microelectronics industry must remove Pb from the surface finishes. For many applications, an electroplated Sn-based surface finish remains a preferred surface for ease of processing. However, the growth of whiskers is currently a perilous drawback.

Based on these needs, this NIST project is focusing on: 1) understanding the effect of alloying elements other than Pb on the tendency for whisker formation, 2) developing techniques to separate possible physical and microstructural factors affecting whisker formation, and 3) assisting the NEMI Standardization Technology Integration Group (TIG) with both test development and understanding the root causes of whisker formation. The Sn-Cu system was chosen as the most versatile for electroplating, since it is compatible with Sn-3.9Ag-0.6Cu and Sn-0.7Cu, the Pb-free solders selected as the new national standard alloys by NEMI for reflow soldering and for wave soldering, respectively.

Whiskers are generally believed to grow to relieve residual stress in electroplated Sn. However, the origin of this stress has not been determined definitively. Therefore, as a starting point, we focused on the relationship of microstructural change and whisker formation as a function of Cu additions. Increased Cu content reduced the grain size of the Sn deposit from 0.65 μm to 0.2 μm . Furthermore, Cu in deposits forms

Cu_6Sn_5 intermetallic compounds (IMC) at the Sn grain boundaries. In the absence of Cu additions, no whiskers were observed after one year of room temperature aging. However, with Cu additions, whiskers were observed within two days increasing to a density of 50/mm² after one year for the highest Cu levels.

Our current hypotheses are that a smaller grain size produces a higher level of intrinsic stress and that the presence of IMC particles at the grain boundaries may prevent relaxation of the stress. As a consequence, the stress level in the Sn-Cu deposits is relieved through whisker growth. To investigate this idea, cantilever beam test coupons were made from phosphor bronze and a commercial bright electrolyte. Using Stoney's Equation, an average planar stress of the deposited film was calculated from the deflection of the beam as a function of time. Preliminary results of pure Sn and Sn-Cu deposits indicated that the presence of the IMC particles in the Sn-Cu deposits inhibited stress relaxation. The compressive stress in the pure Sn deposit went from an initial level of 14 MPa to zero after four days. In contrast, the initial compressive stress in the Sn-Cu deposit was 32 MPa and after 100 days was still at 21 MPa. Whiskers were present after four days on the Sn-Cu sample, but after 100 days, the pure Sn sample was still whisker-free.

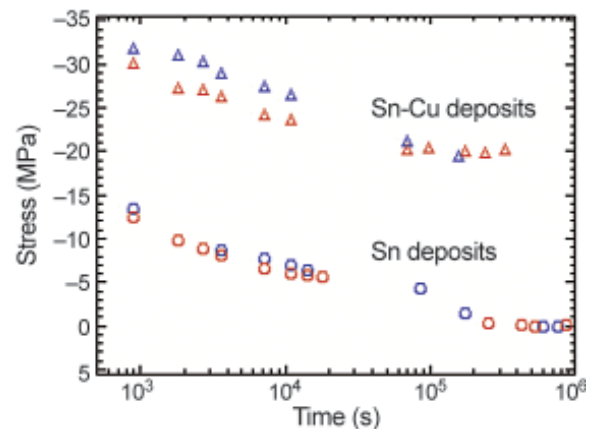


Figure 1: Calculated stress levels with and without Cu additions.

NIST is providing leadership in two NEMI whisker projects: identifying the fundamental growth mechanism and developing an accelerated test method. Our goal at NIST is to provide an understanding of the fundamentals of the whisker formation, which will ensure that the test developed by the NEMI group will have widespread applicability.

Contributors and Collaborators

W.J. Boettinger, G. Stafford (NIST); R. Gedney, I. Boguslavsky, P. Swaminath (NEMI project members)

Solder Reliability: Lead-Free Solder

The worldwide “green” movement in the electronics industry to replace lead–tin eutectic solders with lead-free solders creates a need for critical data on the industry’s new lead-free solder compositions for these design and reliability models. Members of the Materials Reliability Division are working with members of the Metallurgy Division, the Colorado School of Mines, and the National Electronics Manufacturing Initiative (NEMI) to develop and disseminate such data on lead-free solders.

Tom Siewert

Technical Description

The worldwide “green” movement in the electronics industry to replace lead–tin eutectic solders with lead-free solders creates a need for critical data on the industry’s new lead-free solder compositions for these design and reliability models. In fact, the NEMI website describes their view of the situation as, “The NEMI Lead-free Assembly Project was launched in 1999 to help North American companies develop the capability to produce lead-free products by 2001, with an eye toward total lead elimination by 2004. The goals and focus of the project were determined by the findings of NEMI’s 1998 roadmap and an industry task force formed by NEMI to investigate process and material considerations of lead-free electronics assemblies.” Their program plan is being implemented by the Lead-free Assembly Project. Project work is organized into five groups; however, our interests fit with only two: the Alloy Group (whose mission is to select a lead-free alloy, pursue an industry standard, and gather data) and the Reliability Group (who is analyzing data from a round robin that compared the performance of lead and lead-free alloys).

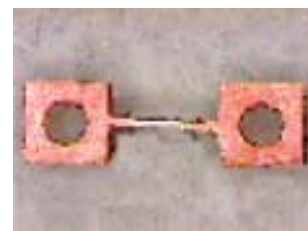
Development of our database started in April 2000 after we became members of the NEMI Lead-free Alloy Group, and we learned that modelers and production engineers need more data before they can switch their production lines to lead-free solders. The long history in the use of current lead-based solders means that these data sets are quite complete and widely available. The modelers and production engineers need equally complete sets of data on the various lead-free alternatives, so they can make informed decisions for their production applications. Researchers are rapidly developing corresponding data on lead-free alloys, but the data are widely distributed among the various technical journals and proceedings. In addition, it is beginning to appear as though differences in test procedures (e.g., loading rates and dwell times) may make some of the data inconsistent from laboratory to laboratory. Finally, individual researchers may be repeating some of the work of others, while other critical data needs are being overlooked. Making the existing data more widely available addresses all of these issues.

The database focuses on the three lead-free compositions that seem to have the widest interest: near the tin–silver–copper eutectic (Sn-4Ag-0.8Cu), near the tin–silver eutectic (Sn-4Ag), and near the tin–copper eutectic (Sn-0.8Cu). We have added data for eutectic tin–lead composition (Sn-37Pb) for comparative purposes, and have added data for other lead-free alloys as we find them. We have not added data for electronic materials other than solder.

Accomplishments

Our team continues to work with this NEMI Lead-free Alloy Group to gather into a single database the existing physical and mechanical property data that have been developed by researchers around the world. The most recent version of the database (4.0) is posted on the Materials Reliability Division’s website at: <http://www.boulder.nist.gov/div853/>. We have reported on the availability of the database in posters at national technical meetings, and the interest in the data is shown by this website being one of the top 5 sites for our Division (based on number of hits in the past year). Feedback from users of the database is guiding the addition of new data. We are also publishing a Standard Practice Guide that describes standardized procedures to facilitate the comparison of data between laboratories and to permit the combination of data from different sources into a single, comprehensive database.

We have developed the capability of tensile-testing solder samples that have test dimensions on the order of the sizes of solder balls used in flip-chip packages. The sample shown at right has a gauge length of 500 μm and a rectangular cross section that is 250 μm by 200 μm . A hydraulic tensile machine was outfitted with a control system that can reliably apply strain rates of 10^{-5} s^{-1} to the specimen. The strain is measured by capturing video images of the gauge section at magnifications of up to 750x. The images are then processed using image correlation techniques to measure the strain across the whole gauge section. Studies can now be conducted on the effects of phase sizes vs. structure size, lead free solder properties, and/or strain rate effects.



Contributors and Collaborators

T. Quinn, Y.-W. Cheng, C. McCowan, C. Handwerker (Metallurgy Division and Chair of NEMI Lead-free Alloy Group); Members of the NEMI Alloy and Lead-free Alloy Task Groups; J.C. Madeni, S. Liu (Colorado School of Mines)

Micrometer-Scale Reliability: Mechanical Behavior of Thin Films

Techniques for characterizing the mechanical behavior of thin films are being developed and applied. This is necessary since thin-film microstructures and properties are usually quite different from those of the same materials in bulk form. While the general principles of conventional mechanical testing apply to thin films, special test equipment and techniques are required. The ultimate goal of this effort is to test specimens produced by semiconductor fabrication equipment and similar in size to features on integrated circuit chips.

David T. Read

Technical Description

Thin films are an essential component of all advanced electronic devices. Understanding of failure modes in these devices, especially interface delamination, requires knowledge of the mechanical behavior of the films. Techniques for measuring such behavior are being developed and applied. Because the films are formed by physical vapor deposition, their microstructures, and hence, their mechanical properties, are quite different from those of bulk materials of the same chemical composition.

The objectives are:

- To develop experimental techniques to measure basic tensile properties, fatigue behavior, and fracture resistance in thin-film specimens fabricated and sized like materials used in actual commercial devices;
- To relate thin-film mechanical behavior to microstructure;
- To extend test techniques from their present level (1 μm thick, 10 μm wide) to smaller specimens that are similar in size to the conductive traces used in contemporary VLSI circuits (widths of 0.1 to 1 μm).

While the general principles of conventional mechanical testing are applicable to thin films, conventional test equipment and techniques are not. Because vapor-deposited films are of the order of 1 μm thick, the failure loads are of the order of gram-forces or less, and the specimens cannot be handled directly.

Accomplishments

Last year we reported the application of our recently developed force-probe technique to two new types of materials: 1) aluminum interconnect layers made in a commercial CMOS (complementary metal oxide semiconductor) fabrication facility, obtained through the MOSIS service, and 2) polycrystalline silicon made at Sandia National Laboratories. This year, we have demonstrated that the same technique is applicable to polymer materials used in electronic devices. We tested a commercial photodefinable polymer, a polyimide, between room temperature and 200°C.

The tensile section was 0.6 x 10 x 190 μm . Our success with these specimens from the three main families of materials, metals, ceramic-like, and polymers, and positive reports from other laboratories using similar techniques, has made us optimistic that standardized testing of thin films may be near.

The cured polyimide was very well behaved, with results as expected and consistent with the manufacturer's product bulletin; the elongation to failure was over twice the minimum value given by the manufacturer. This establishes that in this material, no "thin film" effects alter the tensile properties, down to a thickness of 0.6 μm . Changes in polymer mechanical properties in films thin enough to constrain the arrangement of the chain-like polymer molecules have been anticipated and may still occur for thinner specimens.

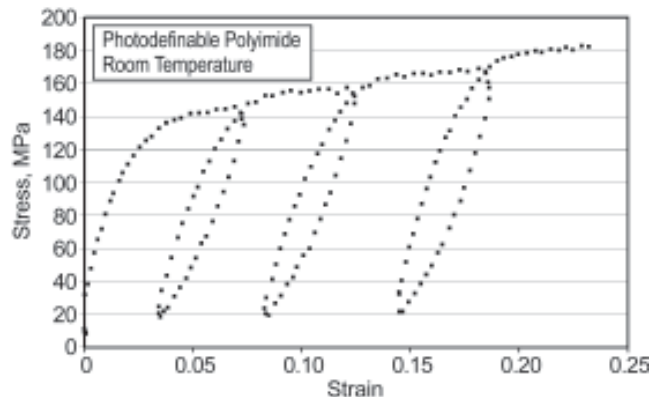


Figure 1: Stress-strain curve of photodefinable polyimide at room temperature showing hysteresis loops.

Three other efforts were pursued in this project: continuation of our testing of CMOS aluminum; fabrication and testing of microtensile specimens representative of copper interconnect lines in microelectronics devices; and extension of our microtensile test technique to exotic materials such as carbon nanotubes. While CMOS aluminum specimens down to 2 μm wide were successfully fabricated, this set of specimens behaved in a very brittle manner, more brittle than the previously tested set. We are applying advanced analytical tools to find the cause of this behavior. Our preliminary results on copper are similar to those for other metals we have tested, but the details are currently covered by a nondisclosure agreement with the supplier of the specimens. Our initial experiments with carbon nanotubes are described elsewhere.

Contributors and Collaborators

Y.-W. Cheng, J.D. McColskey (NIST); R. Emery, T. Scherban (Intel); B. Yeung, (Motorola); C. Litteken (Stanford University)

Electronic Packaging and Components: Packaging Reliability

We are developing methods to examine materials and interfaces in electronic packaging applications and elucidate the damage mechanisms. Our current focus is on advanced packaging structures and embedded passive materials using electron-beam moiré to measure mechanical strain, and thermal microscopy to measure heat flow and thermal properties on increasingly smaller size scales.

Andrew Slifka and Elizabeth Drexler

Technical Description

The microelectronics industry is moving rapidly toward higher-density components of smaller size using less expensive materials. One move in this direction is the advent of embedded and integrated passive components in printed circuit boards (PCBs) and another is the use of PCBs in various types of grid array packages. These organic-based PCBs can have a large coefficient of thermal expansion (CTE) in comparison with many materials found in their proximity. This CTE mismatch can reduce the reliability of electronic packaging systems by causing localized stress. The CTE mismatch in flip-chip packages is also a source of failure and fatigue.

We are investigating the damage induced from CTE mismatches between organic materials, organics and metals, organics and ceramics, and organics, metals and ceramics to determine the initiation of damage and the ultimate failure mechanisms in these systems. Electron-beam moiré is employed to measure displacements and calculate mechanical strain due to thermomechanical loading. Thermal microscopy is used to measure changes in interfacial thermal resistance in order to detect the onset of thermomechanical damage at that interface before any surface manifestation is visible.

We are developing new measurement methods, both thermal and mechanical, using scanned-probe microscopy (SPM) in order to characterize packages at increasingly smaller size scales.

Accomplishments

Building on the preliminary measurements made in FY01, we developed the thermal SPM into a quantitative technique. We used an industrial embedded resistor (Figure 1) to make comparative measurements between the SPM thermal system and the IR microscope. Similar temperature differences can be achieved with both the SPM and IR systems, although two different heating techniques are used due to geometric constraints. Improved spatial resolution is motivating the move to the SPM. With increased miniaturizing in electronic

packaging, the IR microscope no longer has the needed resolution to detect materials and interfaces in future, and even some current, packages.

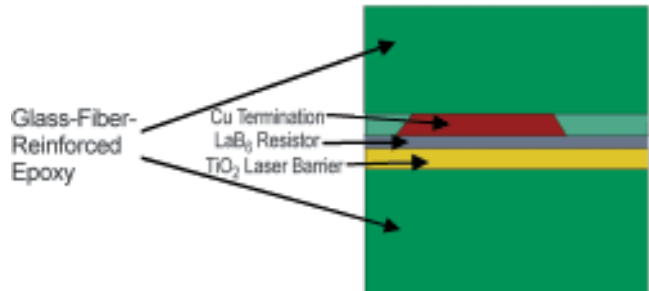


Figure 1: Schematic of the materials contained in the embedded resistor specimen and their relative positions.

Mapping of the change in interfacial thermal resistance in an embedded resistor specimen, shown in Figure 2, among the various material combinations shows the increase in degradation with respect to thermal cycling (-55 to 125°C). The interface between the TiO_2 -filled epoxy (laser barrier) and the ceramic embedded resistor shows signs of damage within 5 thermal cycles. Corresponding electron-beam moiré data show that maximum strains are found in the laser barrier and in the resin-rich regions of the printed circuit board, particularly between the resistors, where unfilled resin collects during lamination.

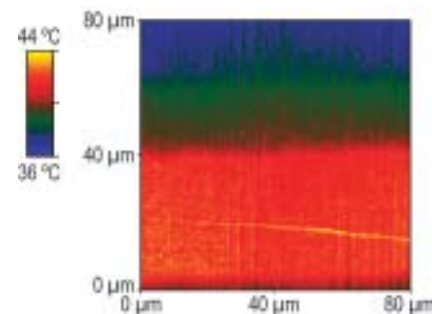


Figure 2: Thermal SPM image showing the laser barrier, resistor, and copper (from top to bottom), 8°C , full scale.

In collaboration with the Jet Propulsion Laboratory, we are looking at techniques to mitigate the destructive consequence of CTE mismatches in flip-chip packages. Strains in specimens were measured before, after, and without the microwave process.

Contributors and Collaborators

J. Felten (DuPont Technologies, Research Triangle Park, NC); V. Shah (MicroFab Technologies, Plano, TX); R. Snogren (SAS Circuits, Inc., Littleton, CO); N. Budraa (Jet Propulsion Laboratory, Pasadena, CA)

Electronic Packaging and Components: Acoustic Loss in Piezo Crystals

Langasite, langatate, and langanite are piezoelectric materials that show promise of providing characteristics superior to quartz for a variety of electronic oscillator and filter applications. The acoustic loss of these crystals is being studied in our laboratory to identify and quantify the dominant physical mechanisms that degrade performance, including the intrinsic phonon–phonon mechanism. Through this work, the project seeks to provide guidance to other researchers in minimizing the acoustic loss and determining the most promising material to pursue among this group of compounds.

Ward Johnson and Sudook Kim

Technical Description

Langasite ($\text{La}_3\text{Ga}_5\text{SiO}_{14}$), langatate ($\text{La}_3\text{Ga}_{5.5}\text{Ta}_{0.5}\text{O}_{14}$), and langanite ($\text{La}_3\text{Ga}_{5.5}\text{Nb}_{0.5}\text{O}_{14}$) have attracted significant attention in recent years as candidate materials for improved electronic oscillators and filters. The potential advantages of these crystals over quartz include higher piezoelectric coupling (which enables devices to be made smaller), lower acceleration sensitivity, and higher Q (which reduces phase noise and enables higher-frequency operation). These materials also have no phase transition below the melting point, which allows devices to be operated at high temperatures and provides the potential of producing large-diameter wafers (for surface-acoustic-wave devices) more easily and cheaply than with quartz.

Values of the acoustic loss Q^{-1} reported in the literature vary widely and may not represent the intrinsic limits of these materials. Therefore, current data provide little guidance in establishing a focus of further research. This project seeks to remedy this situation by identifying the dominant contributions to Q^{-1} in langasite, langatate, and langanite. The known physical mechanisms that can significantly contribute to Q^{-1} include dissipation through external mechanical contact, defect anelasticity, nonlinear coupling to other modes, and intrinsic coupling to thermal phonons (phonon–phonon loss through the Akheiser mechanism).

Accomplishments

In FY02, an experimental system was constructed for measuring Q^{-1} and frequencies of resonant shear modes of Y-cut plano-convex disks in vacuum at temperatures from 150 K to 1000 K. The plano-convex geometry of the sample has the effect of localizing the vibrations of certain modes near the center, so damping from mechanical support at the edges is essentially

eliminated. Acoustic resonance measurements are performed using tone-burst direct piezoelectric coupling with planar electrodes above and below the sample. Q^{-1} and resonant frequencies are determined through analysis of free-decay waveforms in the time domain. The configuration of the sample, supporting structure, and copper electrodes are shown in Figure 1.

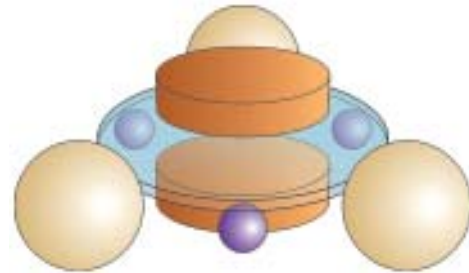


Figure 1: Plano-convex single-crystal disk supported on sapphire spheres and centered laterally by larger alumina spheres. Driving electrodes are above and below sample.

Measurements of Q^{-1} in langatate have been performed as a function of frequency, temperature, external mechanical contact, and vibrational amplitude. As shown in Figure 2, Q^{-1} varies significantly between samples which are taken from the same crystal boule. The dominant contributions to Q^{-1} in these measurements have not yet been identified. However, the contribution from external damping has been determined to be insignificant, except for the lowest mode near 2 MHz. At higher amplitudes, a nonlinear contribution is observed.

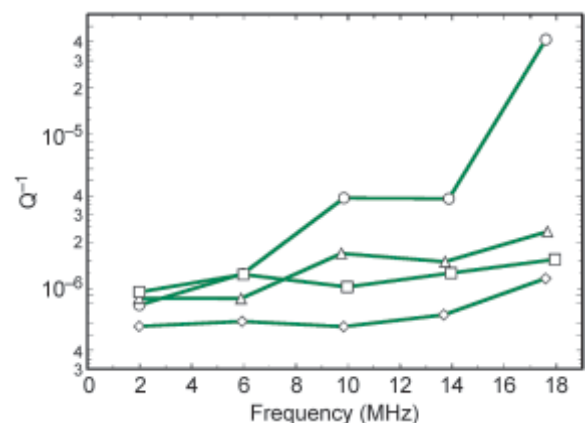


Figure 2: Q^{-1} versus resonant frequency in a Y-cut plano-convex disk of langatate at ambient temperature.

Contributors and Collaborators

R. Smythe (Piezotechnology, Inc., Orlando, FL)

This project is partially supported by a grant from the U.S. Army Research Laboratory.

Combinatorial Materials Research: Interconnects to Optoelectronic Materials

GaN and related nitrides have been identified as important materials for the realization of solid-state lighting, UV/blue lasers, LEDs and photodetectors. The engineering of improved electrical contacts to these devices is of particular industrial importance. This project develops a strategy for industry to reduce contact resistance, increase visible light transmittance, and improve thermal and mechanical stability of ohmic contacts to a variety of optoelectronic devices. Due to the large number of possible materials combinations and process variables involved, a combinatorial approach is valuable.

Albert V. Davydov and Leonid A. Bendersky

Typical electrical contacts to p-type GaN devices consist of thin film Au/Ni bi-layers, but contact resistance and reliability are far from ideal. The goal of this project is to establish techniques for industry to use to rapidly develop improved contacts for GaN and other compound semiconductor devices. A combinatorial approach (looking at Au/Ni ratio and metal film thickness) integrated with thermodynamic and diffusion modeling is being used to quantify the relationship between physical properties such as electrical resistance and optical transmittance of metal contacts and the fundamental microstructural and compositional properties of the metal-to-GaN interface.

Thermodynamic information and diffusion data are being evaluated for the Au-Ni-Ga-N system to help interpret the metallurgical reactions in the Au/Ni/GaN structures. To date, we have measured the thermal stability of the GaN compound and modeled the P-T-composition phase diagram for the Ga-N system. In addition, the Ni-Ga-N phase diagram has been evaluated experimentally and thermodynamically and presented at the CALPHAD-2002 Meeting.

A combinatorial array of Ni/Au bi-layer contacts of varying compositions has been fabricated by physical vapor deposition (e-beam evaporation) on commercial GaN wafers. The thickness of each metal layer varied discretely from 5 to 85 nm using a motion-controlled shutter system, producing an array of 88 elements (Figure 1(a)). The composition and microstructure of the contacts were examined with XRD (with Prof. I. Takeuch, UMD), optical microscopy, SEM and AFM. The transparency of metal layers to visible light was determined by reflectometry and transmission measurements. From transmission and XRD measurements (Figure 1(b, c)), we have identified library elements with optimum as-deposited Au/Ni compositions that are highly transparent and of good crystalline quality with epitaxial metal layers.

In FY2003, we will fabricate combinatorial libraries with an extended compositional range to

develop thermodynamic stability data for GaN with other metal contact materials as well as continue to establish the analysis techniques for quantifying phase transformations and interdiffusion in these GaN/metal contact systems and developing the relationships between phase transformations, microstructures, and electrical performance.

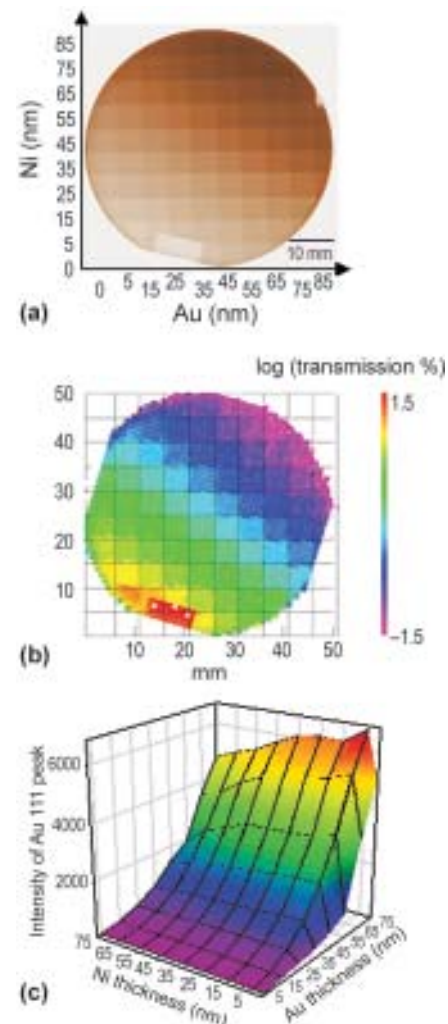


Figure 1: (a) Array of as-deposited Au/Ni bi-layered metallization (88 elements) on 2-inch GaN/sapphire wafer; (b) Optical transmission imaging of the above sample at $\lambda = 450 - 713$ nm; (c) XRD mapping of Au 111 reflection from all 88 Au/Ni elements.

Contributors and Collaborators

W.J. Boettinger, D. Josell, A.J. Shapiro (Metallurgy Division, MSEL); P.K. Schenck, J.E. Blendell (Ceramic Division, MSEL); I. Takeuchi (University of Maryland); V.A. Dmitriev (Technologies and Devices International, Inc.)

Optical and Structural Characterization of Optoelectronic Semiconductors

Photonics manufacturers need to better understand how composition, strain, inhomogeneity and defects affect the performance of optical emitters and detectors made from III-V compound semiconductors. In the Optical and Structural Characterization of Optoelectronic Semiconductors Project, we are measuring critical properties of thin film structures relevant to device performance by a variety of spectroscopic techniques. The project is currently focused on deep UV to near IR (250 nm to 850 nm) emitting materials: $Al_xGa_{1-x}As$, $Al_xGa_{1-x}N$ and $In_yGa_{1-y}N$.

Lawrence Robins and Grady White

Medium to wide bandgap III-V semiconductors enable display, lighting, and data storage technologies, based on their optical emission and their ability to detect at deep UV to near IR wavelengths. Progress in the development of GaN, $Al_xGa_{1-x}N$ and $In_yGa_{1-y}N$ devices (250 nm to 550 nm) has been hampered by problems with materials growth and structure, such as film/substrate lattice mismatch, high defect and impurity concentrations, and structural/compositional inhomogeneity. $Al_xGa_{1-x}As$ (650 nm to 850 nm) is a better developed technology, but the industry still needs improved accuracy in measurements of alloy composition and residual strain. We have, therefore, undertaken several initiatives to address these needs for improved metrology methods and accurate measurements.

- 1) A calibration curve was determined for the dependence of the photoluminescence (PL) emission energy on Al fraction (x) in $Al_xGa_{1-x}As$ films for $x < 0.37$, near room temperature, based on reflection high energy electron diffraction (RHEED) and wavelength dispersive spectroscopy (WDS) measurements of x .
- 2) Correlated Raman and PL measurements were performed on $Al_xGa_{1-x}As$ films as a function of applied biaxial stress to 350 MPa. Two primary Raman peaks, described as AlAs-like and GaAs-like, were observed in films with $x = 0.2$ and $x = 0.5$. The differing stress and composition dependencies of the Raman and PL peaks allow us to determine both the Al fraction and the magnitude of the stress. Measurements suggest that the stress coefficient of each Raman peak is approximately constant as a function of x , with the AlAs-like peak showing a larger stress coefficient than the GaAs-like peak.
- 3) The ordinary refractive index, $n_o(E)$, and absorption coefficient, $\alpha(E)$, were measured in the 200 nm to 2500 nm range for several $Al_xGa_{1-x}As$ films by spectroscopic transmittance, $T(E)$, and reflectance, $R(E)$, correlated with discrete-wavelength prism-

coupled waveguide-mode measurements of n_o . EDS measurements of x enabled determination of the x dependence of $n_o(E)$ and $\alpha(E)$. Transmittance, $T(E)$, and reflectance, $R(E)$, spectra of a representative sample are plotted in Figure 1.

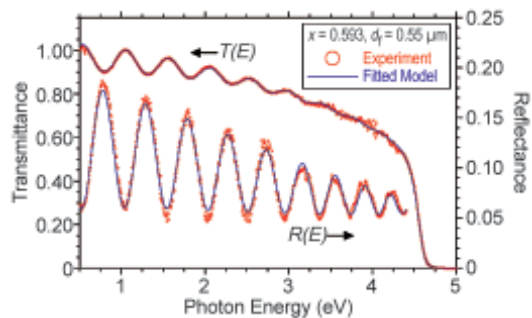


Figure 1: Transmittance and reflectance measurements (red) and model (blue) for a $Al_xGa_{1-x}N$ sample.

The index–film thickness product $n_o(E)d_f$ was determined from the spacing of the interference fringes in $T(E)$ and $R(E)$; similarly, $\alpha(E)d_f$ was determined at energies near the bandgap from the absorption cutoff of $T(E)$. To determine the individual factors n_o , α , and d_f , a two-Sellmeier-term model for $n_o(E)$ was adjusted to best match the n_o values from the discrete wavelength waveguide mode measurements, while simultaneously fitting the $T(E)$ and $R(E)$ data. The $n_o(E)$ and $\alpha(E)$ curves obtained from this multiple optimization procedure are shown in Figure 2.

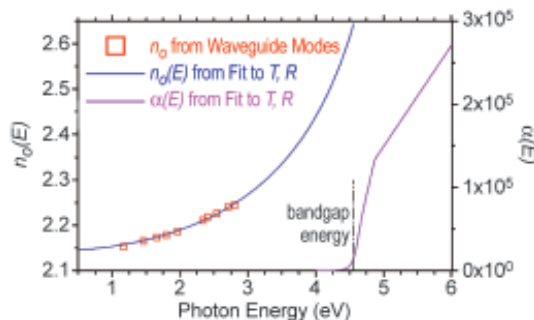


Figure 2: Ordinary refractive index and absorption coefficient obtained in the optimization procedure.

Contributors and Collaborators

C.E. Bouldin, A.J. Paul, M.D. Vaudin (Ceramics); J.T. Armstrong, R.B. Marinenko (Surface and Microanalysis); K.A. Bertness, N.A. Sanford (Optoelectronics); A.V. Davydov, A.J. Shapiro (Metallurgy); J.G. Pellegrino (Physical and Chemical Properties); A.V. Dmitriev, D.V. Tsvetkov (TDI); S. Keller, U.K. Mishra, S.P. DenBaars (UCSB)

Micrometer-Scale Reliability: Strain in Photonic Semiconductors

The compound semiconductor photonics industry seeks to both measure and control strain that develops during the course of device fabrication. In the Materials Reliability Division, we are developing electron diffraction methods for measuring and mapping elastic strain distributions. The methods are applied to phase transition-induced strains for the case of oxide formation in vertical cavity surface-emitting lasers, and to lattice parameter mismatch strains for self-assembled quantum dots.

Robert R. Keller and Roy H. Geiss

Technical Description

Vertical cavity surface-emitting lasers (VCSELs) have, as an integral component, oxide layers to act as apertures resulting in record low threshold currents and high efficiencies. These apertures are grown by selective wet oxidation of AlGaAs layers (compositions typically contain 98–100% AlAs) situated between GaAs layers. Upon transformation from AlGaAs, the aluminum oxide undergoes a large volume contraction in excess of 6%. The exact magnitude of the contraction is not well-characterized as the theoretical volume change exceeds 20% while the few experimental measurements suggesting 6–7% are based on TEM images of layer thickness changes. The contraction can be manifested as elastic strain in adjacent GaAs layers, dislocations in GaAs and in the interfaces, and also as delamination.

We are using TEM and SEM electron diffraction methods to measure elastic strain states via determination of lattice spacings and angles. While the TEM method provides superior spatial and strain resolutions, the SEM method is not subject to the difficulties associated with thin foil preparation, namely site-specificity and stress relaxation induced during thinning. Here, we report progress on SEM measurements by electron backscatter diffraction (EBSD).

Accomplishments

The EBSD method has seen little successful application to the measurement of elastic strains due primarily to the low signal-to-noise inherent in the detection system. We have made exciting progress along two avenues for strain measurement in oxidized AlGaAs/GaAs multilayer structures. We started with the most direct measure of strain available in the diffraction patterns, namely the spacing of the Kikuchi-like bands of high intensity. These bandwidths are proportional to Bragg angles and therefore provide a direct link to interplanar spacings in the crystal. Figure 2 of the

Technical Highlight on this subject shows an example of an indexed pattern with a computer-simulated pattern overlaying an experimental result. Rather than measure bandwidths directly from the data, we have begun to apply simple image mathematics to accentuate the differences between patterns showing strain and those showing no strain.

We have, to date, been able to detect very small differences in strain from locations within the crystal that are only tens of nanometers apart. Quantification of these strains is underway.

The other aspect of EBSD-based strain measurement makes use of automated collection of diffraction patterns, followed by analysis of pattern sharpness. If the elastic strain varies considerably within the volume of material sampled by the electron beam (of approximate diameter 50 nm), then there will be a continuously changing lattice parameter that causes a continuously changing Bragg angle. In the pattern, this effect broadens the edges of the Kikuchi-like bands and makes the pattern more diffuse. A larger strain gradient leads to more diffuseness. The extent of diffuseness can be quantified and this effect mapped as shown in Figure 1. Here, each pixel represents a different beam position, and greater diffuseness is represented by a darker intensity. In this figure, we concentrate on the colored pixels within the GaAs layers only.

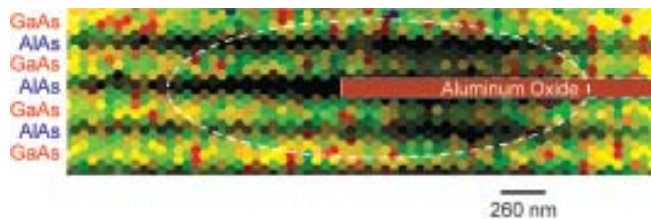


Figure 1: Crystallographic orientation map with darker pixels indicating greater pattern diffuseness or strain.

The strain field around the aluminum oxide growth front (indicated schematically in brown) can be qualitatively seen to extend over a few GaAs/AlAs bilayers in directions normal to the layers. It extends even further in directions parallel to the layers as indicated schematically by the dashed white oval.

We are in the process of evaluating means for quantifying the relationship between EBSD pattern diffuseness and magnitude of elastic strain gradients.

Contributors and Collaborators

A. Roshko, S. Lehman, K. Bertness (Optoelectronics Division, EEEL)

Magnetic Properties and Standard Reference Materials

Users of magnetic materials, including the recording industry, the permanent magnet industry, and the manufacturers of electric motors and transformers of all types, need standard reference materials (SRM's) to calibrate instruments used to measure the critical magnetic properties of their starting materials. The magnetic materials group is in the process of developing such standards. Methods for improving the efficiency and accuracy of measuring and characterizing magnetic materials of industrial importance, including measurement of magnetic susceptibility over wide frequency ranges, are also under investigation.

Robert D. Shull and Robert D. McMichael

In collaboration with scientists from universities, industry, and other Divisions at NIST, magnetic materials important to the scientific and industrial communities are prepared and methods for the improved measurement of their properties are developed. Standard Reference Materials for the calibration of existing and planned instruments used in the measurement of magnetic properties are developed and produced. An equally important parameter to know how to measure is time dependence of magnetization. Consequently, methods for the characterization of accommodation and aftereffect in magnetic recording and permanent magnetic materials are developed. Models are also developed for determining the most efficient methods to fully characterize the hysteresis and magnetostriction in magnetic materials.

Commercial instruments for the measurement of magnetic properties are relative instruments that rely on known samples for their calibration. To produce standard samples for such instruments, an absolute magnetometer was developed and assembled at NIST. A picture of this instrument is shown below.



Figure 1: Absolute magnetometer.

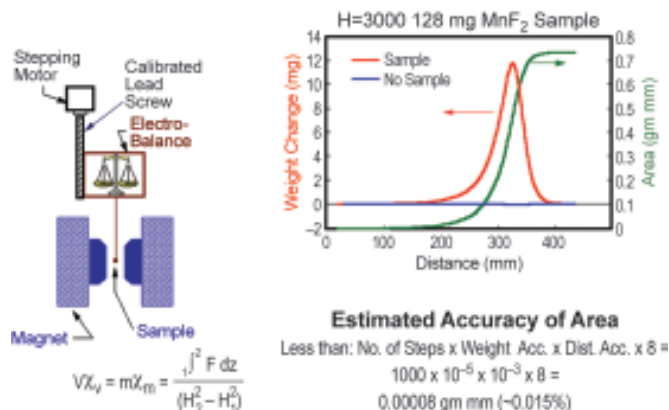


Figure 2: Thorpe-Sentfle Method for Absolute Susceptibility Measurement.

Prior to FY02, two SRM's were issued: a nickel sphere (SRM 772a) and a nickel disc (SRM 762). The measurements for the complete series of magnetic SRMs are made using the Thorpe-Sentfle method shown above. This technique has the advantage of not requiring knowledge of the field gradient anywhere in the apparatus. As that is the largest source of error, higher accuracy is possible.

We measure the susceptibility by physically moving the sample to various positions from the field center to some distance outside of the magnet measuring the magnetic force and then integrate that force vs. distance relationship.

Two new SRMs were developed this year. The first was a 1 mm diameter yttrium iron garnet (YIG) sphere for use in calibrating the more sensitive ranges of magnetometers (SRM 2853). In addition, it will be useful in calibrating very sensitive instruments such as alternating gradient magnetometers and SQUID magnetometers. Because of its high resistivity, the yttrium iron garnet sphere should also be useful for calibrating magnitude and phase in alternating current magnetometers. The second SRM is a platinum cylinder paramagnetic susceptibility standard (SRM 764a). This will be useful in calibrating the zero field point and linearity of magnetometers due to its paramagnetic nature, and it will also be useful for calibrating the field scale after the moment scale has been calibrated.

Contributors and Collaborators

A.J. Shapiro, R.V. Drew; S.D. Leigh (ITL); Industrial and academic collaborators: L.J. Swartzendruber, D.E. Matthews, G.E. Hicho, L.C. Smith, L.H. Bennett, E. Della Torre (George Washington University)

Magnetic Properties of Nanostructured Materials

In the past decade, there has been a remarkable improvement in the technology for materials preparation resulting in present day's capability of controlling morphology and features at the nanometer level. In magnetism, such control allows the fabrication of nm-thick composite materials of dissimilar magnetic behavior, leading to materials with novel bulk magnetic character and unusual properties. We are providing materials metrology necessary for U.S. industry to understand the behavior of these new materials and take advantage of the novel properties.

Alexander J. Shapiro and Robert D. Shull

Greater information storage on recording discs is being accomplished by reducing the size of the regions in which information is stored down to nanometer sizes. Unfortunately, when those regions become too small, the material ceases to be ferromagnetic (FM) and, instead, becomes superparamagnetic and no longer retains magnetic information. In order to exceed the so-called "superparamagnetic limit," the recording industry has recently introduced magnetic media containing two layers of a ferromagnet separated by a sub-nanometer thick layer of Ru. In this structure, the thickness of the nm-diameter regions has been effectively increased by providing magnetic coupling between the two ferromagnetic layers via the in-between Ru. Consequently, the volume of the element has been maintained large, even though the lateral dimensions of the recording "bit" have been decreased, thereby enabling retention of the ferromagnetic state. However, for this new type of media, it is unknown how long information will be retained in those "bits" and what sort of fields are necessary for reversing their magnetization. We have addressed this problem by imaging the magnetic domains in this new type of media using the magneto-optic indicator film (MOIF) technique developed in our laboratory (Figure 1).

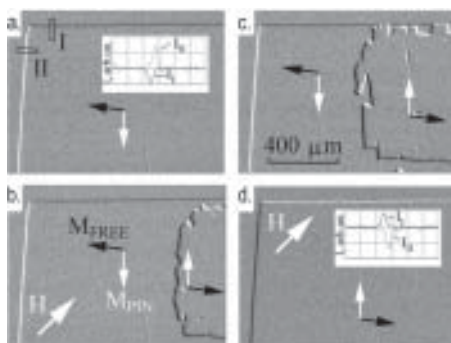


Figure 1: MOIF image of the remagnetization process of a Co/Ru/Co homogeneous structure containing pinholes in the Ru in a field oriented along the total magnetization vector. (a) $H = 0$ mT after magnetization in a field of +60 mT; (b) $H = -9.4$ mT; (c) $H = -9.4$ mT after a 5 sec. wait; (d) $H = -13.0$ mT. The inserts in (a) and (d) show the intensity change of the MO signal.

The first conclusion from the MOIF observations was that, surprisingly, the magnetization vectors in the two FM layers in this 3-layer structure were not colinear as originally assumed. In Figure 1, the lack of colinearity is seen by the 100 degree angle between the magnetization vectors (one white and the other black) of the two FM layers. As a consequence of this non-colinearity, the magnetization reversal mechanism now involves the cooperative behavior of both Co layers simultaneously, leading to different coercive fields and switching speeds. Figure 2 (e-h) shows that this non-colinearity is due to the presence of pinholes in the 0.5 nm thick Ru.

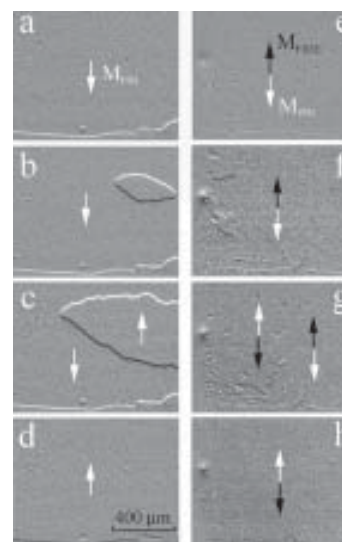


Figure 2: MOIF image of the remagnetization process of a Co/Ru (a-d) and a Co/Ru/Co (e-h) thin film containing no pinholes in a field oriented along the total magnetization vector. H is directed vertically in the figure at increasing magnitude from 4 mT to 4.8 mT (a-d) and from 2 mT to 54 mT (e-h).

For the Co/Ru/Co multilayer with no pinholes, the two FM layers have magnetization vectors which are colinear. With pinholes present, the greater their number, the greater their effect on the magnetic spin misalignment shown in Figure 1. Since most sub-nanometer thin films contain pinholes, these results clearly demonstrate the importance of knowing the effect of these defects. One of the ramifications of the non-colinearity is the presence of time dependence in the coercivities of the stored information, a particularly deleterious situation. Information safely stored now may not be safely stored tomorrow. Two papers have been published presenting these results and a third is in progress to clarify the situation.

Contributors and Collaborators

Alexander J. Shapiro, Robert D. Shull, Robert D. McMichael, William F. Egelhoff (NIST); Valerian I. Nikitenko (Johns Hopkins University); Vladimir S. Gornakov (ISSP, Russian Academy of Sciences, NIST)

Nanomagnetodynamics

For GHz data rate hard drives, magnetic memory chips and other high-frequency magnetic devices, magnetization damping will be an important factor affecting performance. Another consequence of damping is thermal fluctuations that cause sensor noise and data loss in media. We provide industry with: 1) an improved understanding of magnetic damping mechanisms, 2) improved magnetic damping measurements and standards, and 3) data and methods for controlling magnetic damping in technically relevant materials.

Robert D. McMichael

This project is concerned with the metrology and mechanisms of magnetization damping, a process where magnetic energy is dissipated as the magnetization comes to equilibrium. The same mechanisms that allow damping also allow thermal energy to cause magnetization fluctuations that cause noise in sensors such as disk drive read heads and data loss in recorded media. Damping mechanisms are recognized as being important both for GHz data rate writing and reading processes and for long-term stability of stored data. A convenient measurement of damping is the ferromagnetic resonance (FMR) linewidth, a measurement that is complicated by the presence of inhomogeneities.

In FY2002, our accomplishments include:

1) a very successful model of ferromagnetic resonance in inhomogeneous films (see highlight), 2) demonstrations of the effects of intentional defects, 3) measurements of damping in thin magnetic metal films by spin transport

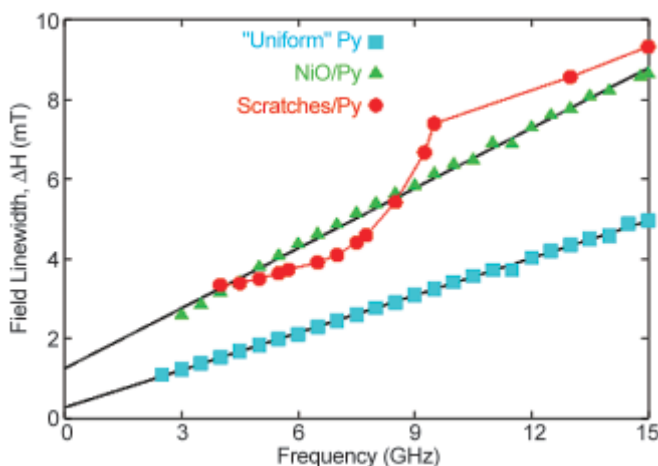


Figure 1: Increased FMR linewidth resulting from intentionally-created defects created to clarify the effects of nanoscale defects on FMR damping measurements. Our modeling describes the effects of the random coupling to the polycrystalline, antiferromagnetic NiO.

into normal metals, and 4) measurements of the very low damping in high moment, soft materials under development for read heads.

We have measured the intrinsic linewidth of Permalloy films, and we have found that it follows one of several proposed phenomenological forms. This data has been very valuable to theorists working on physical damping mechanisms.

One novel physical damping mechanism is damping via spin-polarized electron transport. It had been shown elsewhere that additional damping can be created by polarized electrons propagating into Pt or Pd surface layers. We have shown that the enhanced damping can be achieved with as little as 0.5 nm of Pt, and we have shown that the effect is substantially reduced by a Cu spacer between the Permalloy and Pt that is as thin as 0.5 nm. The abrupt decrease with a thin Cu spacer suggests that the damping enhancement has a contact component in addition to the spin transport component.

In FY2002, four papers related to this project were published, five contributed talks presented and three invited talks given at Seagate Research, U.C. San Diego, and a National Storage Industry Consortium meeting, and two more invitations have been received to speak at the 47th annual MMM conference in November 2002.

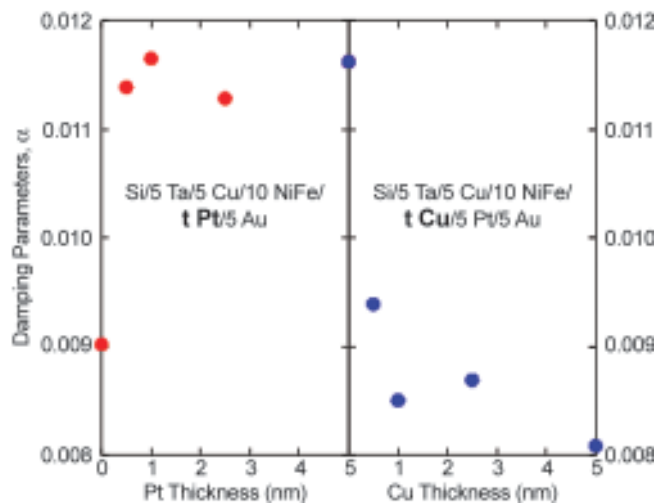


Figure 2: Effect of Pt overlayers on damping in Permalloy films. The effect shows how spin polarized electron transport across the interface contributes to damping.

Contributors and Collaborators

R.D. McMichael, A.B. Kunz, D.J. Twisselmann, A.P. Chen, W.F. Egelhoff (Metallurgy Division, MSEL); S.E. Russek (EEELM); E. McHenry, H. Okumura (Carnegie Mellon University)

New Materials for Ultra-High Density Data Storage

The objective of this program is to provide assistance to U.S. companies in the ultrahigh density data storage industry, which includes such products as hard disk drives and magnetoresistive random access memory chips. Our work provides U.S. companies with significant competitive help by investigating the scientific issues underlying the manufacturing process. Often, this scientific understanding will point the way to improved manufacturing processes. One such example is illustrated in the figures below.

William F. Egelhoff, Jr.

Hard disk drives play a crucial role in the information revolution. The World Wide Web is stored on millions of hard disk drives around the world. The exponential growth of the Web has depended on the exponential growth in hard disk storage capacity. Maintaining these exponential growth rates is one of the great challenges of the information age.

Today, giant magnetoresistance (GMR) is the current technology used for read heads in hard disk drives. It is unrivaled in its ability to read sub-micron-sized bits at gigahertz frequencies. However, the time is not far off when technologies better than GMR will be needed to maintain the historical exponential growth rates in storage density.

Our aim is to assist the U.S. companies that are developing these new technologies. One promising new technology is magnetic tunnel junctions (MTJs). MTJs are magnetic thin films with a typical layer structure of Co/Al₂O₃/Co. Electrons tunnel from one Co layer to the other through the Al₂O₃. One problem with MTJs is that they are not highly reproducible.

To understand the origin of this problem, NIST began a series of measurements at the Magnetic Engineering Research Facility (MERF) to determine the fundamental growth mechanisms in MTJ fabrication. MERF is a unique facility specifically designed to study surface and interface effects occurring during the growth of magnetic thin films for ultrahigh density data storage applications. The results at MERF identified interdiffusion at the Al/Co interface as a problem in the growth of MTJs, as illustrated in Figure 1.

When the Al is oxidized to make Al₂O₃ some of the Al remains in metallic form in the Co. The extent of the interdiffusion is highly susceptible to small changes in experimental conditions. As a result, nominally identical MTJs exhibit a lot of scatter in their performance data, as illustrated in Figure 2.

NIST demonstrated at MERF that oxidizing two atomic layers of the Co surface prior to the Al deposition provided an excellent diffusion barrier and

that the Al reduced the Co oxide back to Co metal. NIST transferred this technology to Read-Rite, which found greatly improved manufacturing uniformity for MTJs and an improved magnetoresistance when this approach was used.

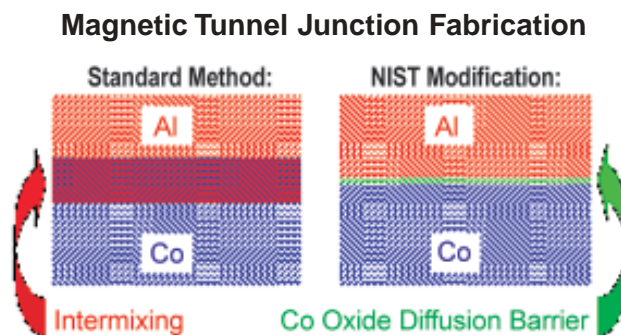


Figure 1: An illustration of the intermixing that occurs in the standard method of MJT fabrication when Al is deposited on Co and the NIST modification using a thin Co oxide diffusion barrier to prevent the intermixing.

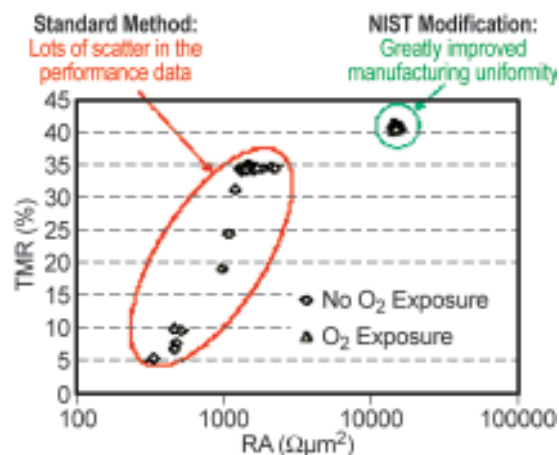


Figure 2: Read-Rite Corp. data on magnetic tunnel junctions.

“The results were amazing. The scattered data collapsed into a single point.”

Dr. H.C. Tong
Director of Advanced Read-Head
Research, Read-Rite Corp.

Contributors and Collaborators

W.F. Egelhoff, Jr., R.D. McMichael (NIST/MSEL); M.D. Stiles (NIST/Physics); 6 U.S. Corporations, the Naval Research Laboratory, 7 U.S. Universities, and 13 International Universities

Nanotribology

The head-disk interface has become an important scientific and technological issue in the data storage industry. To reach 155 Gb/cm² areal density and fast data transfer, the spacing between the head and the disk is shrinking to 3.5 nm for speeds approaching 40 m/s. Occasional contacts will test the strength and robustness of the protective carbon and lubricant coatings, each of which is only one nanometer thick. Measuring and evaluating material properties and their response to impact under these conditions has become a significant technological need.

Stephen Hsu, Richard Gates, Patrick Pei, Pu-Sen Wang, Jerry Chuang, and Dan Fischer

Ceramics Division researchers continue to work with the National Storage Industry Consortium (NSIC) as members of the Tribology Working Group. We have achieved significant progress in four project areas: 1) the development of a high-speed impact test to simulate head-disk collisions under ramp-load and unload operating conditions; 2) the creation of a finite element model for calculating stress concentrations and deformation as a result of such impacts; 3) the development of a master calibration sample for film thickness measurements of complex hydrocarbon molecules on hard disks in the one nanometer \pm 0.2 nm range; 4) the development of an electron spin resonance technique to measure the unpaired electrons in carbon overcoats with MMC Corporation.

These projects, taken together, represent our efforts in addressing two crucial technological issues facing the magnetic hard disk industry: how should the disk be protected from occasional high-speed head-disk contacts when the head is flying faster and lower; how should we define surface reactivity and bonding in new carbon overcoats while ensuring durability.

NSIC has set the ambitious goal of reaching 155 Gb/cm² areal density by 2006 with a concurrent increase in data transfer rate approaching 100 Gbit/s. This translates to a 10-fold increase in capacity in four years.

To increase the areal density, the flight height and the carbon overcoat thickness must be reduced to 3.5 nm and 1 nm respectively. Since the protection of the disk depends on the combination of the lubricant and the carbon overcoat, thinner overcoats may reduce the durability. NSIC is working on improved overcoats and lubricants.

Head disk interface operation has shifted from constant-start-and-stop mode to a ramp-load-and-unload mode. The head is parked on the ramp outside the disk. For read and write operations, the head flies in

and retrieves/writes data and then retreats to the ramp to park. This design minimizes head disk contacts. However, because of the reduced flight height, waviness of the disk, or rotational wobble, occasional contacts between the head and disk do occur and sometimes catastrophically. This kind of random contact takes place under high speed flying conditions and is difficult to measure.

A ridge is artificially created on a disk and a ruby ball is used to collide with the ridge under high speed conditions (see technical highlight). The impact force and the deformation are measured. Preliminary test results show the ranking of lubricants and overcoats agree with field experience. This quick test enables screening of different coating/lubricant combinations for their effectiveness in protecting the disk. A finite element model has also been successfully developed to predict the stress concentrations and deformation for a hard disk. The interaction of various mechanical properties of different layers can be simulated.

Another aspect of improved protection is the lubricant. The spacing allows only a monolayer of molecules to protect the surface. Hydrocarbon molecules hold promise to improve the bonding strength and self-repairing properties of the lubricant film. Current lubricant (perfluoropolyether) has limited solubility of functional molecules. We have demonstrated that a multi-component molecular assembly can be achieved by using hydrocarbon molecules. However the performance depends on film thickness. There is no known acceptable method to accurately measure the film thickness of a complex hydrocarbon film on an atomically rough surface at 1 nm scale. A master calibration sample was successfully developed using a circular barrier to contain a solution with a known amount of solute on an actual hard disk. The solution is frozen in liquid nitrogen and slowly evaporated under controlled conditions. Uniformity of the film is checked by FTIR. Samples of average film thickness were then measured by various methods and the correlation constants were obtained. This enables the use of hydrocarbon molecules for hard disk applications.

The bonding characteristics of lubricant molecules with overcoats are important in shear resistance. An electron spin resonance technique was developed to measure unpaired electrons of overcoats quantitatively. Working with MMC Corporation, a series of hard disk carbon overcoats on a glass substrate was measured. This technique is expected to provide a tool to control surface reactivity/energy.

Contributors and Collaborators

M. Bai; MMC Corp, UC Davis, NSIC (IBM, Seagate, Readrite, Maxtor), Pennzoil-Quaker State

Metrology for Nanoscale Properties: Brillouin Light Scattering

A Brillouin light scattering facility has been constructed for measuring phonon and magnon properties at gigahertz frequencies in micron-scale volumes of thin-film materials. The current focus of research using this system is on characterizing interactions between magnetic modes and thermal phonons which play a central role in determining the switching times of magnetic-storage devices, spin-valve sensors, and other thin-film magnetic devices.

Ward Johnson and Sudook Kim

Technical Description

Brillouin light scattering is the inelastic scattering of incident photons with elastic waves (phonons) or spin waves (magnons) in a material. This scattering can involve either the generation of waves (Stokes process) or annihilation of waves (anti-Stokes process) in the material. Fabry–Perot interferometric techniques for measuring the shifts in photon frequencies arising from Brillouin scattering have evolved rapidly over the past couple of decades, such that they now provide powerful and practical methods of characterizing the dynamic properties of bulk and thin-film materials. In our division, these techniques are being pursued because of their capability to characterize both elastic and spin waves at gigahertz frequencies in thin-film material with surface areas typically on the order of 50 μm in diameter.

The research is currently focused on the interactions of magnons and phonons in ferromagnetic thin films. This subject is of great importance with respect to maximizing the speed of magnetic-storage devices, spin-valve sensors, and other thin-film magnetic devices. The coupling of directly excited spin waves to other waves in the material determines the time to achieve equilibration of the magnetization during a switching event. Brillouin light scattering may provide a particularly powerful tool for probing these interactions because the detection generally can be switched between magnons and phonons simply by rotating a polarizing filter in the path of the scattered light. The plan of research includes measurements of changes in the populations of magnons and phonons induced by ferromagnetic resonant excitation of permalloy ($\text{Ni}_{81}\text{Fe}_{19}$) thin films having varying amounts of rare-earth doping, which affects the damping constants of magnetic switching. Also, measurements will seek to determine whether rare-earth doping affects the peak line widths, which are proportional to the damping constants of the individual acoustic and spin waves.

Accomplishments

Over the past year, we have assembled a Brillouin-scattering system and placed it in operation.

Initial measurements of thermal magnons and phonons in thin films of pure permalloy ($\text{Ni}_{81}\text{Fe}_{19}$) and Tb-doped permalloy have been performed. Figure 1 shows typical magnon and phonon spectra from $\text{Ni}_{81}\text{Fe}_{19}$ (1.2% Tb). The central peak that extends off scale in both plots arises from a direct reference beam. Apparent peaks at frequencies near -2.7 GHz and $+3.5$ GHz in Figure 1(b) are experimental artifacts arising from elastic scattering off the sample. Peaks to the left and right of the central peak arise, respectively, from Stokes and anti-Stokes interactions with magnons and phonons having various symmetries.

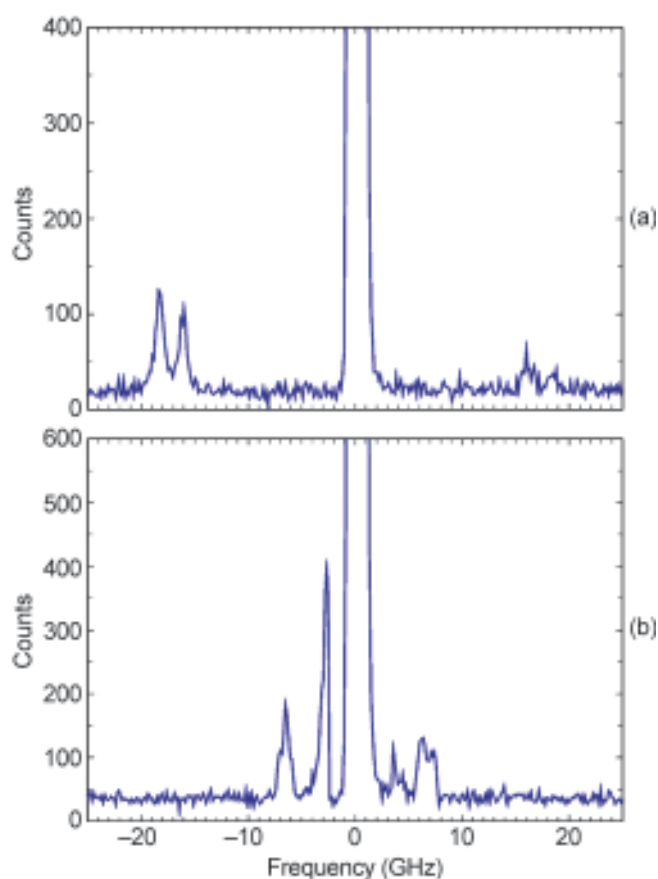


Figure 1: Brillouin spectra from a $\text{Ni}_{81}\text{Fe}_{19}$ thin film doped with 1.2% Tb. (a) Magnon spectrum. (b) Phonon spectrum.

Contributors and Collaborators

P. Kabos (NIST Radio-Frequency Technology Division); S. Russek (NIST Magnetic Technology Division); C. Patton (Colorado State University)

This project was partially funded by the National Nanotechnology Initiative.

Nanoscale Characterization: Electron Microscopy

Electron microscopy is used to characterize the structure and chemistry of materials at the nanometer scale to better understand and improve their properties. New measurement techniques in electron microscopy are being developed and applied to materials science research. The MSEL Electron Microscopy Facility primarily serves the Metallurgy, Ceramics, and Polymers Divisions as well as other NIST staff and outside collaborative research efforts.

John E. Bonevich

Atomic-scale structure and compositional characterization of materials can lend crucial insights to the control of their properties. For instance, direct observation of local structures by transmission electron microscopy (TEM) provides an important information feedback to the optimization of crystal growth and processing techniques. Various characteristics may be observed such as crystal structure and orientation, grain size and morphology, defects, stacking faults, twins and grain boundaries, second phase particles — their structure, composition and internal defect structure, compositional variations and the atomic structure of surfaces and interfaces.

The MSEL Electron Microscopy Facility consists of two transmission electron microscopes, three scanning electron microscopes, a specimen preparation laboratory, and an image analysis/computational laboratory. The JEOL3010 UHR-TEM has atomic scale resolution as well as detectors for analytical characterization of thin foil specimens. An X-ray detector (EDS) provides compositional analysis and an energy-selecting imaging filter (IF) allows compositional mapping at atomic resolution. The JSM6400 is equipped with electron backscattered diffraction/phase identification (EBSD) and EDS systems for characterization of texture and composition of materials.

FY2002 Highlights

- ATP intramural research collaboration with the Semiconductor Electronics and Electricity Divisions (EEEL) to characterize quantum effects in confined Si devices.
- ATP intramural research collaboration with the Optoelectronics Division (EEEL) to characterize quantum dot III-V materials.
- Measurement of size distributions in CeO₂ nanoparticles for use as an x-ray particle size standard reference material.
- Characterization of superconformal deposition of silver in sub-100 nm features for on-chip interconnections.

The shape of self-assembled quantum dots (QDs) play a major role in their electronic properties. In conjunction with RHEED and AFM, TEM studies of QD shape and faceting have revealed novel structures in In_{0.44}Ga_{0.56}As (see Figure 1). Typical models for QD shape include hexagonal dots as well as diamond shaped pyramids. However, TEM results show unusual facets. Instead of appearing with trapezoidal or triangular cross-sections, the QDs have multiple facets at their peaks and bases. The varied shapes have implications for the control and reproducibility of the MBE growth process of QDs.

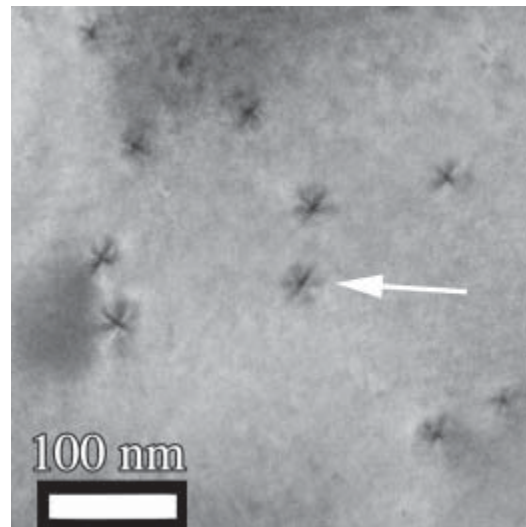


Figure 1: Plan-view TEM of InGaAs QDs reveals “X” features indicating the shape due to surface facets. Some QDs have additional facets (arrowed).

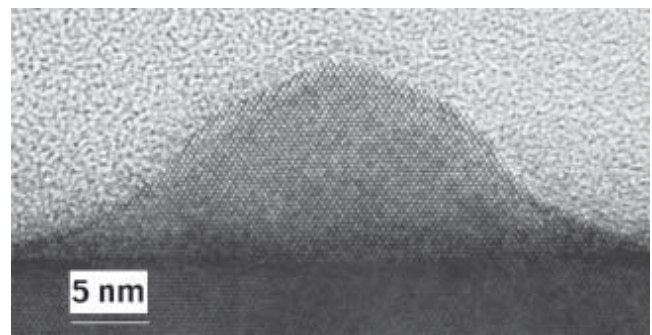


Figure 2: Cross-sectional HRTEM of InGaAs QDs indicating unusual faceting.

Contributors and Collaborators

R.D. McMichael, D. Josell, T.P. Moffat, J. Cline (MSEL); A. Roshko, S. Lehman (EEEL); E. Vogel, N. Zimmerman (EEEL); Prof. A. Stanishevsky (University of Maryland, Institute for Plasma Research)

Phase Diagrams in High Temperature Superconductors

Phase diagrams serve as “road maps” for processing high T_c superconductors. Of current interest are the $Ba_2RCu_3O_{6+x}$ ($R = Sm, Gd$ and Er) superconductors. The critical single-phase regions of $Ba_{2+x}(Nd_{1+x-y}R_y)Cu_3O_{6+z}$ for $R = Gd, Y$ and Yb were determined such that both flux-pinning and melting can be tailored and optimized. The construction of subsolidus phase diagrams of these systems, and the role of phase equilibria and kinetics in the formation of the $Ba_2YCu_3O_{6+x}$ phase, are deemed important for the rapid advancement of second generation coated conductor technology.

Winnie Wong-Ng and Lawrence Cook

NIIST phase equilibrium research has continued to provide critical information pertinent to the development of practical superconductors. DOE has supported high T_c research through a program of intensive R&D focused on wire and cable for high-impact commercial applications. This effort includes three principal groups of superconductors: (1) 1st generation Bi-Pb-Sr-Ca-Cu-O (BSCCO)-based wire/tape produced by the Ag-powder-in-tube (PIT) technique; (2) 2nd generation $Ba_2RCu_3O_7$ -type (Y-213 and R-213, $R =$ lanthanide) coated-conductors produced by rolling-assisted biaxially-textured substrate/ion beam assisted deposition (RABiTS/IBAD); (3) the recently discovered MgB_2 material.

By mixing the smaller lanthanides (Gd, Y, Yb) with the larger Nd in the $Ba_{2-x}(Nd_{1+x-y}R_y)Cu_3O_{6+z}$ (Nd-213) superconductor, both the flux-pinning and the melting properties can be tailored and optimized. A size trend in the single phase solid solution prepared in air was observed. Due to the closer match in size of Nd^{3+} with Gd^{3+} than Nd^{3+} with Y^{3+} , and Nd^{3+} with Yb^{3+} , the solid solution region is largest for the Gd-substituted system and smallest for the Yb-substituted system. We have successfully characterized selected solid solution members by x-ray, neutron, and electron diffraction, and by differential thermal analysis (DTA). There is considerable improvement of $J_c(H)$ for samples with partial Y-substitution at higher field at 77 K, compared with that of $Ba_2NdCu_3O_{6+z}$ and $Ba_2YCu_3O_{6+z}$. This improvement is likely due to the increased flux pinning as a result of doping of Nd^{3+} in the Ba^{2+} site.

The “ BaF_2 *ex situ*” process and the liquid-phase-epitaxy process are promising methods for producing long-length high quality Y-213 superconductor. Therefore investigation of the phase relationships in the system BaF_2 - BaO - Y_2O_3 - CuO_x - H_2O is another area of concentration. Using specially constructed controlled-atmosphere instrumentation and a strategic approach, we succeeded in determining the presence of low

temperature liquids in this air-sensitive multicomponent reciprocal Ba-Y-Cu//O,F system, which can be modeled in compositional space as a trigonal prism. This prism can be viewed as consisting of three tetrahedra (BaO - Y_2O_3 - CuO_x - BaF_2 , BaF_2 - YF_3 - CuF_2 - CuO_x , and BaF_2 - Y_2O_3 - CuO_x - YF_3). We have also initiated a more detailed study of melt equilibria in the BaF_2 - BaO - Y_2O_3 - CuO_x system. The role of $Ba(OH)_2$ in this system, as related to low-temperature melting, was identified as warranting further investigation. All this information is important for both the “ BaF_2 ” process and liquid phase epitaxy process.

To control film properties, it is important to understand the details of Y-213 phase evolution from amorphous “ BaF_2 ” films. To collect data at a faster rate over a broader range, we have used a position-sensitive detector on the high-temperature x-ray diffractometer. Three sets of films with different thickness (provided by R. Feenstra of the Oak Ridge National Laboratory) have been studied. We found that the growth of the Y-213 phase is controlled by the reaction at the interface of the Y-213/precursor, not by diffusion. Sufficient water vapor pressure is critical for Y-213 formation. The detailed phase evolution sequence, kinetics of phase formation, and the texture of these films as a function of processing parameters, will continue to be pursued.

A smaller effort was spent on the study of the melting equilibria of the Pb-doped and Pb-free Bi-2223 superconductors. In collaboration with FSU, the Pb-free 2223 phase was found to be in equilibrium with eight phases in the Bi-Sr-Ca-Cu-O system. Investigation continues to obtain a complete set of subsolidus 4-phase volumes, which is necessary for the determination of the primary phase field. We have measured the enthalpy of formation of MgB_2 , at 298 K by solution calorimetry. The vapor pressure of MgB_2 up to 1100°C was also successfully measured using a thermogravimetric effusion method.

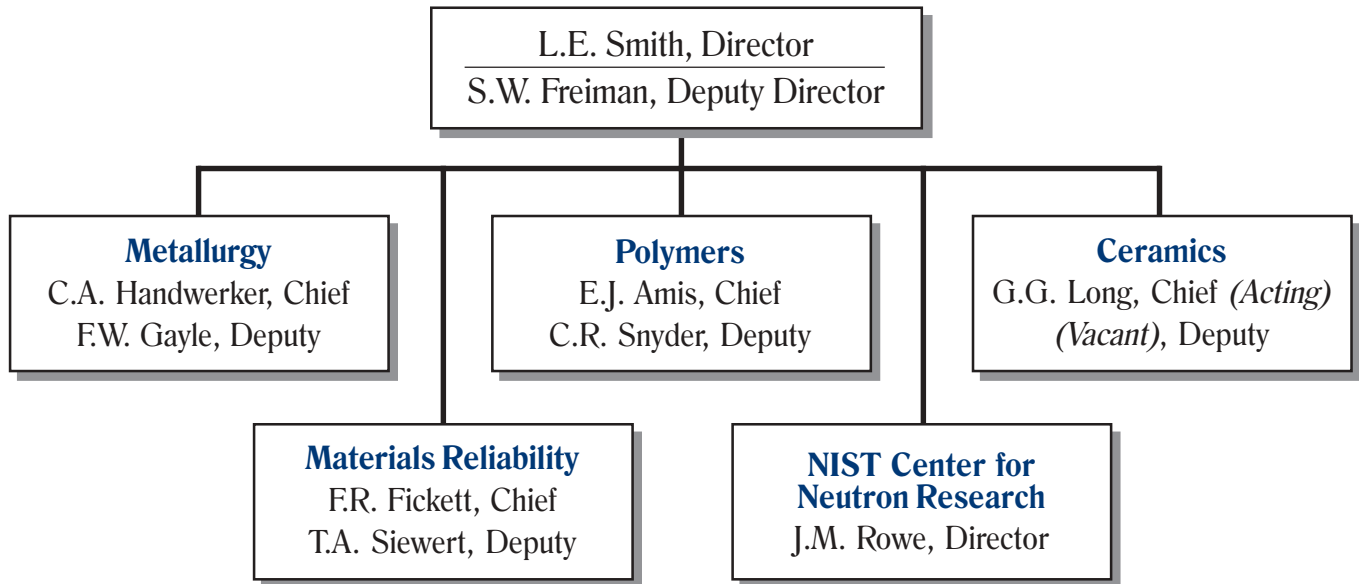
As data accumulate, we anticipate increased use of thermodynamic methods for data smoothing and extrapolation, with the ultimate goal of producing a comprehensive phase equilibria model for each of the three major high T_c systems. By providing the phase equilibria data as the basis for optimal processing, high T_c technology will be advanced through reductions in cost and improvements in performance.

Contributors and Collaborators

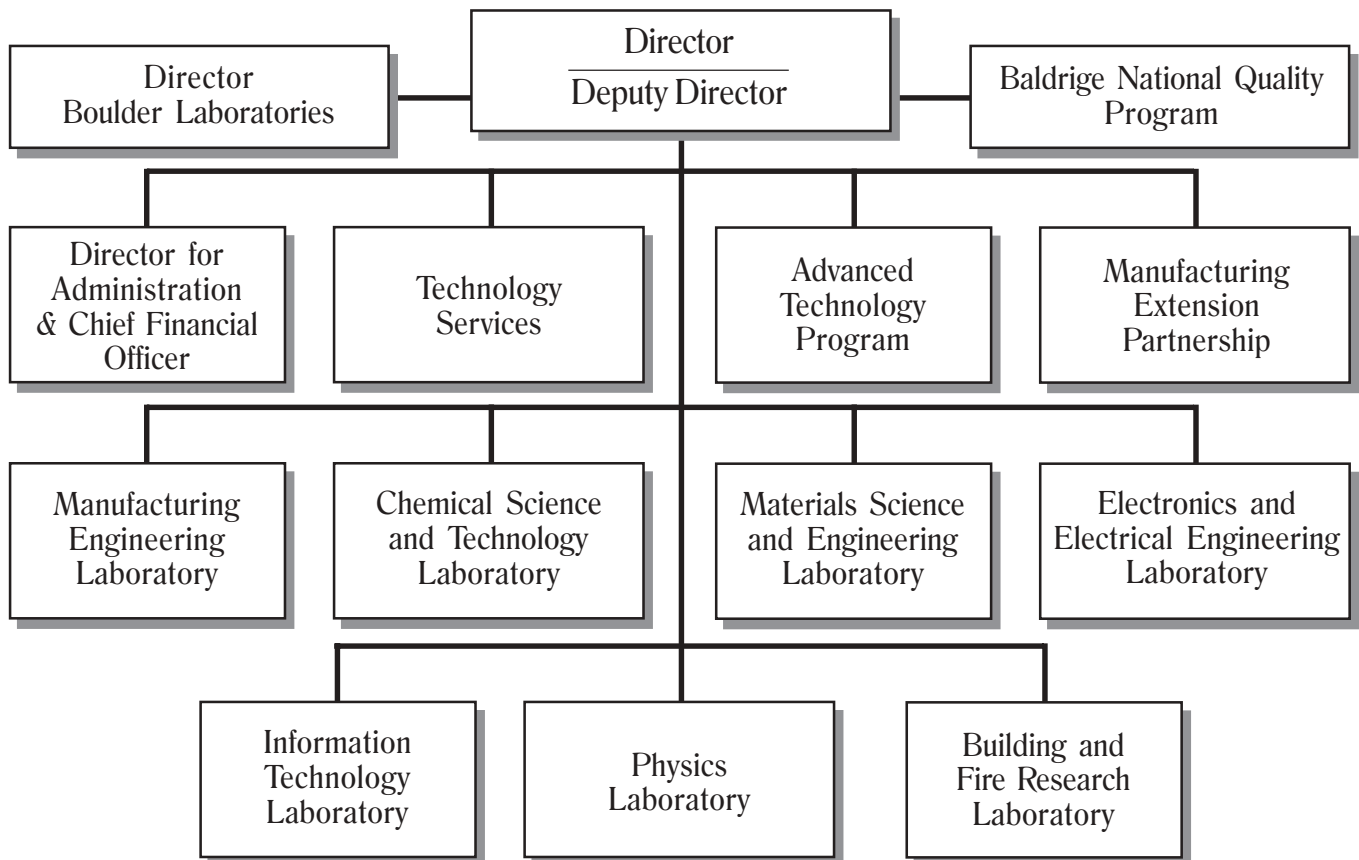
I. Levin, M. Vaudin, J.P. Cline (Ceramics); Q. Huang, B. Toby (Reactor); L. Swartzendruber (Metallurgy); A. Kearsley (Mathematical and Computational Sciences); R. Klein (Chemistry); T. Holesinger (LANL); R. Feenstra (ORNL); M. Rupich (AMSC); J. Storer (3M); J. Kaduk (BP-Amoco); R. Meng (University Houston); M. Suenaga (BNL); and PVPSS Sastry (FSU).

Organizational Charts

Materials Science and Engineering Laboratory



National Institute of Standards and Technology



MSEL

